UNIVERSITY OF OKLAHOMA

GRADUATE COLLEGE

PHOSPHATIDYLSERINE TARGETED BIOTECHNOLOGY AGENTS FOR CANCER

A DISSERTATION

SUBMITTED TO THE GRADUATE FACULTY

in partial fulfillment of the requirements for the

Degree of

DOCTOR OF PHILOSOPHY

By

NEEDA ALNOOR VIRANI
Norman, Oklahoma
2017

PHOSPHATIDYLSERINE TARGETED BIOTECHNOLOGY AGENTS FOR CANCER

A DISSERTATION APPROVED FOR THE
STEPHENSON SCHOOL OF BIOMEDICAL ENGINEERING

BY

_____
Dr. Roger G. Harrison, Chair

_____
Dr. Robert E. Hurst

_____
Dr. Vassilios I. Sikavitsas

_____
Dr. Edgar A. O'Rear III

_____
Dr. Barbara Safiejko-Mroczka

This thesis is dedicated to
my parents, Laila and Alnoor Virani,
and my brother, Zoheb Virani.

Mom, I completed your dream.

I would not be where I am today without your continuous work, untiring efforts, belief in me, and most importantly love.

Thank you.

Bismillah.

Acknowledgements

I would like to thank my committee, Dr. Edgar O'Rear, Dr. Vassilios Sikavitsas, Dr. Robert Hurst, Dr. Barbara Safiejko-Mroczka, and Dr. Roger Harrison, for their support and guidance throughout my course work and these projects. I would like to especially thank my amazing advisor, Dr. Harrison for his insightful guidance and support throughout my four years. Working with you has given me an enormous amount of knowledge and skills that will help propel me throughout my career. I would also like to thank all my collaborators: Dr. Doris Benbrook, Dr. Vibhudutta Awasthi, Dr. Joel Slaton, Dr. Elangovan Thavathiru, Andria Hendrics, and Carole Davis.

I would like to thank all of my funding sources: University of Oklahoma Institute for Biomedical Engineering, Science, and Technology; Peggy and Charles Stephenson Cancer Center; and Gynecological Cancer Program at the University of Oklahoma Health Sciences Center. I would like to thank the following for their contributions: Cancer Tissue Pathology Core at the Stephenson Cancer Center at the University of Oklahoma for performing tissue processing and immunohistochemistry services, specifically Dr. Kar-Ming Fung, Sheeja Aravindan, Dr. Muralidharan Jayaraman, and Louisa Williams; Dr. Ricardo Silvy for the carbon nanotubes; Molecular Imaging Core at the Stephenson Cancer Center for their animal imaging equipment; Dr. Rajagopal Ramesh's laboratory for transfecting cells; Dr. Michael Ihnat's laboratory his fluorescent dissection microscope; and Noble Microscopy Facility at the University of Oklahoma for use of their compound and transmission electron microscope.

I am very grateful to my colleagues in the Harrison laboratory, specifically Patrick McKernan and Dr. John Krais, who have provided significant assistance throughout my four years at the University of Oklahoma. I would also like to thank all the staff and graduate students who have been part of the Biomedical Engineering and the Chemical, Biological, and Materials Engineering departments over the past four years. I would specifically like to thank Terri Coliiver, Pamela Meek, Julien Arrizabalaga, Zachary Musset, Zachary Yokell, Emi Kiyotake, Aaron Simmons, Jin Liu, Cortes Williams, James Buerck, and Christopher Lewis.

I would like to thank my friends in Oklahoma, Serena and Nabeel Jamal, Rameez Dewany, Sheeba Aga, and Saliha Panjwani (my little sister), who have now become like family, for supporting me throughout my PhD with encouraging words and board game nights. I would also like to thank my friends who have moved all across the country but have still been there from the beginning: Anum Ali Mohammed, Shabeen Khetani, and Sanaa Charania. I would like to thank Chase Brown for being there unconditionally for the last two years of my PhD, always supporting me academically as well as emotionally. These last two years would have been significantly more difficult and mundane without you. Lastly, I would like to thank my family: my parents, Laila and Alnoor Virani, my brother and his fiancée, Zoheb Virani and Azmeena Charania, my cousins, Rozina and Sadiq Merchant, and all my aunts and uncles in the U.S. and India for always being supportive, encouraging, and loving no matter the odds. I would not be getting a PhD without the love and support of every single person mentioned here. Thank you.

Table of Contents

Acknowledgements iv

List of Tables xiii

List of Figures xiv

Abstract xvi

Chapter I: Introduction 1

Cancer. 1

Bladder Cancer 2

Ovarian Cancer 3

Breast Cancer 4

Biotechnology Agents for Therapy 5

Single-walled Carbon Nanotubes 5

Enzyme prodrug System 5

Biotechnology Agents for Imaging 7

Gold Nanoparticles 7

Passive versus Active Targeting 8

Enhanced Permeation and Retention Effect 8

Active Targeting Molecular Site: Phosphatidylserine 9

Active Targeting Molecular Agent: Annexin V 12

Scope of Thesis 13

Chapter II: Phosphatidylserine Targeted Single-walled Carbon Nanotubes for Photothermal Ablation of Bladder Cancer 15

Abstract 15

Introduction 16
Materials and Methods 19
Materials 19
Cell lines and culture conditions 20
ANXA5 and SWCNT-ANXA5 production 20
Binding strength 20
Fluorescent microscopy of SWCNT-ANXA5 in vitro 21
In vitro cytotoxicity studies 21
Animal handling procedures 21
In vivo laser tolerance 22
In vivo tumor model 22
In vivo SWCNT-ANXA5 specific tumor cell binding 23
Biodistribution 23
In vivo therapy efficacy 23
Statistics 24
Results. 25
In vitro binding and tolerance 25
In vivo laser tolerance 27
In vivo SWCNT-ANXA5 specific tumor cell binding 27
Biodistribution 28
In vivo tumor ablation 29
Discussion 32
Conclusions 35

Chapter III: Targeted Single-Walled Carbon Nanotubes Thermal Ablation of Cancer via a Radiofrequency Field 36
Abstract 36
Introduction 37
Materials and Methods 41
Materials 41
ANXA5 and SWCNT-ANXA5 production 41
Resonant Frequency Determination 41
Results. 43
Discussion 44
Conclusions 46
Chapter IV: Enzyme Prodrug System in Combination with Immunostimulation for Treatment of Metastatic Ovarian Cancer 47
Abstract 47
Introduction 49
Materials and Methods 55
Materials 55
Cell lines and culture conditions 55
mCTH-ANXA5 production 56
Binding strength 56
Fluorescent microscopy of SWCNT-ANXA5in vitro 56
In vitro cytotoxicity studies 57
Mouse tumor models and treatments 57

In vivo mCTH-ANXA5 toxicity 58
Flow Cytomerty Analysis 58
Antibody Titers 60
Statistics 61
Results. 62
In vitro binding and cytotoxicity 62
In vivo fusion protein dosage study 63
In vivo immunostimulant combination study 64
Long-term survival study 65
Discussion 73
Conclusions 78
Chapter V: Mutation of Cystathionine gamma-lyase for Improved Activity and Therapeutic Efficacy 79
Abstract 79
Introduction 80
Materials and Methods 81
Materials 81
Fusion protein construction, expression, and purification 81
Fusion protein specificity constant assay 83
Cell line and culture conditions 83
Binding strength 83
In vitro cytotoxicity studies 83
Statistical Analysis 83

Results. 84
Mutant fusion protein characterization 84
In vitro cytotoxicity 84
Discussion 86
Conclusions 87
Chapter VI: Enhanced MicroCT Imaging via Phosphatidylserine Targeted Gold Nanoparticles 88
Abstract 88
Introduction 89
Materials and Methods 92
Materials 92
ANXA5 production 92
AuNP-ANXA5 Synthesis 93
Dynamic light scattering and zeta potential 95
Agarose gel 95
Transmission electron microscopy 95
Cell lines and culture conditions 96
In vitro binding strength 96
In vitro fluorescence visualization 96
In vitro microCT contrast enhancement 96
Animal handling procedures 97
In vivo tumor model 97
In vivo blood clearance 97

In vivo targeted binding affinity 98
Statistics 98
Results. 99
Characterization of AuNP-ANXA5s 99
In vitro confirmation 101
In vivo confirmation 103
Discussion 108
Conclusions 110
Chapter VII: Conclusions and Future Directions 111
Single-walled carbon nanotubes 112
Enzyme prodrug system 114
Gold nanoparticles 117
Phosphatidylserine targeting biotechnology agents 119
References 120
Appendix A: Supplemental Data 138
Appendix B: mCGL-ANXA5 Gene Construction 144
mCGL-ANXA5 Complete Sequence 145
Gibson Assembly Fragments 147
Appendix C: Laboratory Protocols 149
FIJI macro for bladder tumor quantification 149
Flow Cytometry Staining 152
Antibody Titers 155
mCGL-ANXA5 Transformation 157

Synthesis of AuNP-ANXA5 161

AuNP-ANXA5 Blood Pharmacokinetics 164

List of Tables

Table 1. Antibodies for flow cytometry analysis. 60

Table 2. Median survival statistics. 67

Table 3. DLS and zeta potential of AuNP-ANXA5. 101

List of Figures

Figure 1. SWCNT-ANXA5 and NIR light combination therapy mechanism..... 18

Figure 2. Ultrasound images of fiber positioning in bladder..... 22

Figure 3. In vitro binding specificity and SWCNT-ANXA5 and NIR tolerance..... 27

Figure 4. In vivo NIR tolerance and tumor specific SWCNT-ANXA5 binding..... 28

Figure 5. In vivo therapeutic efficacy study..... 31

Figure 6. Schematic of electromagnetic waves inducing carbon nanotube heating..... 38

Figure 7. Schematic of tumor vasculature targeted ablative therapy. 40

Figure 8. Resonance frequency analysis. 43

Figure 9. Schematic of the proposed therapy. 53

Figure 10. Study progression timeline..... 58

Figure 11. In vitro binding specificity and cytotoxicity of the enzyme prodrug system.63

Figure 12. Enzyme prodrug system dosage and immunostimulant study. 65

Figure 13. Survival and toxicity of enzyme prodrug synergistic therapy. 66

Figure 14. Cell- and antibody-mediated immune response generated due to the addition of immunostimulants..... 72

Figure 15. DNA gel electrophoresis of mCGL-ANXA5 E. coli colonies..... 82

Figure 16. In vitro cytotoxicity of the new enzyme prodrug system..... 85

Figure 17. Schematic depicting synthesis of tumor targeted gold nanoparticles (AuNP-ANXA5). 95

Figure 18. Characterization of AuNP-ANXA5. 101

Figure 19. *In vitro* binding specificity of AuNP-ANXA5..... 102

Figure 20. Blood clearance..... 103

Figure 21. Representative CT images (xz cross section) of Balb/c mice with 4T1 breast cancer tumors. 105

Figure 22. Binding specificity of targeted versus untargeted AuNPs *in vivo*. 107

Figure 23. Binding strength data of ANXA5 for bladder cancer cells. 138

Figure 24. In vitro cytotoxicity of SWCNT-ANXA5s with NIR. 139

Figure 25. Standard curve for SWCNT-ANXA5 versus NIR fluorescence. 139

Figure 26. Schematic of RF system and matching network. 140

Figure 27. Binding strength data of mCTH-ANXA5 for ovarian cancer cells. 140

Figure 28. Michaelis-Menten kinetics. 141

Figure 29. Binding strength data of mCGL-ANXA5 for breast cancer cells. 142

Figure 30. Standard curve for AuNP concentration. 142

Figure 31. Standard curve for AuNP-ANXA5 concentration compared to CT intensity. 143

Figure 32. Binding strength data of AuNP-ANXA5 for breast cancer cells. 143

Abstract

Cancer is a highly mutating disease that quickly develops resistance to chemotherapies and has a high rate of relapse. If detected early, the survival rate is greater than 90% for most cancers; however if diagnosed during late, metastatic stages survival rate falls sharply to only 10%. Most cancer therapy is delivered systemically with no targeting specificity, which leads to high accumulation in healthy tissue and eventual toxicity. The high toxicity caused by current chemotherapeutics is a key limiting factor in complete eradication of tumors. Another key limiting factor is the development of resistive tumors. A large number of patients undergo multiple rounds of chemotherapy and surgery with the eventual progression into terminal stage cancer due to the development of resistive tumors.

Phosphatidylserine (PS) composes 8 -15% of the total phospholipids that make up the plasma membrane of a mammalian cells. In normal, healthy cells, PS is asymmetrical and only expressed on the inner leaflet of the membrane. In apoptotic cells, PS is exposed on the extracellular surface of the membrane as an “eat me” signal for immune cells such as macrophages to initiate immune suppressive clearance. Viable cancer cells use PS in a similar manner by expressing it on the external leaflet of the plasma membrane along with other “don’t eat me” signals to promote an immunosuppressive environment without clearance. Due to this externalization, PS can be used as a specific target for biotechnology agents. Annexin V (ANXA5), a mammalian protein, specifically binds to PS *in vitro* as well as *in vivo*. ANXA5 can be use to target biotechnology agents, such as nanoparticles and molecular drugs,

specifically to the tumor. This thesis focuses on the use of the strong interaction between PS and ANXA5 in biotechnology agents for cancer.

Chapter I: Introduction

Cancer

Cancer is one of the most elusive and varied diseases; however within all cancers, there are six key hallmarks that assist in its survival and proliferation: 1) sustaining proliferative signaling, 2) evading growth suppressors, 3) activating invasion and metastasis, 4) enabling replicative immortality, 5) inducing angiogenesis, and 6) resisting cell death [1].

Cancer cells can sustain proliferation by either producing their own growth factors or stimulating the surrounding normal cells to produce tumor proliferative growth factors. In order to sustain their proliferative growth, cancer cells also have to hinder tumor suppressor signals such as retinoblastoma-associated (RB) and TP53 proteins. The RB protein serves as a key gatekeeper by integrating extracellular signals with intracellular cell-cycle progression or inhibition. Many tumors have defects in their RB protein, thus losing the ability to check their growth feedback. Similar to the RB protein, TP53 also acts as a checkpoint gatekeeper; however most of its signals originate intracellularly. TP53 either activates or suppresses tumor growth based on the oxidative stress within the tumor and the degree of DNA mutations. TP53 is a common mutation among multiple tumors and in some cases is completely null, leading to uncontrollable growth [1-3].

The key to tumor progression is metastasis. Metastases can occur due to multiple cues including chemical, mechanical, and environmental. Initiation of metastasis is believed to occur via the epithelial to mesenchymal transition (EMT) in order to overcome anoikis, cell death as a result of detachment from the ECM.

Attachment to the ECM provides cells with pro-survival signals; however detachment for metastasis renders them venerable. Cancer cells down-regulate E-cadherin and up-regulate N-cadherin surface receptors that allow for extravasation [1, 4, 5]. Along with EMT, cancer cells continue to proliferate further into an immortalized cycle due to significantly increased amounts of functional telomerase, which adds telomere to the ends of DNA strands to counteract the loss with time [1, 6].

Angiogenesis, sprouting of new vasculature, is also a key component to sustain tumor growth. In normal tissue, angiogenesis occurs primarily during development, wound healing, and the female reproductive cycle, which then gets switched off. However sprouting of neovessicles in tumors is continuously turned on, leading to the development of immature, leaky vasculature [1, 7].

Bladder Cancer

Bladder cancer has one of the highest costs-to-patient ratios due to constant need for treatment of recurrent tumors. The current standard of care is a transurethral resection (TUR) followed by immunotherapy and Bacillus Calmette-Guerin (BCG) treatment intravesically. TUR surgery involves a cystoscope through the urethra to cut the bladder tumor, followed by cauterization. About 60-70% of bladder cancer patients have non-muscle-invasive bladder cancer (NMIBC). For those treated with TUR followed with secondary intravesical treatment, 75% develop recurrence within 5 years [8]. Aside from surgery, two drugs have been FDA approved as an alternative, thiotepa and valrubicin; both are generally used against BCG resistive tumors. In conjunction with chemotherapy, electromotive administration (EMDA), which allows for deeper

penetration of drugs into the bladder urothelium, is used. A clinical study comparing the use of EMDA versus only chemotherapy provided promising results with an increase in 5-year survival [9]. A hyperthermic heat-based approach using chemohyperthermia (CHT) has also been evaluated using epirubicin or mitomycin-c (MMC) in conjunction with microwaves (915 MHz) to increase bladder wall temperatures to greater than 41°C. Within two years, approximately half (56%) of the patients still had recurrence [8, 10].

Ovarian Cancer

Most women are diagnosed with ovarian cancer during late, metastatic stages. About 5 - 15% of women get ovarian cancer due to inherited factors with about 65% having BRAC1 and 35% having BRAC2 mutations [11]. If detected during early stages, the 5-year survival rate is 90%; however this rate significantly falls to 19% if detected after metastasis. About 80% of patients with ovarian cancer will relapse after the first round of chemotherapy, with about 15 - 20% already developing platinum-resistive tumors. From these, about 10% of patients survive only a few months with eventual terminal cases [11].

Due to a lack of an effective chemotherapy, clinical trials are underway using an anti-angiogenesis antibody, bevacizumab, with an overall 1 year survival rate of 58.6% [11, 12]. Another angiogenesis blockading therapy currently in clinical trials, pazopanib, had no survival increase but had increased risks of hypertension, neutropenia, liver-related toxicity, diarrhea, and fatigue [11, 13].

Breast Cancer

Although improvement in treatment and diagnosis of breast cancer has caused a decrease in mortality rates, patients are still misdiagnosed or overdiagnosed in 10 - 65% of cases. If detected early on, patients have a 94% 5-year survival rate, which drops to only 10% once metastasis has occurred [14]. Breast cancer is one of the few cancers with mass diagnosis capabilities. Current diagnosis includes a yearly mammogram for women 40 – 54 years, followed by a biopsy and follow-up imaging if abnormalities are identified. One of the biggest problems with current diagnostic tools such as mammograms is their high false positive rates that result in patients often being overdiagnosed and overtreated, some leading to mortality due to radiation-induced tumors. A key reason for this misdiagnosis is the inability of a mammogram to distinguish a dense breast from a tumor.

Biotechnology Agents for Therapy

Single-walled Carbon Nanotubes

Carbon nanotubes are a promising tool for tumor therapy due to their high mechanical strength, strength-to-weight ratio, and high thermal conductivity [15]. It has been shown that about 84% of the heat generated within a nanotube is transmitted to its surrounding substrate [16, 17]. This property of thermal dispersion can be utilized for cancer ablative therapies to cause temperature-based homeostatic disruption. Once the temperature of a cell rises above 47°C, irreversible cell death by ablation occurs which is characterized by cell necrosis and tissue coagulation [18].

Nanotubes can be single-walled (SWCNTs) or multi-walled (MWCNTs) [19]. For a tumor ablative therapy, SWCNTs are preferred over MWCNTs due to the screening effect seen by the inner shells of MWCNTs. This electrostatic screening diminishes the incident field within the structure [20]. Studies have shown that the dominant power dissipation from MWCNTs is due to the outermost shell, which results in significantly decreased absorption compared to SWCNTs [20, 21].

Enzyme prodrug System

An enzyme prodrug system is a multi-step process involving an enzyme delivered directly to the tumor followed by administration of a nontoxic prodrug, which is converted into a drug at the tumor [22, 23]. There are three main types of enzyme prodrug systems, gene-directed enzyme prodrug therapy (GDEPT), virus-directed enzyme prodrug therapy (VDEPT), and antibody-directed enzyme prodrug therapy (ADEPT) [22-24], each with advantages and disadvantages. One key advantage is the

ability to generate a toxic drug locally rather than systemic delivery of high doses of a cytotoxic drug, such as chemotherapy, that causes nonspecific tissue damage. Another key advantage is the bystander effect, which allows for small molecules to diffuse through the tissue to treat cancer cells with the enzyme bound as well as the surrounding cancer cells that do not have enzyme bound [22-24].

GDEPT and VDEPT rely on the enzyme being produced by the cancer cells by delivering the gene directly, while ADEPT relies on a targeted enzyme delivered to the cancer. All are followed with systemic delivery of a prodrug substrate [22-24]. GDEPT has an increased risk for nontumor cell transfections and mutagenesis, while VDEPT has the risk of a virus reverting back to wild-type and undergoing uncontrollable replication [22-24]. VDEPT also usually targets only replicating cells within the tumor, which in turn leaves 80-94% of cells untargeted and untreated [22, 23]. ADEPT has the disadvantage of eliciting an immune response due to the use of a nonhuman enzyme as well as an uneven tumor distribution [22, 23, 25, 26].

Biotechnology Agents for Imaging

Gold Nanoparticles

Gold nanoparticles have a significantly higher density compared to soft tissue, allowing them to generate greater contrast at the site of accumulation. Gold in conjunction with X-ray imaging can be used as a targeting agent to detect small lesions compared to a mammogram which has a detection limit of 10 – 20 mm [27]. Detection of small lesions and low grade tumors increases the survival rate of patients significantly and makes them more responsive to chemotherapy. Another advantage is the increased sensitivity and specificity of detection. One of the biggest problems with current diagnostic tools such as mammograms is their high false positive rates, which results in several patients being overdiagnosed and overtreated. A key reason for this misdiagnosis is the inability of a mammogram to distinguish a dense breast or microcalcification from a tumor. The use of a targeted contrast agent with computed tomography (CT) or an X-ray source eliminates this obstacle and should decrease rates of incorrect diagnosis [28]. CT is widely available in all clinics and hospitals, which is significantly cheaper than a biopsy or MRI, the second step in screening patients that test positive via a mammogram or the first form of screening for other suspected types of cancers. Another key feature using a targeted contrast agent such as gold nanoparticles is the broad applicability for detection of multiple cancers, such as bladder, ovarian, melanoma, and lung, which do not have effective diagnosis modalities that are sensitive as well as widely available [7]. Due to a lack of a cost-effective and globally available imaging modality, most patients are diagnosed during late stages of tumor development when chemotherapy is less effective.

Passive versus Active Targeting

Enhanced Permeation and Retention Effect

The phenomenon of nanoparticles preferentially accumulating at the tumor was identified more than 30 years ago in a poly(styrene-co-maleic acid)-neoCarzinoStatin (SMANCS) and albumin conjugate. The preferential accumulation is believed to be due to the immature blood vessels as well as an imperfect lymphatic drainage system. The combination of two immature systems is the enhanced permeation and retention (EPR) effect [29, 30].

When tumors reach a size greater than 2-3 mm^3 they need to produce new blood vessels in order to sustain themselves [31]; however this sprouting of new blood vessels is rapid and often irregular leading to a leaky vasculature. The irregularities cause gaps in the usually tight endothelial junctions that form the tubular structure of the vessel wall, which can range from 200 – 2000 nm. Normal vessels are impermeable to particles greater than 2- 4 nm, thus minimizing accumulation within normal, healthy tissue. Due to the gaps as well as the shift in pressure between the vessel and the remaining tumor, the "enhanced permeation" part of the EPR effect occurs, leading to increased, preferential accumulation of drugs and nanoparticles at the site of the tumor [29, 32]

The second part of EPR is due to the failure of an efficient lymphatic drainage system. In normal tissue, extracellular fluid is constantly drained into the surrounding lymph nodes at a mean flow velocity of 0.1 – 2 $\mu m\ sec^{-1}$. This drainage is significantly slowed down and impaired in the tumor microenvironment, leaving no place for

nanoparticles entering the tumor to exit. Particles smaller than 4 nm can be reabsorped into the bloodstream; however, most nanoparticles range from 10 – 300 nm [29, 32].

Active Targeting Molecular Site: Phosphatidylserine

A key feature of most tumor microenvironments is vascularization, which is necessary for overcoming the oxygen diffusion limitation and promoting growth [33]. Tumors recruit endothelial progenitor cells and co-opt existing vessels to generate a functional reactive stroma and promote angiogenesis [34]. The tumor vasculature is considered leaky and highly permeable due to the loss of tight junctions between endothelial cells [34]. A marker for the tumor vasculature is phosphatidylserine (PS), which is internalized in healthy blood vessels but externalized in tumor microenvironments [7, 35-37]. PS composes 8 – 15% of the phospholipd layer in mammalian cells [38, 39]. It exists to provide structural integrity to the plasma membrane, facilitates binding of endofacial surface protein binding, and Ca^{2+}-induced membrane fusion. Exposure of PS is considered a hallmark of apoptosis as an "eat me" signal for macrophages to be recruited for clearance [38, 40].

Marcophage clearance has three key signals: "find me," "eat me," and "engulf me" [41, 42]. The "find me" signal is usually a gradient of cytokines and chemokines released by apoptotic cells signaling the macrophages to recruit to the site of apoptosis. The gradient sets up a migration pattern which directs the phagocyte through the tissue and towards the dying cells. The second key signal is the "eat me" signal, which includes exposure of PS on the surface. It is estimated that on apoptotic cells, the concentration of the PS on the outer leaflet increases by 280-fold within a few hours

[41, 43]. Unlike apoptotic cells, which do get recognized, cancer cells also expose "don't eat me" receptors, which prevent recognition and eventual clearance. One of most well studied signals is CD47, or integrin-associated protein, which is expressed on healthy as well as tumor cells to deter interaction with phagocytes. Other surface ligands such as CD31, expressed on the surface of endothelial cells, and CD300a are also exposed as potential "don't eat me signals" [41, 44, 45]. Once recognition has occurred, the last signal is "engulf me". Apototic cells recruit macrophages in order to have clearance without the need to elicit an immune response as would be seen in necrosis [41].

The asymmetry of PS exposure is maintained by three key lipid transporters, flippase, floppase, and scramblase [38, 40, 46]. In a healthy cell, flippase transports aminophospholipids, PS and phosphatidylethanolamine (PE), from the outer leaflet to the inner leaflet of the plasma membrane and is inhibited by calcium [47, 48]. Floppase transports cholinephospholipids, phosphatidylcholine (PC) and sphingomyelin (Sph), as well as aminophospholipids from the inner leaflet to the outer. A major floppase is the ATP-binding cassette (ABC)-transporter ABCC1, which was previously known as the multi-drug resistant protein MRP1. ABCC1 acts in multi-drug resistance by increasing exocytosis of chemodrugs, thus decreasing the efficacy of the treatment and eventually causing resistance [38, 40, 49]. Another key floppase is ABCA1, which promotes surface exposure of PS and is present in most mammalian cells. Flippase and floppase usually require long periods before sufficient asymmetry of the plasma membrane is reached due to their ATP-dependent mechanisms. A third key transporter is scramblase, which is a bidirectional transporter that can rapidly flip any phospholipid in any

direction following influx of Ca^{2+} and can lead to membrane asymmetry within minutes [38, 40, 49].

Various physical changes to exposed PS effects its capability to act as an "eat me" signal. Studies have compared oxidized versus nonoxidized externalized PS with oxidized PS having a higher affinity for macrophage recruitment. Oxidized PS has a higher affinity to promote efferocytosis, which is considered a noninflammatory and nonimmunogenic process by which clearance occurs [40, 44, 50]. Cells undergoing programmed cell death or efferocytosis expose PS as a means to initiate clearance in an immunosuppressive manner, or silent clearance [40, 45]. Another key feature is the chirality of the PS exposed. A study compared PS in the L and D conformation and showed that macrophages engulfed PS isomers in the L but not D confirmation, which may also be a difference between PS exposed on apoptotic versus cancer cells [42].

Cancer cells along with some viruses and bacteria hijack the PS exposure mechanism as a means to generate an immunosuppressive environment [7, 35, 37, 45, 51]. Viable tumor cells, immature tumor vasculature, and tumor exosomes all expose PS as a means to prevent an inflammatory response and heighten immunosuppression [45].

Studies have shown that different types of cancer cells expose various amounts of PS, which may be dependent on the activity of flippase [48]. Tumors with increased PS externalization had decreased activity of flippase, which decreases the rate of PS transition from the outer to the inner leaflet of the plasma membrane leading to the loss of asymmetry [48]. PS externalization is also modulated by the intracellular calcium present. Calcium inhibits flippase activity but increases scramblase activity. Tumor cells

with increased levels of calcium had more PS exposure, which may be due to the decrease in flippase activity but also the increase in scramblase transitioning PS at a faster rate towards the outer leaflet [38, 40, 48].

Active Targeting Molecular Agent: Annexin V

Active targeting is the use of tumor specific ligands to increase recognition and uptake of molecules at the tumor region. Active targeting allows for faster and increased accumulation of the molecule at the tumor region. PS can be specifically targeted via annexin V (ANXA5) [37, 42].

ANXA5 is an anticoagulant protein that belongs to the annexin super-gene family. It is a nonglycosylated single chain protein with a C-terminal that contains four domains that come together to form the annexin-core. The core has a convex curvature that allows it to interact and bind to PS exposed on cancer cells and the tumor vasculature [52, 53]. ANXA5 has a Ca^{2+}-dependent binding interaction with PS. The Ca^{2+} binds to the ANXA5 core primarily composed of α-helices, at the C-terminal, specifically at the type II Ca^{2+} binding site [52, 53]. ANXA5 resides as a monomer in solution, but forms trimers when interacting with PS, which can lead to internalization [54]. A previous study reported a binding dissociation of ANXA5 and PS between 0.1 – 2 nM [52].

Scope of Thesis

Most current cancer therapies and imaging tools focus on delivering high doses of the drug or contrast agent and relying on the EPR effect for accumulation at the tumor site. The high dose is a key limiting factor leading to nonspecific toxicity of the agent. This study focuses on the use of the strong interaction between PS, which is exposed on tumor cells and vasculature, and ANXA5, a mammalian protein, to deliver targeted therapeutic and diagnostic agents to bladder, breast, and ovarian cancer, with the goal of eliminating or reducing toxic side effects to normal organs and tissue. This thesis is focused primarily on the development of the following for treating or detecting tumors:

1. Photothermal ablation of non-muscle invasive bladder cancer using PS-targeted single-walled carbon nanotubes and near-infrared light or radiofrequency.
    a. *In vitro* and *in vivo* studies determining the strong, specific binding between ANXA5 conjugated single-walled carbon nanotubes and cancer cells, as well as photothermal tumor cell death via a 980 nm near-infrared laser.
    b. Preliminary studies determining the resonance frequency of ANXA5 conjugated single-walled carbon nanotubes in a radiofrequency field for heat-based death of cancer cells.
2. Enzyme prodrug therapy for the treatment of metastatic ovarian cancer using a PS-targeted novel mutant enzyme prodrug (cystathionine gamma-lyase) with selenomethionine as the prodrug, in conjunction with immunostimulation.

a. *In vitro* and *in vivo* studies determining optimum dosage of the enzyme prodrug system in conjunction with immunostimulant pairs for a synergistic and immune stimulating therapy of metastatic ovarian cancer.
b. Development of a novel PS-targeting mutant of cystathionine gamma-lyase and determination of *in vitro* cytotoxicity compared to a previous mutant.

3. A novel PS-targeted gold nanoparticle for early detection of breast cancer using computed tomography (CT).

Chapter II in this dissertation has been submitted to *Nanotechnology* in July 2017. Chapters IV and VI have been written as publications for submission in 2017.

Chapter II: Phosphatidylserine Targeted Single-walled Carbon Nanotubes for Photothermal Ablation of Bladder Cancer

Abstract

Bladder cancer has a 60-70% recurrence rate most likely due to residual tumor left behind after a transurethral resection (TUR). Failure to completely resect the cancer can lead to recurrence and progression into higher grade tumors with metastatic potential. We present here a novel therapy to treat superficial tumors with the potential to decrease recurrence. The proposed therapy is a heat-based approach in which bladder tumor specific single-walled carbon nanotubes (SWCNTs) are delivered intravesically at a very low dose (0.1 mg SWCNT per kg body weight) followed by a short 30 sec treatment with a 360° near-infrared (NIR) light that heats only the bound nanotubes. Nanotubes are specifically targeted to the tumor via the interaction of annexin V (ANXA5) and phosphatidylserine (PS), which is normally internalized on healthy tissue but externalized on tumors and tumor vasculature. SWCNTs are conjugated to ANXA5, which binds specifically to bladder cancer cells as confirmed *in vitro* and *in vivo*. Due to this specific localization, NIR light can be used to heat the tumor while conserving the healthy bladder wall. In a short-term efficacy study in mice with orthotopic MB49 murine bladder tumors treated with the SWCNT-ANXA5 conjugate and NIR light, no tumors were visible on the bladder wall 24 h after NIR light treatment, and there was no damage to the bladder. In a separate survival study in mice with the same type of orthotopic tumors, there was a 50% cure rate at 116 days when the study was ended. At 116 days, no treatment toxicity was observed, and no nanotubes were detected in the clearance organs or bladder.

Introduction

Bladder cancer has high costs-per-patient ratios due to the elevated rate of recurrence [8, 55, 56]. Approximately 75-85% of patients have Ta/T1 stage non-muscle invasive bladder cancer (NMIBC) that can be treated using surgical transurethral resection (TUR). TUR is usually followed by intravesical chemotherapy and immunotherapy, which has proven to be effective in increasing remission periods; however 70% of patients still experience tumor relapse [8, 55-58]. Recurrence is believed to occur due to four main mechanisms: incomplete resection, re-implantation, disperse microscopic tumors, or new tumor development [8, 55, 57]. A previous study tested the frequency of each mechanism and determined incomplete resection and cell re-implantation after TUR to be the primary causes of most relapses [55]. Unfortunately, there has been limited improvement in therapeutic options for bladder cancer patients over the past 20 years [58]. Due to this void in research as well as the rapidly increasing costs associated with cycles of diagnostics and treatment, we have developed a novel approach to thermally ablate tumors using specifically targeted single-walled carbon nanotubes (SWCNTs) and near-infrared (NIR) laser light.

Photothermal ablation is the use of light to heat biologic tissue above 60°C over a short time period [59, 60]. Exposure to high temperatures leads to tissue death via necrosis and can be used as an alternative for chemoresistive as well as hyperthermic resistive tumors [59-61]. A previous study comparing the response of breast cancer to hyperthermia, a slow heating of tissue, versus ablation showed that ablation temperatures were able to eradicate hyperthermia resistive tumors [60].

A recent study of treating mice with bladder cancer used NIR light in combination with anti-epidermal growth factor receptor (anti-EGFR) coated gold nanoparticles obtained promising results using a procedure that required surgery to expose the bladder [62]. In the current study, we have focused on using targeted single-walled carbon nanotubes (SWCNTs) and have developed a clinically translatable procedure to irradiate the bladder without the need for surgery.

SWCNTs are gaining more attention as versatile nanoparticles in diagnostics and therapeutics for drug delivery, photodynamic therapy, and NIR contrast enhancement [63-66]. SWCNTs have an intrinsic excitation in the NIR range (700-1100 nm) that is released as vibrational energy. This energy is converted into heat that induces cell death via coagulative necrosis, rupturing of cell membranes, and denaturing of proteins [61, 67, 68]. Biological tissue has an "optimal window" within the NIR range making the tissue easily light penetrable up to a few millimeters [61, 64].

In order to enhance nanotube accumulation within the tumor as well as minimize nonspecific heat effects, SWCNTs are conjugated to annexin V (ANXA5), which strongly binds with phosphatidylserine (PS) [7, 37, 40, 69]. PS is primarily found in an asymmetric conformation on the inner leaflet of the plasma membrane of healthy cells; however in the tumor vasculature and cancer cells, it gets externalized, making it a specific and versatile targeting receptor for bladder cancer as well as other tumors [7, 36, 37, 40, 69]. The SWCNT-ANXA5 conjugate is delivered intravesically to the bladder for tumor specific accumulation. Intravesical delivery is commonly utilized over systemic since it provides a higher payload and the urothelium limits the absorption of particles into the bloodstream [56, 64, 68, 70].

Due to the strong association of ANXA5 to bladder tumors and the intrinsic property of nanotubes to absorb NIR light and dissipate energy as heat, this study hypothesizes that targeted SWCNT-ANXA5s in combination with a global radiating NIR fiber can be utilized as an alternative to treat NMIBC and reduce relapse rates without invasive surgery (figure 1). This study has proven that SWCNT-ANXA5s specifically target bladder cancer cells *in vitro* as well as *in vivo* with no detectable binding to normal urothelium; combining PS-targeted nanotubes with NIR light resulted in a 50% cure rate with no observable healthy tissue damage for orthotopic MB49 murine bladder tumors, thereby proving the effectiveness and clinical applicability of the proposed approach.

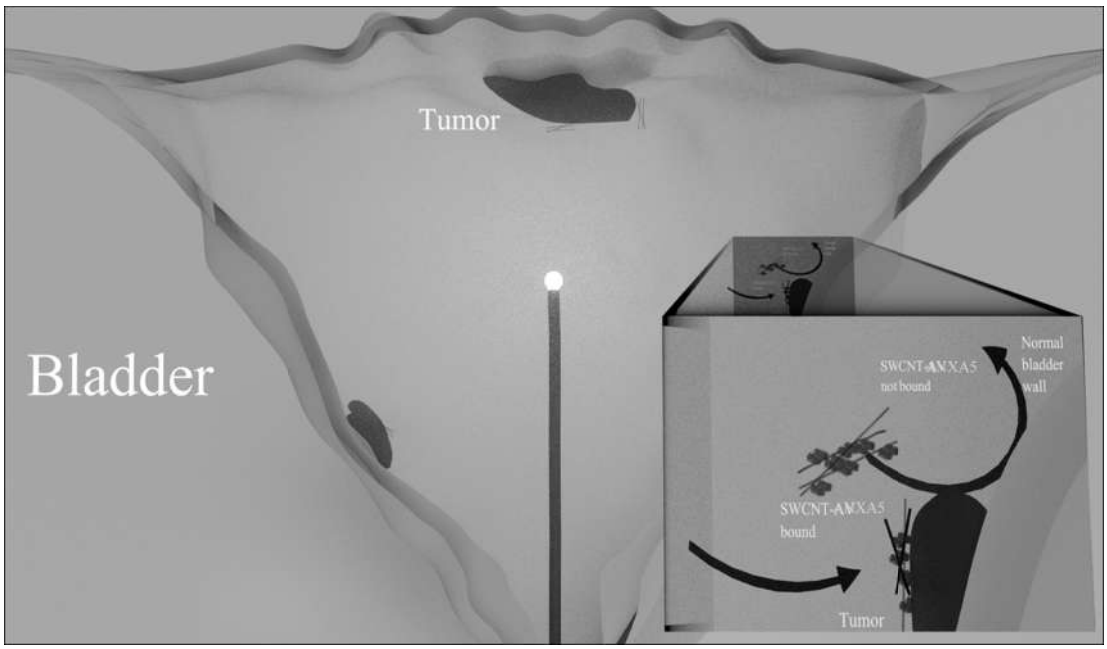

Figure 1. SWCNT-ANXA5 and NIR light combination therapy mechanism. Cancer targeted SWCNTs are instilled into the bladder via catherization. After a clearance period for unbound nanotubes, a globally diffusing fiber emitting a 980 nm light is threaded via a catheter into the center of the bladder. The tumor is irradiated to heat the bound nanotubes and cause cancer cell death.

Materials and Methods

Materials

The plasmid encoding ANXA5, pET-30 Ek/LIC/ANXA5, was previously constructed in this lab [64]. Bovine serum albumin (BSA), Alamar Blue reagent, Triton X-100, EDTA, and Tris-acetate-EDTA buffer were from Sigma-Aldrich (St Louis, MO). Sodium phosphate and sodium dodecyl sulfate (SDS) were from Mallinckrodt Chemicals (Phillipsburg, NJ). Paraformaldehyde was from Electron Microscopy Sciences (Hatfield, PA). Antifade reagent Fluoro-gel, borate buffer, fluorescein isothiocyanate (FITC), poly-L-lysine, and Slide-A-Lyzer dialysis cassettes (3.5 kDa) were from Thermo Fisher Scientific (Waltham, MA). The 2 and 100 kDa dialysis membranes were from Spectrum Laboratories (Rancho Dominguez, CA). Anti-ANXA5 (FL-319) was from Santa Cruz Biotechnology (Santa Cruz, CA). Murine bladder cancer cells (MB49) and human bladder cancer cells (J82) were from ATCC (Manassas, VA). RPMI-1640, Dulbecco's Modified Eagle, and keratinocyte-SFM cell medium were from ATCC (Manassas, VA). Fetal bovine serum (FBS) was from Atlanta Biologicals (Lawrenceville, GA). Antibiotics, penicillin and streptomycin, were from Invitrogen (Grand Island, NY). (6,5) CoMoCAT SWCNTs (average diameter 0.8 ± 0.1 nm, average length 1.5 ± .5 μm) were provided by Southwest Nanotechnologies, Inc. (Norman, OK). The 1,2-distearoyl-*sn*-glycero-3-phosphoethanolaminepolyethylene glycol-maleimide (DSPE-PEG-maleimide; PEG molecular weight of 3.4 kDa) linker was from Creative PEGWorks (Winston Salem, NC).

Cell lines and culture conditions

MB49 cells were transfected with tdTomato (Td) and luciferase (Luc) and J82 cells were transfected with Td. Normal bladder cells were HPV immortalized as described [71]. MB49-Td-Luc cells were grown in RPMI-1640 medium, and J82-Td cells were grown in Dulbecco's Modified Eagle's Medium with glucose. Both cell line media were enriched with 10% FBS and penicillin/streptomycin antibiotics (100 U ml^{-1} and 100 μg ml^{-1}, respectively). Normal immortalized bladder cells were grown in keratinocyte-SFM medium supplemented with 50 μg ml^{-1} bovine pituitary extract, 5 ng ml^{-1} epidermal growth factor, and penicillin/streptomycin antibiotics (50 U ml^{-1} and 50 μg ml^{-1}, respectively). All cells lines were grown at 37°C with 5% CO_2.

ANXA5 and SWCNT-ANXA5 production

Recombinant ANXA5 and the SWCNT-ANXA5 conjugate were produced as previously described [64]. The conjugation was performed using DSPE-PEG-maleimide linker. ANXA5 was characterized via SDS-PAGE, and SWCNT-ANXA5s were characterized by UV-Vis-NIR spectroscopy.

Binding strength

The dissociation constant for ANXA5 was determined as previously described [64] using biotin conjugated ANXA5 on 70% confluent MB49-Td-Luc and J82-Td cells. Specific binding was determined by subtracting total binding (medium supplemented with calcium) from nonspecific binding (medium supplemented with EDTA).

Fluorescent microscopy of SWCNT-ANXA5 in vitro

MB49-Td-Luc and J82-Td cells were grown to 70% confluence on cover slips. SWCNT-ANXA5s were tagged with FITC following a protocol by [64]. SWCNT-ANXA5-FITCs (20 mg l^{-1}) in 2 mM $CaCl_2$ were incubated with either MB49-Td-Luc or J82-Td cells for 2 h followed with PBS washing. The cells were fixed in 4% paraformaldehyde. Images were taken on a Nikon fluorescence microscope.

In vitro cytotoxicity studies

Alamar Blue pre- and post-cell viability assays were conducted to determine the cytotoxic effects of NIR and SWCNT-ANXA5s alone and in combination on both bladder cancer lines as well as normal bladder cells. Viability assays were conducted on cells at 70% confluence followed by either SWCNT-ANXA5 incubation at various concentrations for 2 h or NIR treatment for 30 sec at various energy levels. Cells were washed, and a second viability assay was conducted 18 h later.

Animal handling procedures

All procedures complied with a protocol approved by Institutional Animal Care and Use Committee (IACUC) of the University of Oklahoma Health Sciences Center. C57BL/6J female mice 10 weeks of age, weighing 20 – 22 g were used. Mice were on a standard chow diet. All studies on mice were conducted under anesthesia with 2% isoflurane and 98% oxygen using a nose cone.

In vivo laser tolerance

Fiber insertion and positioning was determined via ultrasound (VEVO 2100) as shown in figure 2. The fiber was threaded through a catheter attached to an adapter with a resealable end to push the fiber through and a second end with a syringe to fill the bladder with air. An *in vivo* NIR tolerance test at 50 and 100 J cm^{-2} for 30 sec with a globally radiating, 980 nm fiber was conducted. Mice were euthanized 24 h after treatment, and H&E staining on bladders was used to determine if damage was caused to the urothelium.

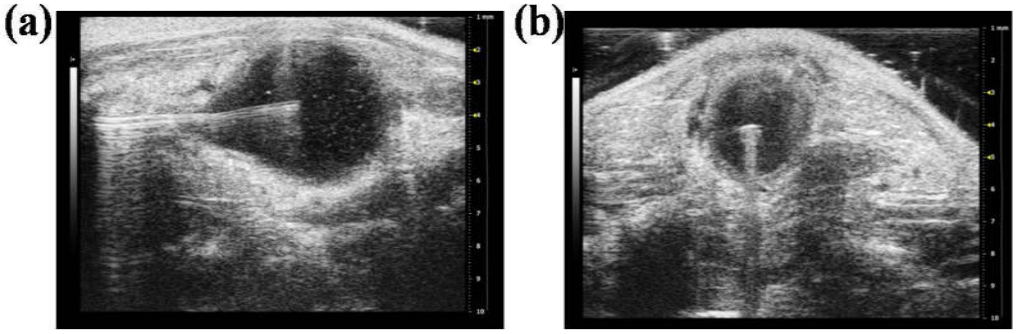

Figure 2. Ultrasound images of fiber positioning in bladder.
Ultrasound images of diffusing fiber centered in C57BL-6 mouse bladder in the x-z (a) and x-y (b) plane. A centered diffusing fiber ensures one session is required to treat the entire bladder and isolated residual tumor cells.

In vivo tumor model

Mice were anesthetized and catheterized with a 24 gauge catheter through the urethra. Urine was expelled and the bladder was washed with PBS. Mouse bladders were incubated with 100 µl poly-L-lysine for 20 min to disrupt the glycosaminoglycan (GAG) layer and allow for tumor implantation [72]. Bladders were inoculated with 100 µl of MB49-Td-Luc cells (5 x 10^5 cells ml^{-1}) for 1 h. All animal studies were conducted

once tumor presence was confirmed via bioluminescence on a Carestream X-treme Imager.

In vivo SWCNT-ANXA5 specific tumor cell binding

A mouse with an orthotopic bladder tumor was instilled with 100 µl of SWCNT-ANXA5s at a concentration of 20 mg l^{-1} (0.1 mg SWCNTs kg^{-1}) for 90 min. The mouse was euthanized 24 h later, and the bladder was collected for H&E and immunohistochemistry (IHC). IHC was conducted for SWCNT-ANXA5s using an anti-ANXA5 to stain the ANXA5 component of the nanotube conjugate. Images were taken on a Zeiss light microscope.

Biodistribution

NIR fluorescence spectroscopy (NS MiniTracer) analysis by Applied NanoFluorescence (Houston, TX) was conducted on the bladders of saline and SWCNT-ANXA5s treated mice 24 h after instillation. A second spectroscopy was conducted on mice that were tumor free 116 days after tumor instillation. Samples for NIR fluorescence spectroscopy were prepared as previously described [73].

In vivo therapy efficacy

A therapeutic efficacy study combining SWCNT-ANXA5s and NIR light was performed. Tumor presence was confirmed with bioluminescence imaging prior to study initiation. SWCNT-ANXA5s (100 µl of 0.1 mg kg^{-1}) were instilled for 90 min and followed with 30 sec of 50 J cm^{-2} NIR laser treatment 24 h later. The mice were

euthanized 24 h after NIR light treatment, and tdTomato fluorescence was measured with a Leica fluorescence dissecting microscope. Fluorescence was quantified via FIJI analysis (code for analysis can be found in Appendix C: Laboratory Protocols). A second set of mice was monitored every 3-4 days for survival post-treatment. H&E and Trichrome staining was conducted to evaluate toxicity of treatment and scar tissue formation.

Statistics

Statistical significance of *in vitro* studies was assessed using a one-way ANOVA and Tukey-Kramer multiple comparisons test with GraphPad Prism software. Statistical significance for tumor presence 24 h after treatment was assessed using Pearson's chi-square goodness of fit test.

Results

In vitro binding and tolerance

The dissociation constant of ANXA5 binding to MB49-Td-Luc and J82-Td cells was 4.14 ± 1.30 nM and 0.38 ± 0.20 nM, respectively, confirming a strong affinity of ANXA5 for bladder tumors (data can be found in Figure 23 of Appendix A: Supplemental Data). Once ANXA5 and PS interaction was confirmed, further evaluation of SWCNT-ANXA5s conjugate binding affinity was visualized via fluorescence microscopy. As seen in figure 3a, even after the conjugation of SWCNTs to ANXA5, ANXA5 still strongly associated with mouse as well as human bladder cancer cells.

Tolerance of bladder cancer as well as normal bladder urothelium cells for SWCNT-ANXA5s and NIR light was determined as seen in figure 3b and 3c. SWCNT-ANXA5 concentrations above 40 mg l^{-1} were detrimental to normal bladder cells and to a lesser extent for MB49 and J82 cells. In order to ensure no damage to healthy bladder urothelium occurred due to SWCNT-ANXA5 toxicity, a conservative 20 mg l^{-1} concentration of nanotubes was used for all following work. Normal bladder cells had a higher tolerance to NIR energies with minimum cytotoxicity seen up to 350 J cm^{-2}. Mouse (MB49) and human (J82) bladder cancer cell lines had noticeable decreases in viability at 150 J cm^{-2} and 100 J cm^{-2}, respectively. Combination therapy had a significant decrease in cell viability for both cancer cell lines as well (data can be found in Figure 24 of Appendix A: Supplemental Data).

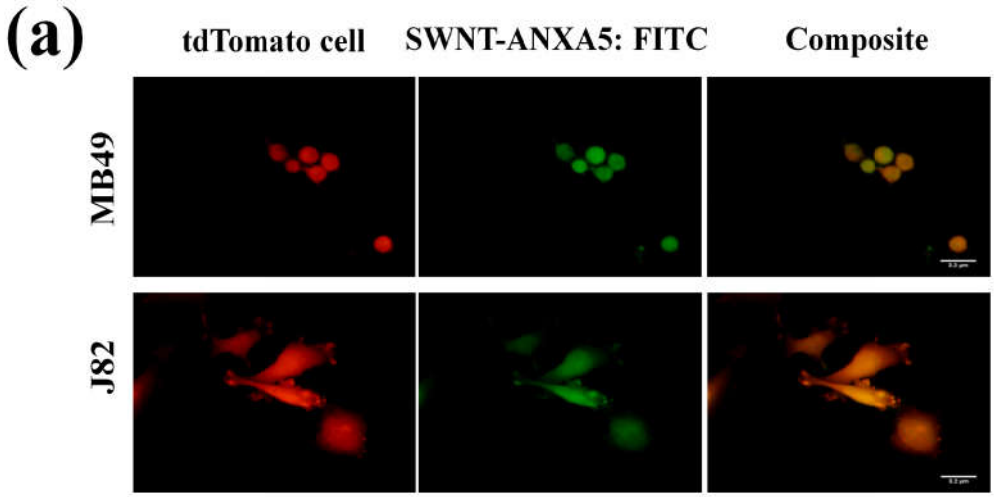
(a)
tdTomato cell
SWNT-ANXA5: FITC
Composite
MB49
J82

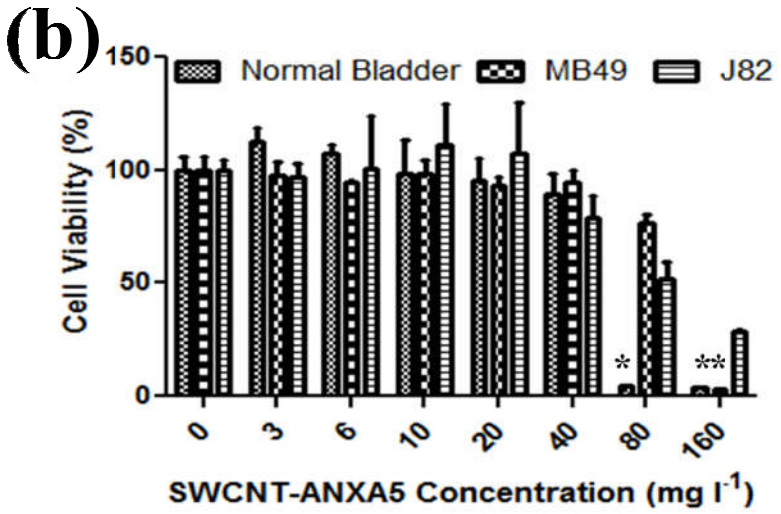
(b)
Normal Bladder
MB49
J82
Cell Viability (%)
150
100
50
0
*
**
0
3
6
10
20
40
80
160
SWCNT-ANXA5 Concentration (mg l-1)

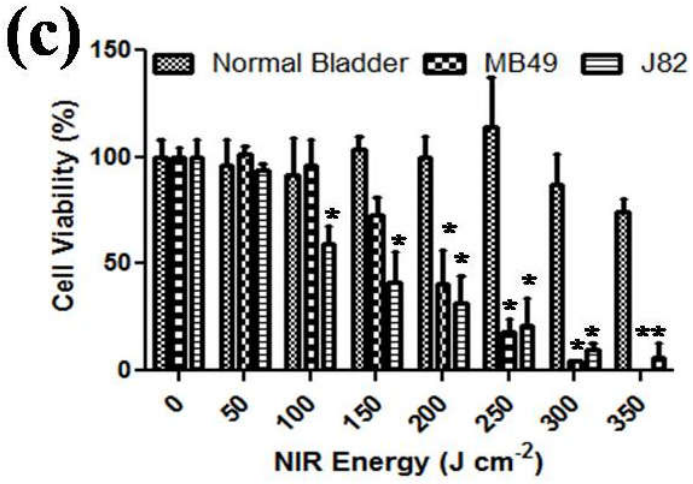
(c)
Normal Bladder
MB49
J82
Cell Viability (%)
150
100
50
0
0
50
100
150
200
250
300
350
NIR Energy (J cm-2)

Figure 3. In vitro binding specificity and SWCNT-ANXA5 and NIR tolerance. (a) Fluorescence imaging confirming SWCNT-ANXA5 binding to murine (MB49) and human (J82) bladder cancer cells. TdTomato transinfected MB49 and J82 cells (left), FITC labeled SWCNT-ANXA5s (middle), and composite (right). Scale = 3.2 μm. Murine and human bladder cancer lines as well as normal bladder cells were tested to determine tolerance to (b) SWCNT-ANXA5s and (c) NIR energy with 30 sec exposure. Data is presented as mean ± SE (n = 3). Statistical significance between groups is denoted by * ($p < 0.01$) with control, untreated samples compared against SWCNT-ANXA5 or NIR treated samples.

In vivo laser tolerance

Tolerance studies on mice without tumors were conducted to determine the optimal energy for NIR radiation which will cause the tumor bound SWCNT-ANXA5s to heat without affecting the remainder of the urothelium. Figure 4a depicts H&E results from mouse bladders treated with 50 and 100 J cm^{-2} NIR energy over 30 sec as compared to a control bladder. Treatment with 100 J cm^{-2} resulted in apparent change in the urothelium and muscle layer; however 50 J cm^{-2} led to no change.

In vivo SWCNT-ANXA5 specific tumor cell binding

In order to benefit from a targeted therapy, nonspecific binding needs to be minimized to prevent heating of healthy urothelial tissue. Anti-ANXA5 IHC confirmed that SWCNT-ANXA5s were specifically bound to the tumor, and no binding was seen along the healthy bladder wall within the same animal (figure 4b).

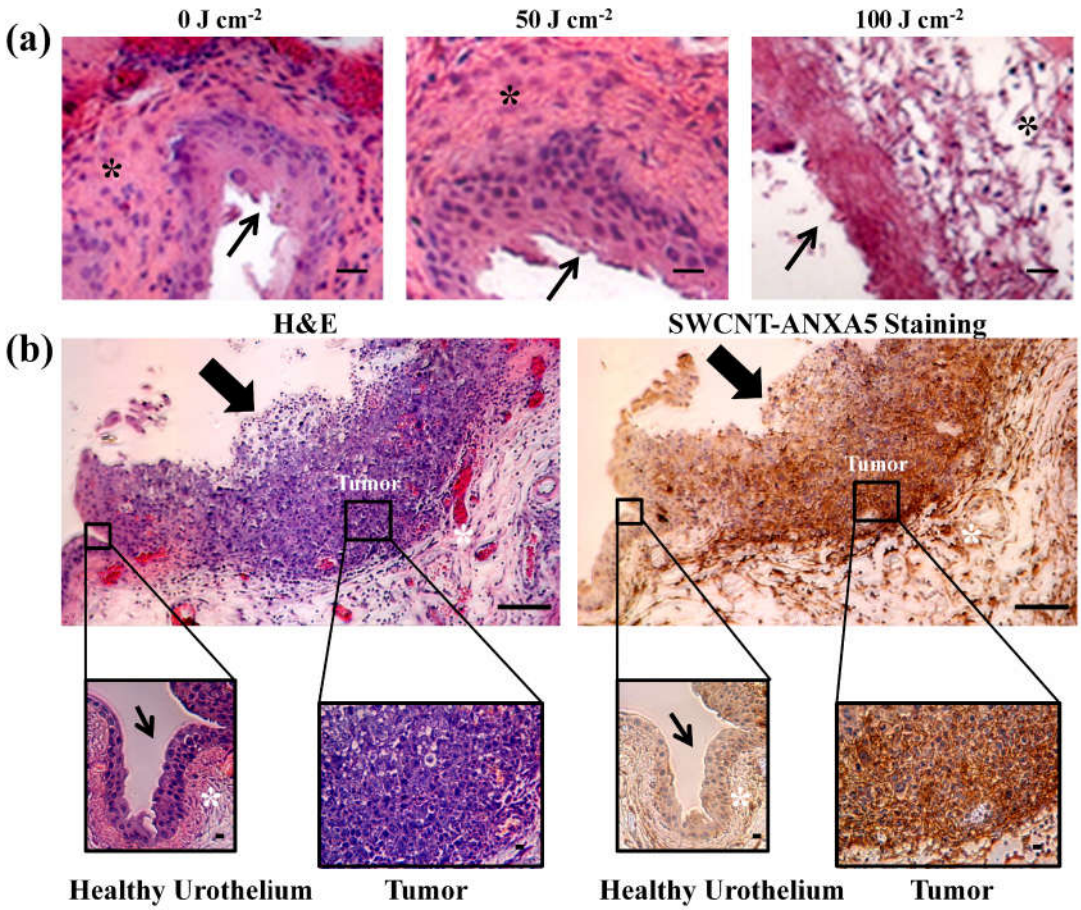

Figure 4. In vivo NIR tolerance and tumor specific SWCNT-ANXA5 binding. (a) Mice (n = 3) were treated with 0 J cm^{-2}, 50 J cm^{-2}, and 100 J cm^{-2} NIR energy for 30 sec. Representative histology images show change to the bladder wall and deeper muscle layer in mice treated with 100 J cm^{-2}. Mice treated with 50 J cm^{-2} NIR energy had no visible changes 24 h after irradiation. (b) Mouse with orthotopic bladder tumor was instilled with 100 µl of 20 mg l^{-1} SWCNT-ANXA5s for 90 min followed by bladder collection 24 h later when NIR laser would be applied. Within the same bladder, dark brown, positive anti-ANXA5 staining for SWCNT-ANXA5s is seen on the tumor while minimum staining is seen on the remainder of the urothelium. Thin arrow indicates healthy bladder wall, thick arrow indicates bladder wall with tumor, and * indicates muscle layer. Scale = 10 µm.

Biodistribution

NIR fluorescence spectroscopy along with a standard curve (data can be found in Figure 25 of Appendix A: Supplemental Data) was utilized to determine presence of 0.88 ± 0.13% of the injected dose (34.0 ± 10.6% ID/g of bladder) of SWCNT-ANXA5s in

bladders of mice with tumors 24 h after SWCNT-ANXA5 instillation. A long-term biodistribution study was also conducted on the clearance organs, liver and kidney, as well as the bladder of treated mice 116 days after tumor implantation to determine clearance. No detectable nanotubes were observed in any of the clearance organs or bladder.

In vivo tumor ablation

Following confirmation of SWCNT-ANXA5s binding to tumor and NIR tolerance, a short-term efficacy study was conducted for presence of tumors 24 h post treatment. As seen in figure 5a, mice treated with SWCNT-ANXA5s and NIR light combined had no detectable tumor fluorescence. A decrease in fluorescence is seen when the bladders are given SWCNT-ANXA5s or NIR alone; however all mice still had detectable fluorescence, which can eventually lead to tumor re-growth. H&E staining (figure 5b) confirmed no visible damage to the bladder of control or treated mice 24 h post-treatment.

Recurrence was evaluated by monitoring survival after one cycle of therapy compared to saline-treated mice as a control. The median survival was 34 days in the control group compared to 76 days in the treated group with 50% of the mice still alive at 116 days, when the study was ended (figure 5c). Trichrome staining (figure 5d) was conducted on the surviving treated mice to detect any collagen or scar tissue formation which would alter long-term normal bladder function. No scar tissue was observed.

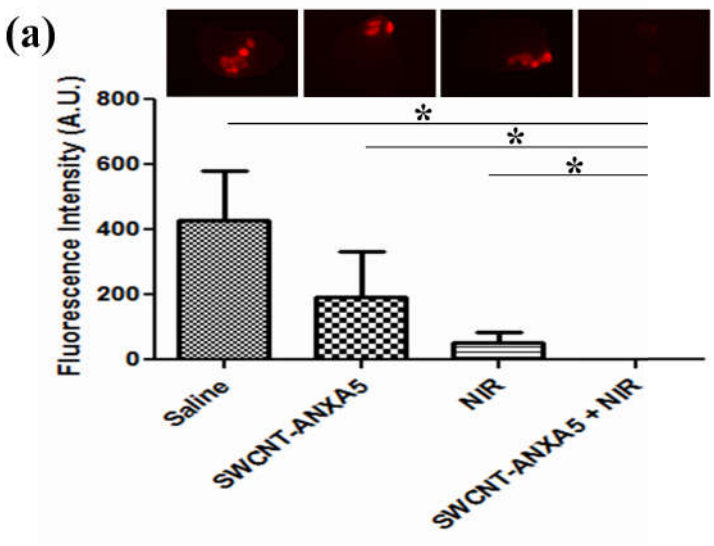
(a)
Fluorescence Intensity (A.U.)
800
600
400
200
0
*
*
*
Saline
SWCNT-ANXA5
NIR
SWCNT-ANXA5 + NIR

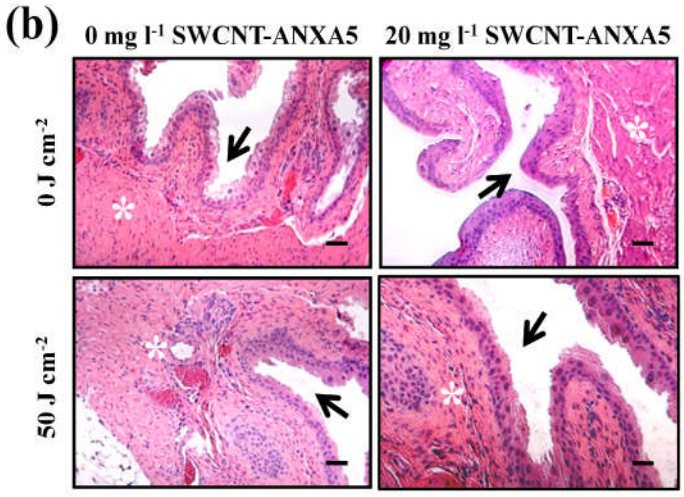
(b)
0 mg l-1 SWCNT-ANXA5
20 mg l-1 SWCNT-ANXA5
0 J cm-2
50 J cm-2

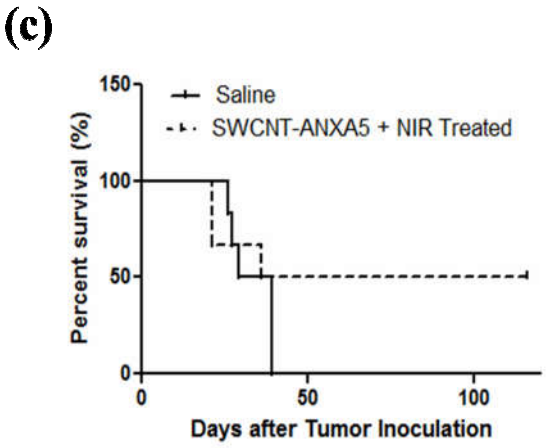
(c)
Saline
SWCNT-ANXA5 + NIR Treated
Percent survival (%)
150
100
50
0
0
50
100
Days after Tumor Inoculation

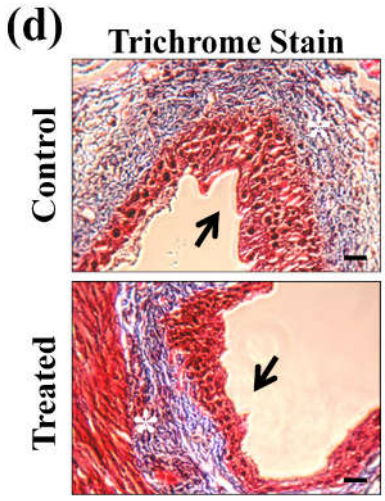

Figure 5. In vivo therapeutic efficacy study.
(a) MB49 orthotopic tumors were grown to simulate NMIBC. SWCNT-ANXA5s or PBS was delivered intravesically for 90 min. After 24 h to allow for nonspecific nanotube clearance, a diffusing fiber was used to deliver 50 J cm^{-2} NIR energy for 30 sec. Bladders were harvested 24 h after therapy to assess tumor presence via tdTomato fluorescence (representative images above graph). Data is presented as mean ± SE (n = 6). Statistical significance between groups is denoted by * ($p < 0.01$). (b) H&E staining was conducted on bladders 24 h after therapy. No visible signs of damage to the bladder were detected. (c) Survival of treated and control mice (n = 6) was monitored for recurrence of bladder cancer. All the control mice died within 39 days of tumor inoculation while half the treated mice were still living at 116 days when the study was terminated. (d) Trichrome staining was conducted on the surviving mice to determine if any damage incurred which may cause scar tissue formation and thus disrupt the normal mechanical function of a bladder. No scar tissue was observed within the surviving mice. Arrow indicates bladder wall and * indicates muscle layer. Scale = 10 μm.

Discussion

Bladder cancer has a high rate of recurrence due to incomplete resections as well as eventual chemotherapy resistance with no promising alternatives developed over the past 20 years [58]. A global heat based approach to recurrent, superficial bladder cancer shows promise as a viable therapeutic option to specifically heat the tumor with no apparent damage to the healthy urothelium. SWCNTs are conjugated to the protein annexin V via a PEG linker, which provides a stealth coating to make them more biocompatible and minimize the risk of eliciting an immune response [74]. ANXA5 is a mammalian protein which binds specifically and with high affinity only to bladder cancer cells, as seen on murine and human bladder cancer cells *in vitro* as well as on orthotopic MB49 tumors *in vivo*. The strong binding ensures that the heat being generated by the nanotubes is contained within the tumor region, thus minimizing nonspecific damage to the healthy bladder urothelium.

In addition to successfully treating bladder tumors, this study has also shown that there was no detectable long-term nanotube presence or toxicity from the photothermal therapy at 50 J cm^{-2} based on the following results: (1) the H&E analysis showing no visible damage to the bladder 24 h after treatment, and (2) the analysis of the mice surviving 116 days post-tumor instillation, which showed no nanotubes in the liver, kidney, or bladder as well as no scar tissue formation in the Trichrome stain. The 50 J/cm^2 energy level was used instead of 100 J cm^{-2} since the higher level was found to give some changes to the bladder wall in the study with only NIR light treatment (figure 4a). It is possible that lower than 50 J cm^{-2} energy could be used in combination with SWCNT treatment.

A recent study using a similar photothermal based approach for bladder cancer showed promising results with anti-EGFR coated gold nanoparticles; however delivery of the NIR light required surgery to expose the bladder, which is not as clinically translatable compared to the minimally-invasive intravesical NIR light delivery proven effective in this study [62]. A global NIR light also ensures that the entire bladder is treated at the same time, thus decreasing the possibility of incomplete treatment which is a major cause of recurrence currently. Our approach also requires significantly less power (1.7 W cm^{-2} versus 10 W cm^{-2} for the gold nanoparticles) which minimizes healthy tissue damage for a nonsurgical approach [62]. In contrast to the previous work, the proposed therapy also provides a unique adjuvant benefit of blocking PS, which is a global immunosuppressive signal in cancer [40]. A recent study tested the effects of blocking PS via ANXA5 and saw significant regression of tumor size as well as decreases in tumor angiogenesis factors that can be a synergistic addition to the novel therapy [36].

A preliminary 48 h study was conducted to evaluate the therapeutic efficacy of the proposed therapy along with a 24 h post-treatment period to observe any signs of therapy induced distress. No visible signs of discomfort or pain were observed. At the end of the study, bladders treated with only SWCNT-ANXA5s had some decrease in tumor presence, possibly due to the effect of the SWCNT-ANXA5s accumulating in the tumor cells in conjunction with the possible adjuvant nature of ANXA5 blockade of immunosuppressive PS [36, 40]. There is also a decrease in fluorescence for mice treated with only NIR laser, which might be due to the increased susceptibility of malignant cells to heat damage because of their reduced ability to efficiently dissipate

heat as seen in the *in vitro* tolerance study [59]. Although there were some decreases in tumor fluorescence for only SWCNT-ANXA5 or NIR treated mice, all mice still had tumors which will lead to recurrence. On the other hand, all mice treated with SWCNT-ANXA5s in combination with NIR had no detectable tumor presence 24 h post-therapy.

Since tumor re-growth is the major problem with the current standard of care treatment for NMIBC and results in 70% of patients having tumor relapse, a survival study was conducted comparing saline treated control mice and combination treated mice [8, 55-58]. The photothermal therapy resulted in a 50% cure rate in the survival study, which is higher than treatments used today. This is a remarkable result, given that this treatment consists of one 30 sec irradiation versus the usual combination of resection, chemotherapy, and immunotherapy for the current standard of care. The cure rate should be able to be increased by transitioning to a two- or three-cycle therapy to ensure all tumors are treated. No visible change was seen in the bladders treated with this therapy, making a multi-cycle therapy a possible alternative to further increase efficacy.

Conclusions

This study has shown success in the treatment of bladder cancer in mice with a targeted photothermal therapy using a very low dose of SWCNTs (0.1 mg SWCNTs kg^{-1}) delivered intravesically combined with a 30 sec NIR light treatment at a relatively low power density (1.7 W cm^{-2}). This treatment approach is much simpler and less invasive than for the current standard of care that normally consists of a combination of resection, chemotherapy, and immunotherapy, and in a 116 day survival study with only one cycle of therapy a higher cure rate was found compared to what patients now experience. It is also significant that no treatment toxicity was observed and no nanotubes were detected in the clearance organs or bladders at the end of the survival study. In future work, it would be desirable to evaluate the potential of a multi-cycle therapy since no signs of treatment toxicity were detected.

Chapter III: Targeted Single-Walled Carbon Nanotubes Thermal Ablation of Cancer via a Radiofrequency Field

Abstract

Single-walled carbon nanotubes (SWCNTs) are promising candidates for tumor ablative therapy because of their robust nature and high thermal conductivity. SWCNTs can be accumulated preferentially within cancerous tissue via annexin V (ANXA5) surface modification that selectively targets phosphatidylserine (PS) externalized on tumor cells and tumor vasculature. PS targeting of tumors has previously proven to be effective and very specific *in vitro* as well as *in vivo*. SWCNT-ANXA5s can be targeted to the tumors and mechanically excited via radiofrequency (RF) fields to generate a cell intolerable environment. The resonance of SWCNTs in the RF spectrum can be utilized as a noninvasive tool to thermally excite tumor targeting nanotubes above ablative temperatures (> 47°C). This study focuses on determining the resonance frequency of SWCNT-ANXA5s for future use as a noninvasive, targeted irradiation therapy for cancer.

Introduction

Most late stage tumor treatments focus on palliative therapy rather than a cure. Tumors become vascularized when they are as small as 2 - 3 mm^3, and are leaky and highly permeable due to the loss of tight junctions between endothelial cells [29, 31, 34]. A marker for tumor vasculature is phosphatidylserine (PS) which is internalized in healthy blood vessels but externalized in tumor vessels and tumor cells [35]. Annexin V (ANXA5) is an excellent marker for PS and can be used for targeted tumor therapies [7, 25, 37, 64, 75]

Radiofreuency (RF), which can deeply penetrate tissue (> 15 cm) and cause minimum damage to normal cells, can be utilized as an effective, noninvasive method for cancer treatment. RF based heat generation is dependent on the dielectric properties of the material which consists of permittivity, the ability to absorb and dissipate electrical energy as heat, and conductivity [76-78]. Raoof et al. compared the permittivity of liver and pancreatic tumors against normal tissue and found that the permittivity of both tumors was significantly higher than healthy tissue, explaining the highly preferential RF heating of the malignant regions [76]. The predisposition of RF tumor heating can be enhanced by the use of dielectric nanotubes to avoid damage of nonspecific regions such as the liver and spleen [79, 80].

In order to dissipate heat into cancerous tissue, nanotubes first need to generate thermal energy. Electromagnetic waves physically force nanotubes to vibrate due to the dipole formed from the buildup of opposing charges on the ends of the SWCNTs [81-86]. Heat is carried by acoustic phonons, which are defined as vibrations in the crystal lattice, and by electrons. In carbon materials, heat conduction is dominated by phonon

transport due to the strong sp^2 covalent bonding. There are two types of phonon transport regimes: diffusive and ballistic. Thermal transport is diffusive if the size of the sample (L) is much larger than the phonon mean-free path (Λ), which means that the phonon undergoes multiple scattering events. Conversely, if $L \ll \Lambda$, then thermal transport is ballistic and phonons can propagate without scattering [87]. Nanotube thermal conduction transitions from ballistic to diffusive with increasing temperatures as well as increasing length [19]. Figure 6 depicts phonon transport within a carbon nanotube.

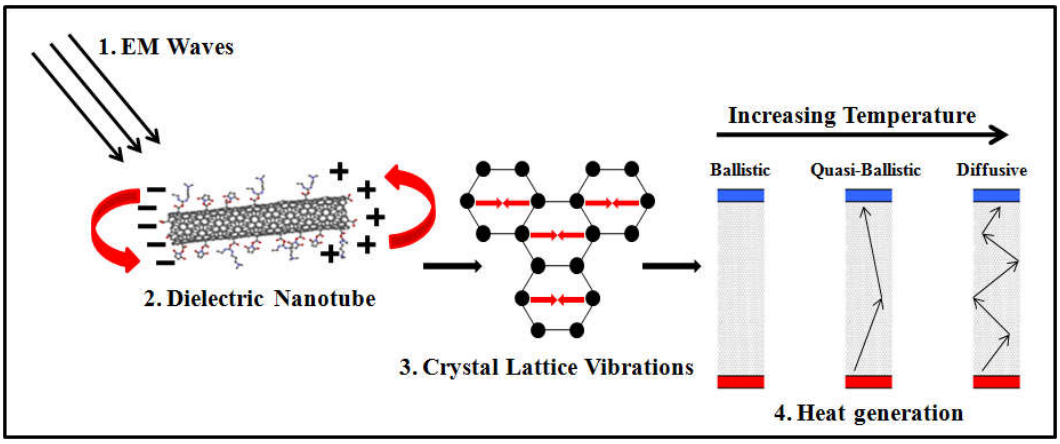

Figure 6. Schematic of electromagnetic waves inducing carbon nanotube heating. When struck with an (1) electromagnetic wave such as RF, (2) nanotubes act like dielectrics and physically vibrate. (3) Heat is generated by the vibrations of the crystal lattice or phonon transport. (4) As temperature increases phonon transport goes from a ballistic to a diffusive regime due to the decreasing mean free phonon path and increased scattering.

Nanotubes have a resonant frequency at which the amplitude of vibration is significantly higher than at any other frequency within the RF spectrum. Resonance of the nanotubes can be predicted using Euler-Bernoulli's beam theorem; however, it only takes into account length and diameter. Furthermore, the beam theory does not consider

the additional contributions of surface modifications (ANXA5 and PEGylation), number of nanotube shells, or nanotube chirality (metallic or semiconductive) [81-86, 88].

Although SWCNT resonance studies have been conducted, factors such as chirality and surface modification have not been taken into consideration. Most studies have focused on developing mathematical models to correlate with experimental data rather than optimizing SWCNT resonance for applications such as cancer ablative therapy [81-86, 89]. Previous studies involving noninvasive RF heating of cancer cells have focused on a single frequency (13.56 MHz) with untargeted and targeted gold nanoparticles to enhance the tumor ablation effect [76, 79, 90-94]. The novelty of this study is to improve tumor ablation by exploring mechanical resonances of SWCNT-ANXA5s within the RF spectrum that will produce a more effective system; this therapy will be further enhanced with an already established, highly specific tumor vasculature targeting mechanism. A schematic of the proposed targeted, ablative therapy is depicted in Figure 7.

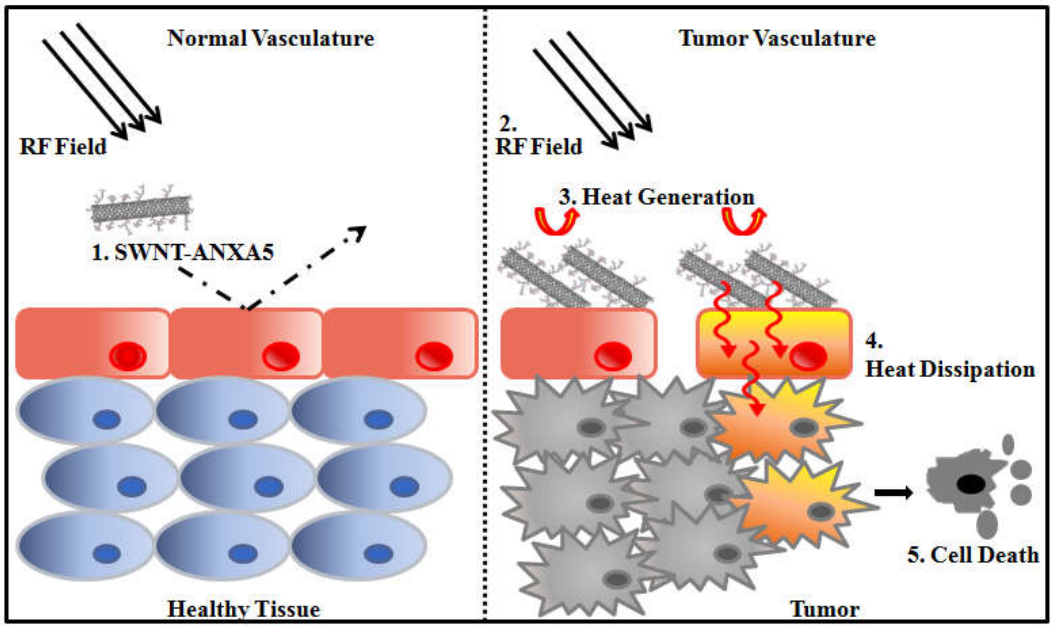

Figure 7. Schematic of tumor vasculature targeted ablative therapy.
(1) SWCNT-ANXA5s will be delivered systemically and bind preferentially to PS exposing tumor vasculature. (2) A RF field will be delivered and tumor bound SWCNT-ANXA5s will (3) generate heat which will be (4) dissipated into the surrounding cancerous tissue and lead to (5) cell death.

Materials and Methods

Materials

The plasmid encoding ANXA5, pET-30 Ek/LIC/ANXA5, was previously constructed in this lab [64].Bovine serum albumin (BSA), Alamar Blue reagent, Triton X-100, EDTA, and Tris-acetate-EDTA buffer were from Sigma-Aldrich (St Louis, MO). Sodium phosphate and sodium dodecyl sulfate (SDS) were from Mallinckrodt Chemicals (Phillipsburg, NJ). The 2 and 100 kDa dialysis membranes were from Spectrum Laboratories (Rancho Dominguez, CA). (6,5) CoMoCAT SWCNTs (average diameter 0.8 ± 0.1 nm, average length 1.5 ± .5 μm) were provided by Southwest Nanotechnologies, Inc. (Norman,OK). The 1,2-distearoyl-*sn*-glycero-3-phosphoethanolaminepolyethylene glycol-maleimide (DSPE-PEG-maleimide; PEG molecular weight of 3.4 kDa) linker was from Creative PEGWorks (Winston Salem, NC).

ANXA5 and SWCNT-ANXA5 production

Recombinant ANXA5 and the SWCNT-ANXA5 conjugate were produced as previously described [64]; the conjugation was performed using a DSPE-PEG-maleimide linker. ANXA5 was characterized via SDS-PAGE, and SWCNT-ANXA5s were characterized by UV-Vis-NIR spectroscopy.

Resonant Frequency Determination

Samples of SWCNT-ANXA5s (75 mg l^{-1}) were placed in glass vials and mounted in a five turn coil connected to a RF generator. SWCNT-ANXA5s rate of heating was

determined with a forward looking infrared (FLIR) thermal imager by measuring the temperature change every 30 sec. A buffer control was run at 45 MHz, which produced the highest SWCNT-ANXA5 heating rate, to confirm negligible buffer heating. The study was conducted by J.P.P's & Consulting, Inc. (Pleasanton, CA).

Results

In order to assess the validity of an improved thermal ablation therapy due to SWCNT-ANXA5 resonance within the RF spectrum, preliminary studies by J.P.P's & Consulting, Inc. were conducted (figure 8). As frequency increased, the rate of heating increased exponentially.

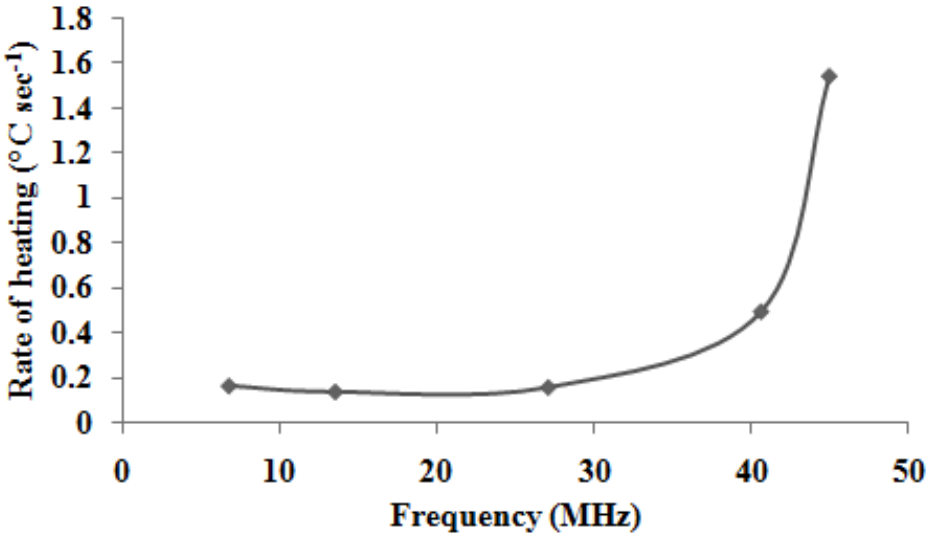

Figure 8. Resonance frequency analysis.
Preliminary analysis conducted by J.P.P's & Consulting, Inc. at a concentration of 75 mg l^{-1} SWCNT-ANXA5 and a volume of 1 ml. Change in temperature was determined with a FLIR thermal imager.

A similar study was conducted within our lab to determine the SWCNT-ANXA5 (75 mg l^{-1}) rate of heating by a 980 nm near-infrared (NIR) laser, which has been effective in causing *in vivo* tumor eradication for breast and bladder cancer. The rate of heating was determined to be 0.603°C sec^{-1} (T_i = 25.3°C and T_f = 43.39°C) at a power of 3.67 W cm^{-2} for 30 sec which is lower than the 45 MHz (1.088°C sec^{-1}) but higher than the

13.56 MHz (0.095°C sec^{-1}) rate, which has previously been reported to cause SWCNT based thermal ablation [95].

Discussion

As mentioned previously, SWCNTs have a mechanical resonance within the radiofrequency range that can be exploited to improve their rate of heating. It is expected that at the resonance frequency, the rate of heating will be at its maximum [17, 86, 96, 97]. Euler-Bernoulli's beam model is a simplified theory of elasticity which can be used estimate the resonance frequency of a SWCNT based on length and diameter [82-86, 88]. The mechanical resonance frequency can be predicted by equation 1 [82-86, 88]:

$$f_i = \frac{\beta_i^2}{8\pi}\frac{1}{L^2}\sqrt{\frac{(D_o^2 \quad D_i^2)E}{\rho}}$$

Equation 1. Euler-Bernoulli's beam model for mechanical resonance frequency. f_i is the resonance frequency, β_1 is 4.73 for the first harmonic [83, 85], L is the length, D_o and D_i are the outer and inner diameters respectively, E is the Young's modulus which is 1 TPa [83, 85], and ρ is the density which is 0.094 g cm^{-3} (SWeNT, Inc.).

By solving the preceding equation with the known parameters, $f_i = 42\ MHz$; however this does not take into account the ANXA5 molecules on the surface, the chirality, and any defects in the SWCNTs. As seen in the results above, even though the expected resonance is around 42 MHz, no peak is seen up to 45 MHz. In order to determine the true resonance, further experimental tests will need to be conducted.

A previous study combining SWCNTs with 13.56 MHz RF was conducted with promising results [95]. The SWCNTs were directly injected into the hepatic xenograft tumors of rabbits followed by 800W of RF for 2 minutes. Complete tumor necrosis was

reported 48 h post-therapy compared to the mice treated only with RF. Compared to the previous study, our approach is further advantageous by 1) using targeted nanotubes which specifically bind to tumors over healthy tissue, 2) eliminating the need for intratumoral injections, and 3) the resonance frequency of the nanotubes will be used to deliver more heat in a short period leading to complete primary and secondary tumor death.

The overall objective of targeting the nanotubes via the ANXA5-PS interaction is to localize a highly concentrated SWCNT-ANXA5 solution within the tumor as compared to the other organs. When a RF field is applied, tumor sites will be treated because of a higher rate of heating compared to the surrounding organs. Previous literature has shown that SWCNT concentration and rate of heating have a linear relationship and that there is preferential heating of tumor sites with just RF fields, which can be enhanced by localized nanoparticles [79, 95]. A previous study confirmed the lack of acute or chronic damage because of RF heating of healthy tissue with nonspecific nanoparticle accumulation [79].

Conclusions

The work conducted in this study will be a stepping stone for an ablative therapy that can be translated relatively easily for clinical treatment of tumors. In order to evaluate the full potential of this regime, further testing into a wider RF range will need to be assessed to determine the optimal peak while still maintaining whole body penetration for a noninvasive treatment alternative. A network analyzer is being developed to test a wider range of RF frequencies to determine resonance (schematic of network analyzer can be found in Figure 26 of Appendix A: Supplemental Data). Further testing of biodistribution will need to be conducted to evaluate any cytotoxic effects due to acute SWCNT-ANXA5 accumulation. Blood clearance will also need to be assessed in order to ensure that the RF field will not affect normal tissue. Combining SWCNT-ANXA5 with RF has promising potential for a clinically relevant, noninvasive option for cancer treatment.

Chapter IV: Enzyme Prodrug System in Combination with Immunostimulation for Treatment of Metastatic Ovarian Cancer

Abstract

Approximately 75% of ovarian cancer is diagnosed once metastasis to the peritoneal cavity has occurred, which results in a 70% mortality rate. The current treatment option includes a combination of a cytoreductive surgery with platinum-based chemotherapy given intraperitoneally or intravenously. A large proportion of patients quickly develop platinum-resistive tumors, which are considered terminal. In order to provide an alternative for resistive tumors as well as decrease mortality rates, a novel fusion protein, mCTH-ANXA5, has been developed for the treatment of high grade, metastatic ovarian cancer. The fusion protein combines annexin V (ANXA5), an ovarian tumor and tumor vasculature targeting protein, with a mutated cystathionine gamma-lyase (mCTH), an enzyme converting selenomethionine (SeMet) into toxic methylselenol. The fusion protein is targeted to the tumor followed by addition of a nontoxic prodrug, SeMet, which is locally converted into a cytotoxic reactive oxygen species (ROS) generating drug, methylselenol. Excess ROS causes oxidative stress leading to DNA, membrane, and mitochondrial damage and eventual tumor cell death. In order to further enhance the therapeutic efficacy of this system, anti-CD73 and anti-OX40 immunostimulants were combined to produce a significant increase in survival from 45 days for untreated to 57 days for treated mice, and a decrease in tumor burden in mice with orthotopic metastatic ovarian tumors. Further evaluation of the combination therapy revealed a strong antibody-mediated immune response, and an increase in infiltration of cytotoxic T-cells along with a decrease in tumor promoting immune cells

such as myeloid-derived suppressor cells and regulatory T-cells. This study demonstrates the efficacy of a synergized, multi-drug system by attacking the tumor as well as enlisting the body's own defense system to treat the patient.

Introduction

Ovarian cancer has a 70% mortality rate largely due to 75% of diagnoses occurring after metastases to the peritoneal cavity [98]. The current standard of care is a cytoreductive surgery followed by platinum-based chemotherapy delivered intraperitoneally, which increases tumor free survival by only 5-months. Novel therapies for metastatic ovarian cancers need to be developed, which will increase tumor free survival as well as avoid aggressive surgery that increases the chances of complications [98]. A novel enzyme prodrug system is proposed in combination with immunostimulation for the treatment of aggressive, metastatic ovarian cancer.

An enzyme prodrug approach is a two-step therapy that involves the delivery of a drug activating enzyme to the tumor followed by a nontoxic prodrug that is converted into a highly toxic drug by the enzyme [22, 23]. To be considered a successful enzyme prodrug therapy, a few key requirements need to be met: 1) the enzyme should be nonhuman or absent/minimally expressed in normal tissue, 2) the enzyme must remain highly active once at the tumor, 3) the prodrug must be activated by the tumor specific enzyme but not by endogenous enzymes in the remainder of the body, 4) the prodrug and activated drug must be highly permeably to allow for a bystander effect, 5) the half-life of the drug must be optimal to allow for diffusion into the surrounding cancer cells but limit systemic leakage, and 6) there must be a high therapeutic index between the prodrug and the drug [22, 23]. We have developed a novel enzyme prodrug system combining a fusion protein composed of the targeting protein annexin V (ANXA5) with mutated cystathionine gamma-lyase (mCTH) enzyme and selenomethionine, a nontoxic prodrug.

The fusion protein is composed of ANXA5, which specifically and strongly binds to phosphatidylserine (PS) that is exposed on tumor cells and tumor vasculature [7, 25, 26, 37]. PS is normally internalized on healthy cells, thus reducing the chances of nonspecific accumulation and eventual toxicity of the fusion protein. The second part of the fusion protein is composed of mCTH, an enzyme that generates a local cytotoxic agent against tumor cells. Cystathionine gamma-lyase (CTH) is a mammalian enzyme that breaks down cystathionine into cysteine, α-ketobutyrate, and ammonia [25]. Wild type CGL has no activity towards selenomethionine; however three point mutations to the enzyme (mCTH) allows it to develop catalytic activity to the prodrug, selenomethionine (SeMet), and generate a highly toxic drug, methylselenol, which generates reaction oxygen species (ROS) [99]. Increased ROS accumulation induces oxidative stress and leads to membrane, mitochondrial, and DNA damage with eventual cell death [25, 100, 101].

The mutant CTH (mCTH) also has activity towards conversion of methionine into methanethiol, α-ketobutyrate, and ammonia, which has been proposed to aid in the regression of multiple tumors including human ovarian cancers [102]. Methionine is a key amino acid that is used in protein synthesis as well as the *de novo* pathway or methylation cycle in cell function [102, 103]. Through the *de novo* pathway, methionine gets converted into homocysteine. Homocysteine is then converted into glutathione, which reduces ROS, through the trans-sulfuration pathway [102, 103]. In normal cells, homocysteine is methylated back into methionine making the cells methionine-independent; however, cancer cells either lack or have mutated forms of methionine synthase which methylates homocysteine, thus blocking their source of a key amino

acid, methionine, and making them methionine-dependent [102, 103]. mCTH-ANXA5 in conjugation with the prodrug SeMet can provide a dual mechanism for human ovarian cancer death by: 1) converting nontoxic SeMet into a ROS generating toxic drug and 2) depriving cells of methionine that in turn limits the amount of glutathione produced, which actively reduces ROS to protect the cell from oxidative stress [102, 103].

In conjunction with the enzyme prodrug system, immunostimulant combinations of anti-PD-1, anti-CD73, and anti-OX40 are studied to determine the most synergistic immune system activators. PD-1 ligands are present on tumor cells as inhibitory surface markers that interact with PD-1 receptors on T-cells to render them anergic, exhausted, or dead, thus preventing a T-cell mediated immune response and tumor cell clearance [104-108]. Upregulation of PD-1 expression has been associated with higher grade ovarian tumors with poor prognosis and a high risk of recurrence [104-107]. Anti-PD-1 blockade of the PD-1 receptors present on T-cells may prevent the interaction of tumor PD-1 ligands with immune cells and minimize immune suppression.

Another key immune modulator, CD73, participates in the conversion of adenosine monophosphate (AMP) into adenosine, which is an immunosuppressive molecule. Adenosine interacts with A_{2A} receptors on regulatory and effector T-cells [108-110]. On regulatory T-cells, A_{2A} receptor activation by adenosine triggers a positive feedback loop to promote regulatory T-cell expansion and immunsuppressive chemokine production, which in turn promotes more cell expansion. On the other hand, A_{2A} receptor activation on effector T-cells inhibits immune promoting cytokines and cell proliferation. CD73 has also been shown to be specifically upregulated in human

ovarian cancer cells, and there is a strong correlation between increased expression of CD73 and severity of tumor grade [108, 110, 111]. Due to this upregulation, anti-CD73 antibodies are proposed as a combinatorial approach with the enzyme prodrug system to decrease adenosine production and promote proliferation of effector T-cells and downregulation of regulatory T-cells.

Since anti-PD-1 and anti-CD73 blockade work to promote effector T-cell recruitment and activation, anti-OX40 was evaluated due to its co-stimulatory function on effector T-cell activation and regulatory T-cell augmentation [107, 112, 113]. OX40 is expressed by effector T-cells following T-cell receptor recognition by antigen presenting cells to stimulate activation. In order to promote activation of tumor recognizing effector T-cells, anti-OX40 is administered to act as a co-stimulatory signal to promote tumor regression.

Due to the increasing evidence of a strong correlation between increased CD73 presence and high grade, metastatic ovarian cancer as well as the co-stimulatory activation mechanism of anti-OX40, it is hypothesized that combining anti-CD73 and anti-OX40 with a targeted ROS generating therapy will result in a decrease in metastatic ovarian cancer. Figure 9 depicts a schematic of the multi-pronged approach proposed. This study demonstrates that mCTH-ANXA5 with SeMet alone can cause a decrease in tumor burden; however the addition of anti-CD73 and anti-OX40 significantly decreased overall tumor weight and increased survival of mice against untreated, saline control as well as mice treated with only the enzyme prodrug system. The addition of anti-CD73 and anti-OX40 also caused an increase in cell-mediated immunity by increasing the tumor infiltrating ratio of cytotoxic T-cells to tumor

suppressing immune cells. There is also a significant increase in antibody-mediated immunity when combining anti-CD73 and anti-OX40 with mCTH-ANXA5 and SeMet versus either antibody alone or the control, untreated mice. The overall increase in survival, decrease in tumor burden, and increase in immune response sheds promise on the use of a combinatorial approach of mCTH-ANXA5, SeMet, anti-CD73, and anti-OX40 as an alternative therapy for high grade, metastatic ovarian cancer.

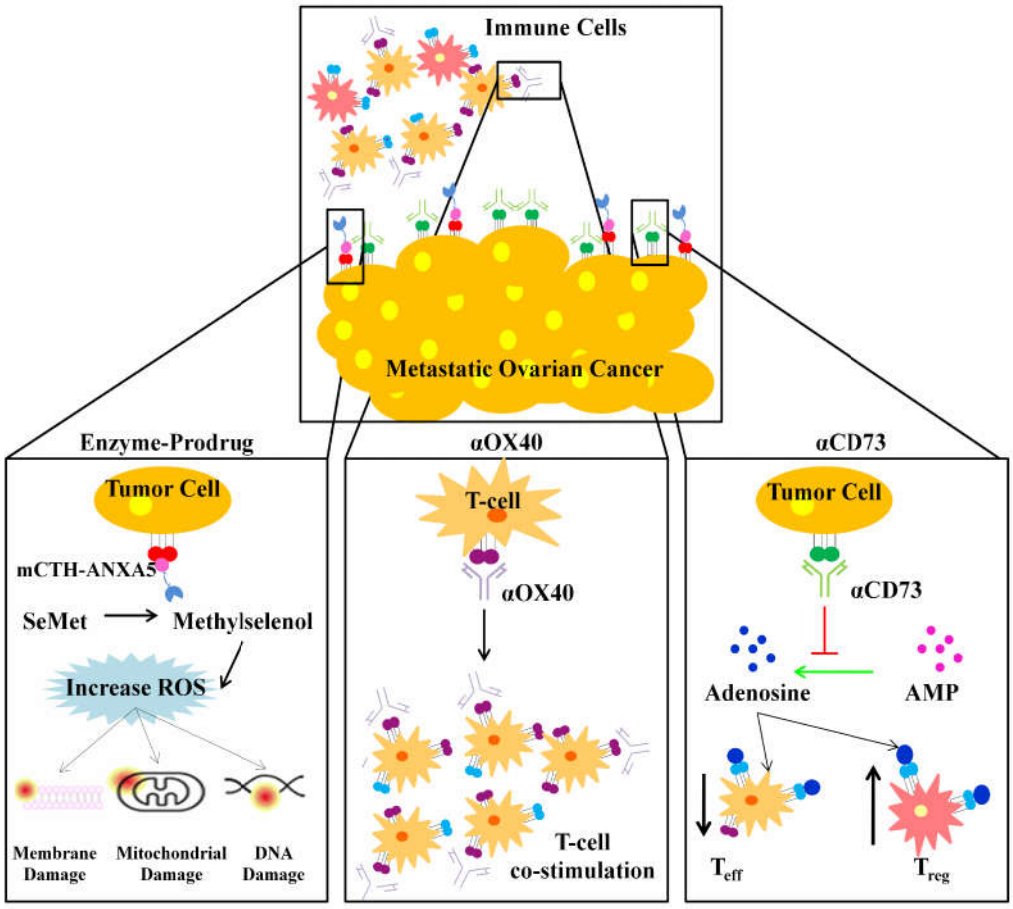

Figure 9. Schematic of the proposed therapy.
This therapy combines an ROS generating enzyme prodrug system mCTH-ANXA5/SeMet with immunostimulatants, anti-OX40 and anti-CD73, for a synergistic approach to metastatic ovarian cancer. The enzyme prodrug system involves delivery of a fusion protein with ANXA5 on one end to bind specifically to phosphatidylserine expressing tumor cells and tumor vasculature, and mutated cystathionine gamma-lyase

(mCTH) on the other end. Following unbound mCTH-ANXA5 clearance, a nontoxic prodrug, selenomethionine (SeMet), is delivered and converted locally by the fusion protein into a toxic drug, methlyselenol, which generates reactive oxygen species (ROS). ROS causes tumor cell death by damaging the cell membrane, mitochondria, or DNA as seen in the left panel. Mice are treated with the enzyme prodrug system to induce tumor regression and increase overall survival. Immunostimulants, anti-OX40 (αOX40) and anti-CD73 (αCD73), are delivered to activate an immune response towards the tumor. Anti-OX40 (middle panel) binds to OX40 present on T-cells as a co-stimulatory molecule to keep them activated and cause expansion once they are primed by antigen presenting cells to attack the tumor. Anti-CD73 (right panel) binds to CD73 receptors on tumor cells, which converts adenosine monophosphate (AMP) into adenosine. Adenosine interacts with A_{2A} receptors on effector and regulatory immune cells to decrease proliferation of tumor suppressing immune cells and increase expansion of tumor promoting immune cells.

Materials and Methods

Materials

The plasmid encoding mCTH-ANXA5, pET-30 Ek/LIC-mCTH-ANXA5, was previously constructed in this lab [25]. Bovine serum albumin (BSA), Alamar Blue reagent, Triton X-100, EDTA, selenomethionine, and Tris-acetate-EDTA buffer were from Sigma-Aldrich (St Louis, MO). Sodium phosphate and sodium dodecyl sulfate (SDS) were from Mallinckrodt Chemicals (Phillipsburg, NJ). Paraformaldehyde was from Electron Microscopy Sciences (Hatfield, PA). Antifade reagent Fluoro-gel, borate buffer, streptavidin coated ELISA plates, Alexa-488, Deep Red Plasma Membrane stain, DAPI, flow cytometry staining buffer, fixation/permeabilization buffer, permeabilization buffer, and Slide-A-Lyzer dialysis cassettes (3.5 kDa) were from Thermo Fisher Scientific (Waltham, MA). The 2 and 100 kDa dialysis membranes were from Spectrum Laboratories (Rancho Dominguez, CA). Dulbecco's Modified Eagle cell medium was from ATCC (Manassas, VA). Fetal bovine serum (FBS) was from Atlanta Biologicals (Lawrenceville, GA). Antibiotics, penicillin and streptomycin, were from Invitrogen (Grand Island, NY). All antibodies were from BioLegends (San Diego, CA). All immunostimulants were from BioXcell (West Lebanon, NH).

Cell lines and culture conditions

ID8 $p53^{-/-}$ cells were a gift from Dr. McNeish. The cell line was grown in Dulbecco's Modified Eagle's Medium (DMEM) with glucose and was enriched with 4% fetal bovine serum (FBS), 1X insulin transferrin selenium (ITX-100), and

penicillin/streptomycin antibiotics (100 U ml^{-1} and 100 μg ml^{-1}, respectively). Cells were grown at 37°C with 5% CO_2.

mCTH-ANXA5 production

Recombinant mCTH-ANXA5 was produced and analyzed via SDS-PAGE and a methionine activity assay was conducted as previously described [25].

Binding strength

The dissociation constant for mCTH-ANXA5 was determined as previously described [25] using biotin conjugated mCTH-ANXA5 on 70% confluent ID8 $p53^{-/-}$ cells. Specific binding was determined by subtracting total binding (medium supplemented with calcium) from nonspecific binding (medium supplemented with EDTA).

Fluorescent microscopy of SWCNT-ANXA5in vitro

ID8 $p53^{-/-}$ cells were grown to 70% confluence on cover slips. mCTH-ANXA5 was tagged with Alexa-488 following the company's protocol. mCTH-ANXA5-Alexa-488 (100 nM) in 2 mM $CaCl_2$ was incubated with ID8 $p53^{-/-}$ cells for 2 h followed with PBS washing. Cells were fixed in 4% paraformaldehyde, and the nucleus and plasma membrane were stained with DAPI and Deep Red Plasma Membrane stain, respectively. Images were taken on a Nikon fluorescence microscope.

In vitro cytotoxicity studies

Alamar Blue cell viability assays were conducted to determine the cytotoxic effects of mCTH-ANXA5 combined with SeMet on ID8 $p53^{-/-}$ cells over 3 days in 24-well plates as previously described [25].

Mouse tumor models and treatments

All procedures complied with a protocol approved by Institutional Animal Care and Use Committee (IACUC) of the University of Oklahoma Health Sciences Center. C57BL/6J female mice 6 weeks of age, weighing 18 – 20 g were used. Mice were on a standard chow diet. Mice were injected with 5 x 10^6 ID8 $p53^{-/-}$ cells by intraperitoneal (i.p.) injection. Mouse body weight was monitored every 3-4 days. Mice bearing ID8 $p53^{-/-}$ tumors were randomized into groups (6 to 9 per group) prior to initiation of treatment 2 weeks after inoculation. mCTH-ANXA5 fusion protein (10 mg/kg) was administered over 21 days either daily, every 3 days, or every 7 days by i.p. injection. SeMet (5 mg/kg i.p.) was administered 10 h post-fusion protein. Immunostimulants, anti-OX40 (10 mg/kg i.p.), anti-CD73 (5 mg /kg i.p.), and anti-PD-1 (5 mg/kg i.p.), were administered on days 10, 14, and 18 post-tumor inoculation as seen in figure 10. Mice were euthanized once ascites development occurred or animals seemed distressed, and tumor, blood, and organs were collected.

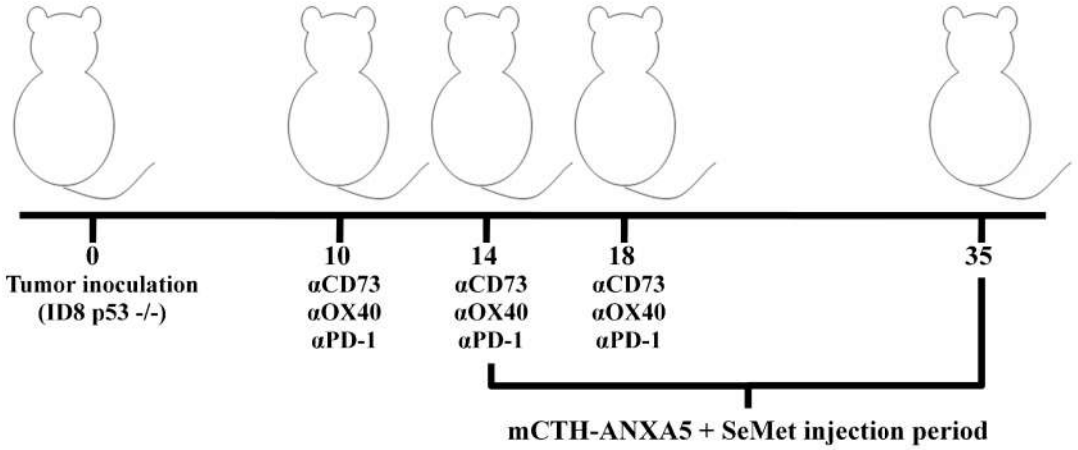

Figure 10. Study progression timeline.
C57BL/6J mice are inoculated with 5 x 10^6 ID8 $p53^{-/-}$ cells i.p., and tumors are grown for 10 - 14 days. Combinations of anti-CD73 (αCD73), anti-OX40 (αOX40), and anti-PD-1 (αPD-1) are given i.p. 10, 14, and 18 days post-tumor inoculation. The enzyme prodrug system, mCTH-ANXA5 with SeMet, is given over a 21 day period either daily, every 3 days, or once a week. The fusion protein, mCTH-ANXA5, and the prodrug, SeMet, are given 10 h apart.

In vivo mCTH-ANXA5 toxicity

Mice with orthotopic ovarian tumors were treated for 1 week with the complete combination therapy, mCTH-ANXA5 with SeMet, anti-CD73, and anti-OX40. The mice were euthanized 24 h later, and the liver, lungs, kidney, and heart were collected for H&E. Images were taken on a Zeiss light microscope.

Flow Cytomerty Analysis

Mice were euthanized 21 days post-inoculation, and the mesenteric lymph nodes were collected for flow cytometry analysis (more details can be found in Appendix C: Laboratory Protocols). Lymph nodes were kept in DMEM media on ice until use. Lymph nodes were mechanically dissociated with tweezers and strained through a 70 μm filter with 3 ml of flow cytometry staining buffer. Strained cells were centrifuged at

1000 g for 5 min and the supernatant was discarded. Another 3 ml of flow cytometry buffer was added to resuspend and recentrifuge the cells. Cells were counted and resuspended in flow cytometry buffer to a final concentration of 10 x 10^6 cells ml^{-1}. Cells (100 µl) were stained (stain 1) for myeloid-derived spleen cells (MDSCs), macrophages, CD8+ T-cells, and regulatory T-cells separately with 50 µl antibody mixture for 1 h at 4°C, protected from light. Antibody cocktails for each cell stain are listed in table 1, and flow cytometry staining buffer was used to bring the final volume to 50 µl. Cells were washed three times with 1 ml of flow cytometry staining buffer followed by 5 min of centrifuging at 1000 g; the supernatant was discarded each time and cells were resuspended in 1 ml of fresh flow cytometry staining buffer. After the last wash, cells were suspended in 1 ml of fixation/permeabilization working solution for 1 h at 4°C, protected from light. Cells were washed three times with 1 ml of permeabilization buffer followed by 5 min of centrifuging at 1000 g; the supernatant was discarded each time and cells were resuspended in 1 ml of fresh permeabilization buffer. After the last wash, cells were suspended in 100 µl of permeabilization buffer with 2 µl of 2% bovine serum albumin (BSA) for 15 min at 25°C, protected from light. Without washing, either 2.5 µl PE-FoxP3 or permeabilization buffer (stain 2) was added to the cells for 30 min at 25°C, protected from light. Cells were washed three times with 1 ml permeabilization buffer followed by 5 min of centrifuging at 1000 g; the supernatant was discarded each time, and cells were resuspended in 1 ml of fresh permeabilization buffer. After the last wash, cells were suspended in 500 µl of flow cytometry staining buffer and analyzed via a BD Accuri C6 flow cytometer (San Jose, CA).

	Stain 1			Stain 2		
Cells	**Antibodies**	**Concentration (mg ml^{-1})**	**Volume (µl)**	**Antibodies**	**Concentration (mg ml^{-1})**	**Volume (µl)**
MDSC	APC-CD11b	0.2	1.25	Permeabilization buffer	-	2.5
	PerCP-Ly-6C	0.2	1.25			
	FITC-Ly-6G	0.5	0.5			
Macrophages	APC-CD11b	0.2	1.25	Permeabilization buffer	-	2.5
	PE-F4-80	0.2	1.25			
CD8+ T-cells	APC-CD8	0.2	1.25	Permeabilization buffer	-	2.5
	PE-Cy7-CD3e	0.2	2.5			
Regulatory T-cells	APC-CD25	0.2	0.3	PE-FoxP3	0.2	2.5
	FITC-CD4	0.2	0.625			

Table 1. Antibodies for flow cytometry analysis.
Flow cytometry staining for immune cells from the mesenteric lymph nodes of C57BL/6J mice were analyzed to evaluate the effect of immunostimulantion.

Antibody Titers

ID8 p53$^{-/-}$ cell specific antibody titers were determined based on modified protocols from [114, 115]. ID8 p53$^{-/-}$ cells were grown to 70% confluence on a 96-well plate. Blood samples were collected from mice on day 21 post-inoculation. A sandwich ELISA assay was performed by incubating cells with various plasma dilutions at 37°C for 2 h. Plates were washed with media and incubated with HRP conjugated goat anti-mouse IgG and IgM (1:5000 dilution). Excess IgG and IgM were washed with media and a colormetric analysis was conducted with *o*-phenylenediamine (OPD) for quantification on a BioTek Synergy plate reader. A standard curve with different concentrations of HRP conjugated goat anti-mouse IgG and IgM was generated (more details can be found in Appendix C: Laboratory Protocols).

Statistics

Statistical significance of *in vitro* cell survival and *in vivo* tumor weight and immune response studies was assessed using a one-way ANOVA and Tukey-Kramer multiple comparisons test with GraphPad Prism software. Statistical significance for survival was assessed using the log-rank (Mantel-Cox) test with a 0.05 significance level.

Results

In vitro binding and cytotoxicity

The dissociation constant of mCTH-ANXA5 binding to ID8 $p53^{-/-}$ cells was 18.5 ± 6.1 nM, confirming a strong affinity of mCTH-ANXA5 for ovarian cancer cells (data can be found in Figure 27 of Appendix A: Supplemental Data). Fluorescence microscopy (figure 11a) was used to visualize the interaction of Alexa-488 tagged mCTH-ANXA5 and ovarian cancer cells *in vitro*. A previous study has shown that mCTH-ANXA5 also has a strong binding affinity for endothelial cells representative of PS exposure of the tumor vasculature [25].

In addition to binding, the cytotoxic efficacy of a ROS damage based system was proven effective *in vitro* on ovarian cancer cells as seen in figure 11b. Significant cell death is seen after only one dose of mCTH-ANXA5 and 2 days of 50 μM SeMet, with increasing cytotoxicity at increasing concentrations of SeMet. Minimal toxicity is seen with cells treated with only SeMet at the same concentrations.

(a)

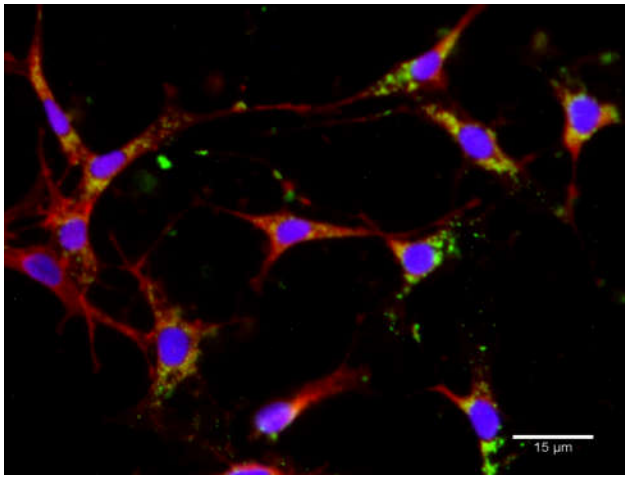

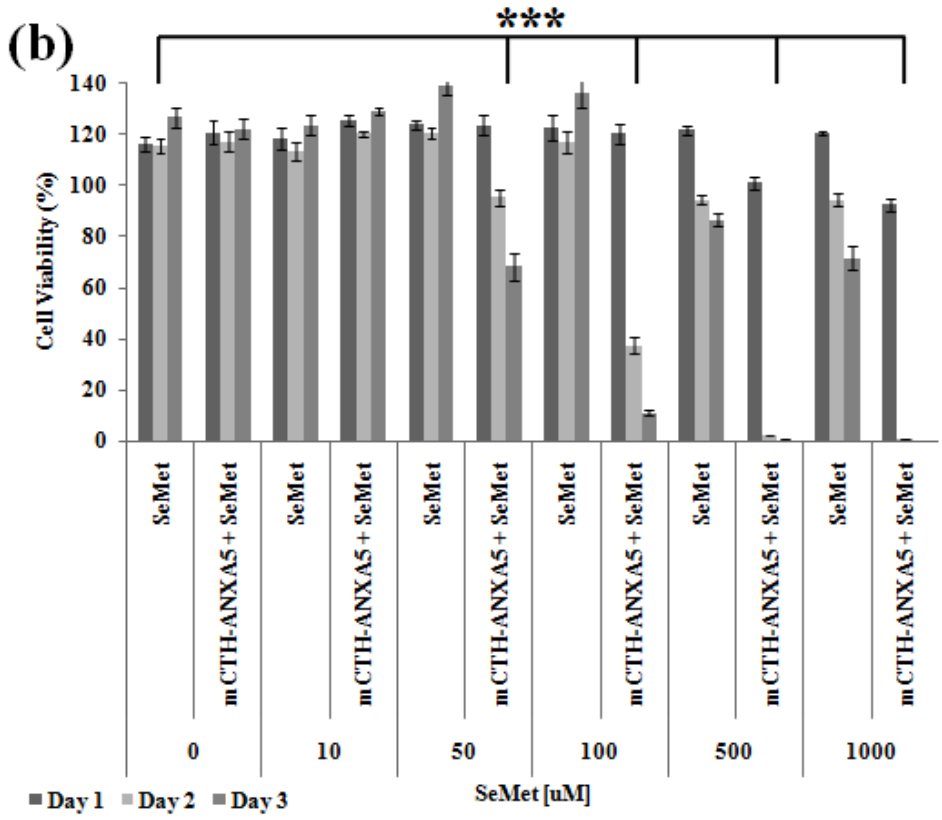

Figure 11. In vitro binding specificity and cytotoxicity of the enzyme prodrug system.
(a) Fluorescence imaging confirming mCTH-ANXA5 binding to ovarian cancer cells. Deep red stained plasma membrane (red), Alexa-488 labeled mCTH-ANXA5 (green), and DAPI stained cell nucleus (blue). Scale = 15 µm. (b) Cytotoxicity of murine (ID8 $p53^{-/-}$) ovarian cancer cells to increasing concentrations of SeMet in the presence of mCTH-ANXA5 was determined. Data is presented as mean ± SE (n = 3). Statistical significance between groups is denoted by *** ($p < 0.001$) with control, untreated cells compared against enzyme prodrug treated cells.

In vivo fusion protein dosage study

A dosage study was conducted by delivering the enzyme prodrug system every day, every 3 days, or once a week to determine the most effective cycle of treatment that would induce greatest tumor regression with the lowest drug dose. As seen in figure 12a, delivering the enzyme prodrug system every day or every 3 days gave tumor

regression; however, a continuous delivery of the enzyme prodrug system every day yielded the greatest decrease in final tumor load 2 weeks after the end of the study.

In vivo immunostimulant combination study

Combinations of anti-PD-1, anti-CD73, and anti-OX40 were tested in conjunction with the enzyme prodrug system to evaluate the synergistic nature of a clinically relevant multi-pronged therapy approach. Figure 12b depicts the tumor volumes of mice 2 weeks after therapy ended with three doses of the respective immunostimulant combinations and 21 days of enzyme prodrug treatment. The greatest decrease in tumor volume and synergism occurred between the enzyme prodrug system and combinations of anti-PD-1 and anti-OX40 as well as anti-CD73 and anti-OX40; however between the two immunostimulant combinations, anti-PD-1 and anti-OX40 caused more animal distress. All further studies were conducted with anti-CD73 and anti-OX40 treated mice.

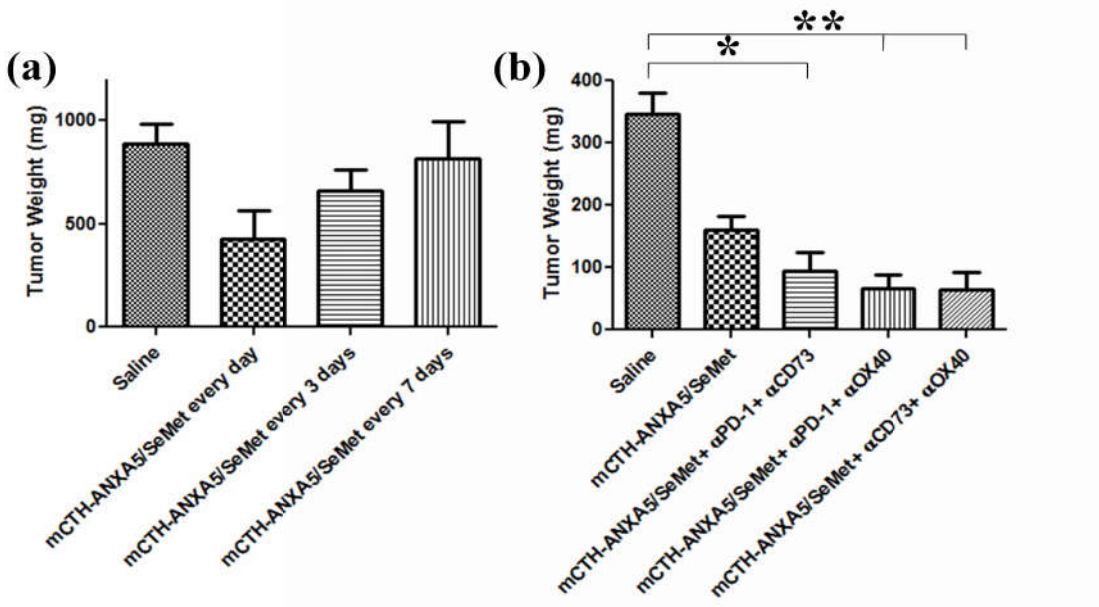

Figure 12. Enzyme prodrug system dosage and immunostimulant study. Treatment started 2 weeks after inoculation with 5 x 10^6 ID8 $p53^{-/-}$ cancer cells. Tumor weight 2 weeks post-therapy is shown. (a) Mice were treated with mCTH-ANXA5 and SeMet daily, every 3 days, or every 7 days to optimize dosage. (b) A pilot study comparing the synergistic effect of different combinations of immunostimulants with the enzyme prodrug system administrated daily. Immunostimulants, anti-PD-1 (αPD-1), anti-CD73 (αCD73), and anti-OX40 (αOX40), were administrated on days 10, 14, and 18 post-tumor inoculation. Data are presented as mean tumor weight ± SEM (n = 6). Statistical significance of saline treated versus combination treated mice is indicated by * ($p < 0.05$) and ** ($p < 0.01$).

Long-term survival study

Tumor survival was monitored to evaluate the long-term efficacy of the proposed therapy. As seen in figure 13a, mice treated with the enzyme prodrug system in combination with anti-CD73 and anti-OX40 had a significant increase in survival compared to the control, saline treated mice. The median survival went from 45 – 47.5 days for saline and control treated mice to 57 days for mCTH-ANXA5/SeMet with both immunostimulants treated mice (Table 2). H&E analysis of the liver, lungs, kidney, and heart showed no noticeable change in tissue morphology between healthy non-tumor bearing mice and saline or combination treated mice (figure 13b).

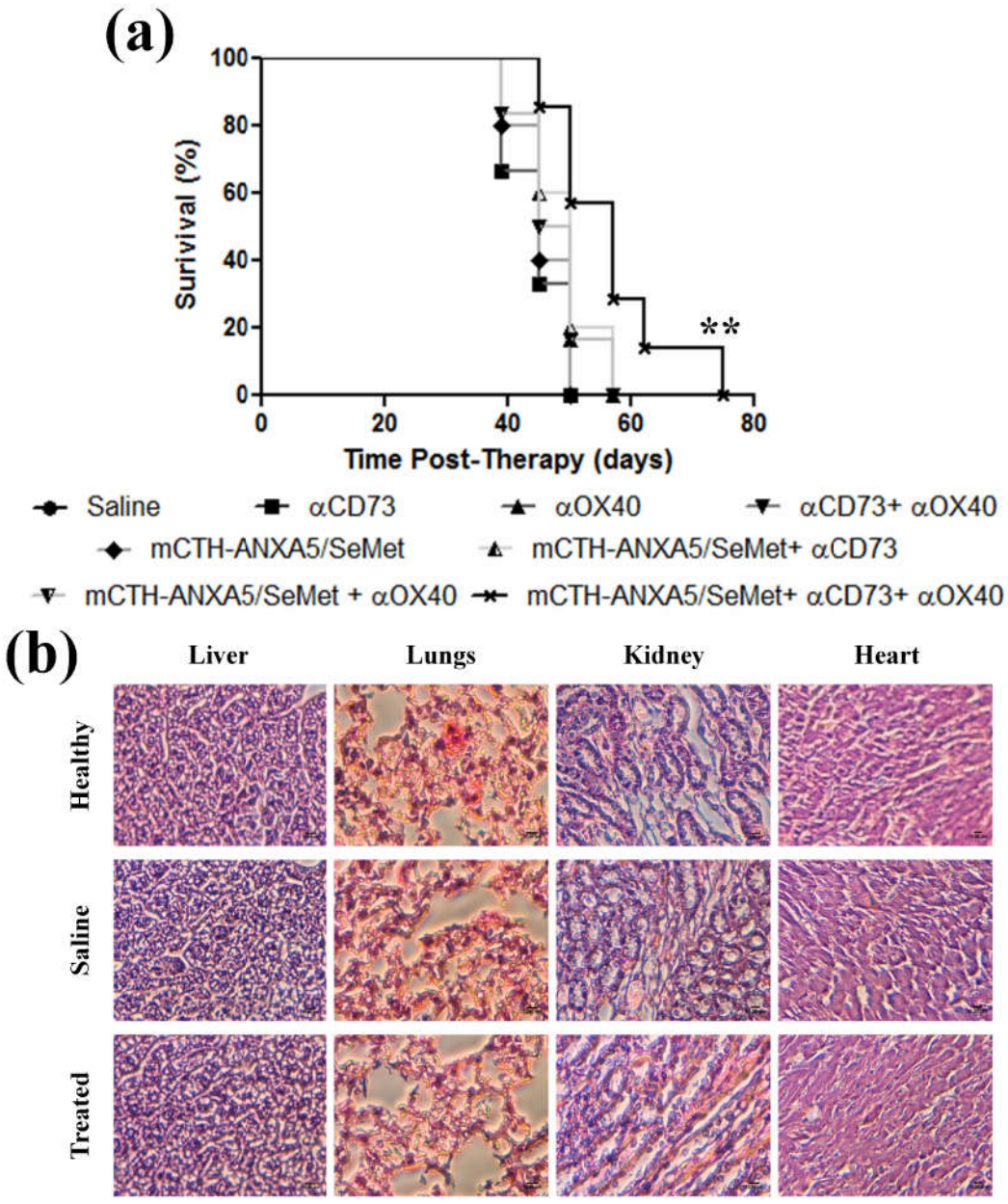

Figure 13. Survival and toxicity of enzyme prodrug synergistic therapy. Treatment on C57BL/6J mice started 10 days after inoculation with 5 x 10^6 ID8 $p53^{-/-}$ cancer cells. (a) Mice (n = 6 – 7) were treated with mCTH-ANXA5 and SeMet daily. Immunostimulats, anti-CD73 (αCD73) and anti-OX40 (αOX40), were administrated on days 10, 14, and 18 post-tumor inoculation. Survival was monitored and mice were euthanized if there was more than 10% abdominal swelling or mice seemed distressed. Statistical significance of saline treatment versus combination treatment is indicated by ** ($p < 0.01$). (b) H&E staining was conducted on the liver, lungs, kidney, and heart of non-tumor bearing (healthy), saline treated, and full combination treated mice. No visible signs of damage to the any organ were detected. Scale = 10 μm.

Group	Median Survival (days post-therapy)	p-values vs. Saline	p-values vs. mCTH-ANXA5/SeMet + αCD73 + αOX40
Saline	45		** 0.006
αCD73	45	1.000	** 0.006
αOX40	45	0.494	* 0.040
αCD73 + αOX40	47.5	0.199	0.066
mCTH-ANXA5/SeMet	45	0.719	* 0.011
mCTH-ANXA5/SeMet + αCD73	45	0.154	0.087
mCTH-ANXA5/SeMet + αOX40	47.5	0.199	0.066
mCTH-ANXA5/SeMet + αCD73 + αOX40	57	** 0.006	

Table 2. Median survival statistics.
Kaplan-Meier survival curves for all groups of mice (n = 6 – 7) with ID8 $p53^{-/-}$ tumors were analyzed for significance against saline and the full combination treated mice. Log-rank determined p-values are presented and significance is indicated * ($p < 0.05$) and ** ($p < 0.01$).

Further evaluation of cell- and antibody-mediated immunity was compared via flow cytometry of the mesenteric lymph nodes and antibody titers towards ID8 $p53^{-/-}$ cancer cells, respectively. The addition of anti-CD73 as well as the enzyme prodrug system caused an increase in CD8+ cytotoxic T-cells in the lymph nodes of mice inoculated with metastatic ovarian cancer (figure 14b). There was a significant decrease in regulatory T-cells in mice treated with anti-OX40 compared to untreated, saline mice (figure 14c), as well as with anti-OX40 or anti-OX40 and anti-CD73 combined with the enzyme prodrug system mice. The addition of immunostimulation with the enzyme produg system caused an overall increase the ratio of cytotoxic T-cells to suppressive MDSCs (figure 14d) and regulatory T-cells (figure 14e). Combining anti-CD73 with

anti-OX40 also caused an increase in tumor infiltrating macrophages as seen in figure 14f.

In addition to a cell-mediated immune response, a stronger antibody-mediated immune response is detected against ID8 p53 $^{-/-}$ ovarian cancer cells as seen in figure 14g. There is no difference in antibody presence within the plasma of healthy mice without tumors and saline treated ovarian cancer mice; however with the addition of anti-CD73 or anti-OX40 with and without the enzyme prodrug system, a slight increase in antibody presence specifically to ovarian cancer cells is detected. The greatest increase in antibodies is seen with the combination of anti-CD73 with anti-OX40 with and without the enzyme prodrug system.

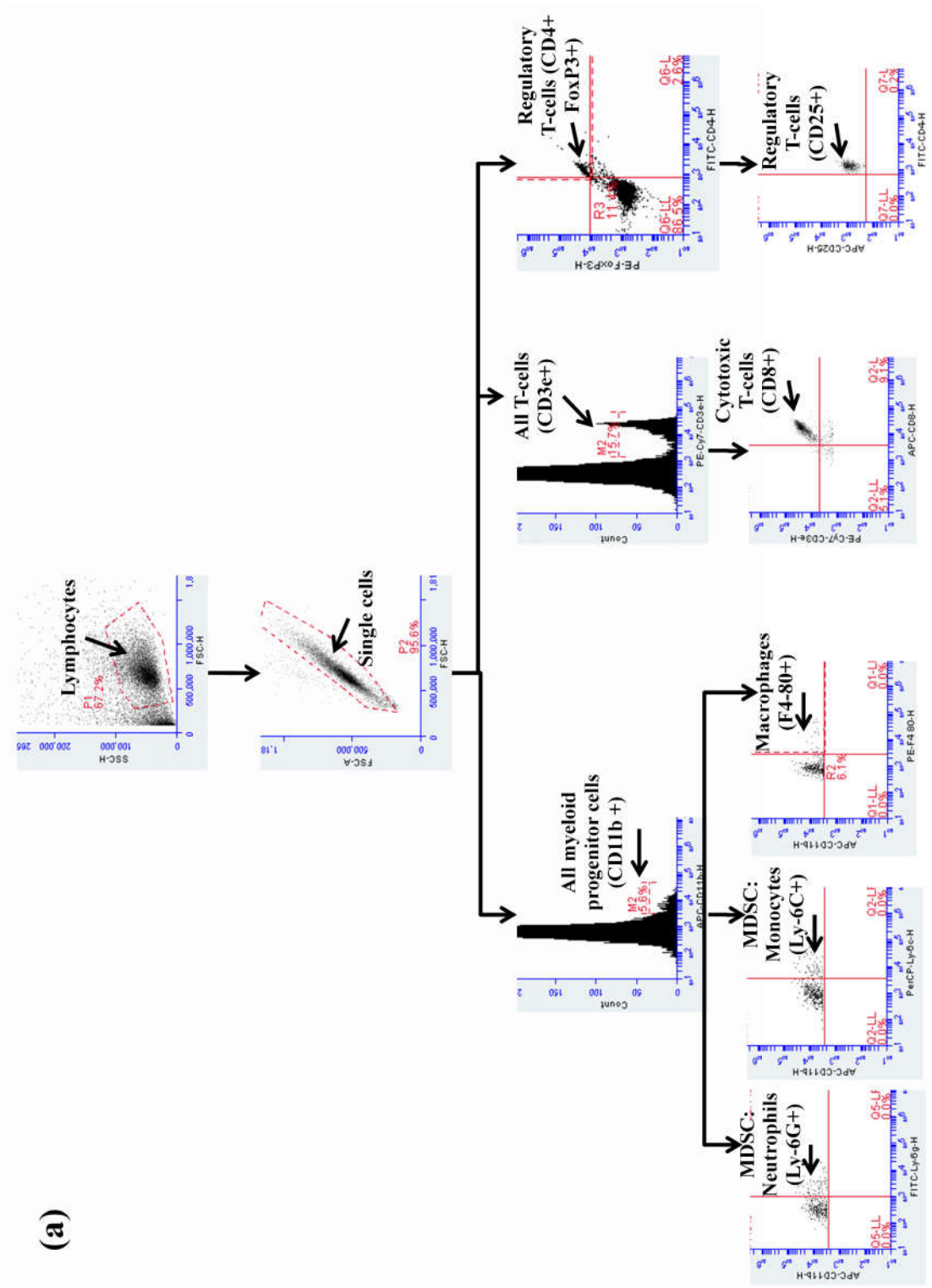
(a)
Lymphocytes
Single cells
All myeloid progenitor cells (CD11b +)
Macrophages (F4-80+)
MDSC: Monocytes (Ly-6C+)
MDSC: Neutrophils (Ly-6G+)
All T-cells (CD3e+)
Cytotoxic T-cells (CD8+)
Regulatory T-cells (CD4+ FoxP3+)
Regulatory T-cells (CD25+)

Cell-mediated Immunity
(b)
% CD8 T-cells
40
30
20
10
0
(c)
% Regulatory T-cells
40
30
20
10
0
*
(d)
Ratio of CD8 T-cells/MDSC
2.5
2.0
1.5
1.0
0.5
0.0
*
(e)
Ratio of CD8/Regulatory T-cells
1.5
1.0
0.5
0.0
Healthy
Saline
αCD73
αOX-40
αCD73+ αOX-40
mCTH-AnxA5/SeMet
mCTH-AnxA5/SeMet+ αCD73
mCTH-AnxA5/SeMet + αOX40
mCTH-AnxA5/SeMet+ αCD73+ αOX40

(f)

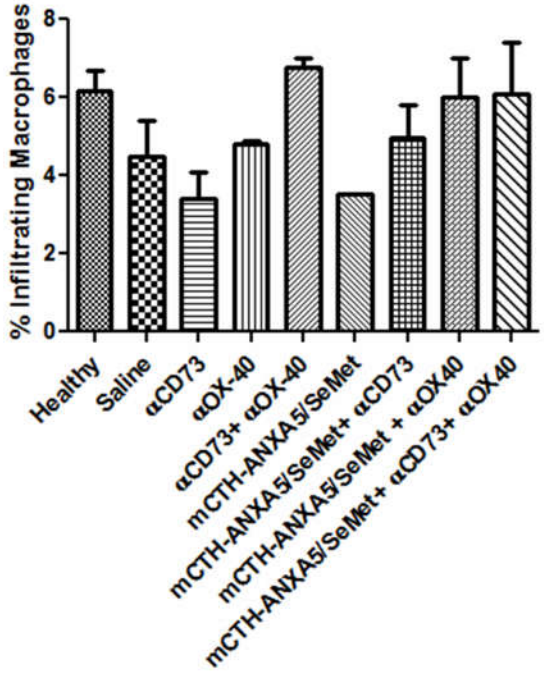

Antibody-mediated Immunity

(g)

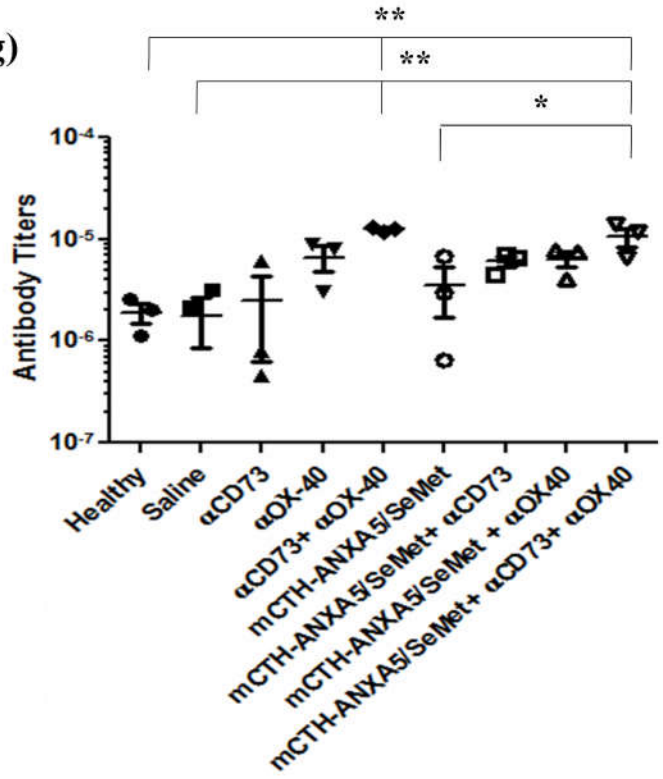

Figure 14. Cell- and antibody-mediated immune response generated due to the addition of immunostimulants.
(a) Flow cytometry schematic for identification of myeloid-derived suppressor cells (MDSCs) that are neutrophils (CD11b+ Ly-6G+) or monocytes (CD11b+ Ly-6C+), macrophages (CD11b+ F4-80+), cytotoxic T-cells (CD8+ CD3e+), and regulatory T-cells (CD25+ CD4+ FoxP3+) in the mesenteric lymph nodes of C57BL/6J mice with orthotopic metastatic ovarian tumors (ID8 $p53^{-/-}$). The mesenteric lymph nodes were collected 21 days post-inoculation of tumor cells for flow cytometry analysis. (b) Percent of single lymphocytes that are cytotoxic T-cells (CD3e+ CD8+). (c) Percent of single lymphocytes that are regulatory T-cells (CD4+, FoxP3+, and CD25+). (d) Total MDSCs were identified as sum of single lymphocytes that were either neutrophilic (CD11b+ Ly-6G+) or monolytic (CD11b+ Ly-6C+). The percent of total MDSCs was compared against the percent of cytotoxic T-cells as previously identified. (e) The percent of total regulatory T-cells was compared against the percent of cytotoxic T-cells. (f) Percent of single lymphocytes that are macrophages (CD11b+ F4-80+). (g) Antibody titers against ID8 $p53^{-/-}$ cells in the plasma of mice 3 days after immunostimulatants were given (day 21 post-inoculation). Data is presented as mean ± SEM (n = 3). Statistical significance of saline treatment versus combination treatment is indicated by * ($p < 0.05$) and ** ($p < 0.01$).

Discussion

Ovarian cancer is usually detected once metastasis to the peritoneal cavity has occurred. Current standard of care involves a cytoreductive surgery in combination with platinum-based chemotherapy, which has only a 5-month increase in survival due to development of resistance. A novel approach for metastatic ovarian cancer that can treat multiple nodules throughout the peritoneal cavity with minimum damage to healthy tissue has been developed combining an enzyme prodrug system with immunostimulation.

Human bodies work to generate and eliminate ROS in a homeostatic environment; however, tipping the scale towards a higher ratio of generation versus elimination of ROS can lead to cell death [102, 103]. In this therapy, the enzyme prodrug system works to generate a higher output of ROS in the local tumor environment thereby tipping the scale to a ROS-rich location that promotes tumor cell death. The mutant enzyme also has activity towards methionine, which is a key component in some human ovarian cancers that are methionine-dependent, as well as a key reactant for the generation of glutathionine, which reduces ROS to maintain the homeostatic balance [102, 103].

In vitro studies were initially conducted as a proof of concept for the efficacy of the treatment in ovarian cancer cells showing strong binding of the fusion protein as well as cytotoxicity with the addition of the prodrug, selenomethionine. A previous study evaluated the cytotoxic nature of the enzyme prodrug on tumor vasculature representing endothelial cells as well, since PS is expressed on tumor cells and leaky tumor vasculature [25, 116].

A dosage study was conducted to evaluate the frequency of the enzyme prodrug therapy which would provide a decrease in tumor volume while still maintaining minimum healthy tissue damage. Treatment every day over a 3 week period yielded the largest decrease in tumor volume compared to the saline, untreated mice. Injections of mCTH-ANXA5 and SeMet were given 10 h apart to allow for mCTH-ANXA5 blood clearance as determined in a previous study [25]. mCTH is a mutant of a mammalian enzyme that has minimum activity toward SeMet; however three point mutations confers reactivity to SeMet as well as methionine. Some forms of human ovarian cancer are considered methionine-dependent tumors, which may prove to be advantageous in the clinic as a dual targeting agent to produce cell death initiating ROS as well as causing methionine deprivation [102, 103]. Methionine is a key amino acid in the protein synthesis as well as *de novo* pathway, which generates glutathionine to reduce ROS and prevent cell damage [102, 103]. The combination of producing ROS as well as preventing ROS reduction may have a compounding effect in patients with ovarian tumors.

In order to transition the local tumor environment from an immunosuppressive to an immune reactive environment, combinations of anti-PD-1, anti-CD73, and anti-OX40 immunostimulants were studied to determine the most synergistic immune modulation with the enzyme prodrug system. Upregulation of PD-1 and CD73 expression have been associated with higher grade ovarian cancer and poor patient progression, which makes them key targets for immunotherapy [104, 110]. Clinical trials are under way for anti-PD-1 blockade to enhance effector T-cell infiltration and inhibit suppressive immune cells for ovarian cancer patients with promising results

[105, 117]. Combinatorial studies with anti-PD-1 and anti-OX40 in an ID8 mouse model showed promising results of increased survival, decreased tumor burden, and an increased immune response compared to either anti-PD-1 or anti-OX40 alone [107]. No change in effector or regulatory immune cells were seen with either anti-PD-1 or anti-OX40 alone; however when combined, there was an increase in the ratio of peritoneal infiltrating effector (CD4+ and CD8+ T-cells) versus regulatory (MDSCs and CD4+/FoxP3+ T-cells) immune cells [107]. Anti-CD73 is currently undergoing phase I clinical trials as well [118]. A study on 4T1 breast tumor models combining anti-PD-1 with anti-CD73 also had positive outcomes of increased survival and decreased tumor burden due to the shift in the ratio of tumor infiltrating cytotoxic T-cells to regulatory T-cells [108]. The goal of studying combinations of anti-CD73, anti-OX40, and anti-PD-1 with the novel enzyme prodrug system was to determine the most effective combination with the least distress to animals as well as a minimum toxicity to healthy tissue. Combinations of anti-PD-1 with anti-OX40 and anti-CD73 with anti-OX40 along with the enzyme prodrug system yielded the greatest decrease in tumor volume 2 weeks post-therapy; however comparing animal distress, mice treated with combinations of anti-CD73 and anti-OX40 with the enzyme prodrug system showed least animal distress.

A complete survival and immune response study was conducted comparing control, untreated mice against combination therapy mice. The only statistically significant increase in survival is seen in mice treated with a combination of the enzyme prodrug system with anti-CD73 and anti-OX40. Median survival increased to 57 days when compared to the saline treated mice (45 days). No toxicity of the full combination

therapy was identified as indicated in the H&E stains of healthy, saline, and full combination treated mice.

In order to determine the mechanism of action of the immunostimulants, immune cells from the lymph nodes as well as mouse blood were analyzed to determine the impact of a cell-mediated versus an antibody-mediated immune response. Similar to previous studies, there was an increasing trend in the presence of cytotoxic T-cells while a decrease in regulatory T-cells in mice treated with immunostimulants, either with or without the enzyme prodrug system. There is an overall positive shift in the ratio of effector to regulatory T-cells, which helps shift the tumor microenvironment towards tumor suppression. This shift can be attributed to the co-stimulatory nature of the anti-OX40, which helps activate cytotoxic T-cells that recognize foreign antigens presented by dendritic cells in the lymph nodes, as well as the blockade of adenosine production by anti-CD73. Adenosine acts on adenosine receptors to decrease activation of tumor suppressive immune cells while increasing activation of tumor promoting immune cells. In mice treated with the enzyme prodrug system along with anti-CD73 there is an overall increase in the ratio of cytotoxic T-cells to MDSCs, which act as tumor promoting cells. There is an overall increase in tumor infiltrating macrophages when combining anti-CD73 and anti-OX40. Macrophages can be either M1, anti-tumor, or M2, pro-tumor, polarized. Further evaluation will need to be conducted to evaluate the difference; however the decrease in tumor burden with the addition of the immunostimulants suggests a more anti-tumor environment. An overall decrease in tumor suppressive immune cell recruitment is observed in mice treated with either the enzyme prodrug system alone or in combination with immunostimulation, which

suggests the role of a cell-mediated immune response leading to an increase in survival and overall decrease in ovarian tumor burden.

Although some cell-mediated immunity is observed in mice treated with immunostimulants, a more significant synergism is in the antibody-mediated immune response. Previous studies combining immunostimulation with various drugs have focused on a cell-mediated immune response, but our study has proven a significant positive synergism of an antibody-mediated immune response with an ROS generating therapy. The addition of anti-CD73 or anti-OX40 caused a slight increase in antibodies generated towards the tumor cells compared to either the saline or enzyme prodrug only treated mice; however a significant increase in antibodies towards ID8 $p53^{-/-}$ cells is seen with the combination of the immunostimulants with the enzyme prodrug system. Although a strong antibody response is also seen without the addition of the enzyme prodrug system, this response was not enough to cause a significant increase in survival or decrease in tumor burden. The combination of the antibody response generated by the two immunostimulants and the addition of the ROS inducing tumor cell death is needed to cause a significant increase in animal survival.

Conclusions

This study has shown success in the treatment of metastatic ovarian cancer with a combinational approach involving an ROS generating enzyme prodrug system and immunostimulation. This therapy can be used to initially treat patients with metastatic ovarian tumors as an alternative to surgery and chemotherapy with minimal toxicity to healthy tissue as seen in the H&E, or as an option for platinum-resistive patients. The combination of the enzyme prodrug system with anti-CD73 and anti-OX40 yielded a significant increase in survival (45 – 47.5 days for saline and control mice versus 57 days for full combination mice), decrease in tumor burden, and increase in an immune response against the tumor. In future work, other combinations of immunostimulants can be evaluated to determine a more synergistic approach to treat metastatic ovarian tumors. Further work can also be conducted into the addition of pyridoxal phosphate, a co-factor for the mCTH, with the enzyme prodrug system to increase efficacy of ROS generation. Work can also be conducted into evaluating the activity a further mutated form of CTH [119, 120].

Chapter V: Mutation of Cystathionine gamma-lyase for Improved Activity and Therapeutic Efficacy

Abstract

A novel fusion protein, mCGL-ANXA5, has been developed with improved methionase activity for the reactive oxygen species (ROS) induced cell death of cancer. The fusion protein is a combination of annexin V (ANXA5), which specifically binds to phosphatidylserine (PS), and an eight point-mutated mammalian cystathionine gamma-lyase enzyme (mCGL). The point mutations provide the fusion protein with a three-fold increase in methionase activity compared to the original mutant enzyme (mCTH-ANXA5). The increase in activity is proven beneficial in a proof-of-concept *in vitro* cytotoxicity study with murine breast cancer (4T1) cells causing significant cell death after one day of treatment.

Introduction

A high proportion of tumors are identified once they have become vascularized and metastatic. The current standard of care involves a combination of chemotherapy, radiation therapy, and surgery, all of which have associated significant side effects and nonspecific toxicities. In order to provide a novel alternative, a new mutant form of cystathionine gamma lyase (mCGL) fused with annexin V (ANXA5) has been developed for the treatment of vascularized solid tumors. ANXA5 binds specifically to the phosphatidylserine (PS) exposed on the tumor vasculature and tumor cells [7, 25, 26, 37]. The fusion protein in combination with the prodrug selenomethionine (SeMet) synthesizes methylselenol, a cytotoxic drug, locally at the tumor, thus minimizing side effects associated with nonspecific accumulation of current chemotherapeutics [25].

This study focuses on the development of a new mutant, mCGL-ANXA5, which has more activity than mCTH-ANXA5 previously developed in our lab [25]. The increase in activity provides an opportunity to either lower overall dose of the enzyme prodrug system or give patients fewer cycles of therapy with the same or better therapeutic efficacy, making the novel system more clinically relevant. Characterization studies with the new mutant, mCGL-ANXA5, confirm a three-fold increase in overall activity compared to mCTH-ANXA5. The increase in activity is further seen *in vitro* on murine breast cancer (4T1) cells with a sharp increase in cytotoxicity compared to the mCTH-ANXA5.

Materials and Methods

Materials

pET-30 Ek/LIC vector was from EMD Chemicals (Billerica, MA). Gibson assembly master mix was from New England Biolabs (Ipswich, MA). Bovine serum albumin (BSA), Alamar Blue reagent, Triton X-100, EDTA, selenomethionine, isopropyl β-D-thiogalactopyranoside (IPTG), and Tris-acetate-EDTA buffer were from Sigma-Aldrich (St Louis, MO). HRV-3C protease was from Thermo Fisher Scientific (Waltham, MA). Sodium phosphate and sodium dodecyl sulfate (SDS) were from Mallinckrodt Chemicals (Phillipsburg, NJ). The 2 and 100 kDa dialysis membranes were from Spectrum Laboratories (Rancho Dominguez, CA). Murine breast cancer cells (4T1) and RPMI-1640 were from ATCC (Manassas, VA). Fetal bovine serum (FBS) was from Atlanta Biologicals (Lawrenceville, GA). Antibiotics, penicillin and streptomycin, were from Invitrogen (Grand Island, NY).

Fusion protein construction, expression, and purification

Eight point mutations were made to wild type human cystathionine gamma-lyase (CTH) previously [120]. The same mutations were made to mouse CTH (E58I, S62L, L90M, R118L, K267R, P3110G, E338V, and I352S). Mutant mouse CTH (mCGL) and annexin A5 (ANXA5) gene fragments were codon optimized for *E. coli* protein production and synthesized (Life Technologies) as three gene fragments (sequences can be found in Appendix B: mCGL-ANXA5 Gene Construction). The gene fragments were assembled into the pET-30Ek/LIC vector using the Gibson Assembly method [121]. Gibson assembly and cell transformation were conducted as previously described

(more details can be found in Appendix C: Laboratory Protocols) [25]. Colonies were analyzed via DNA electrophoresis as seen in Figure 15. Colonies with the correct DNA size were sent for sequencing (Oklahoma Medical Research Foundation, Oklahoma City, Oklahoma). Protein production and purification were conducted using the same parameters as mCTH-ANXA5 production as previously described [25].

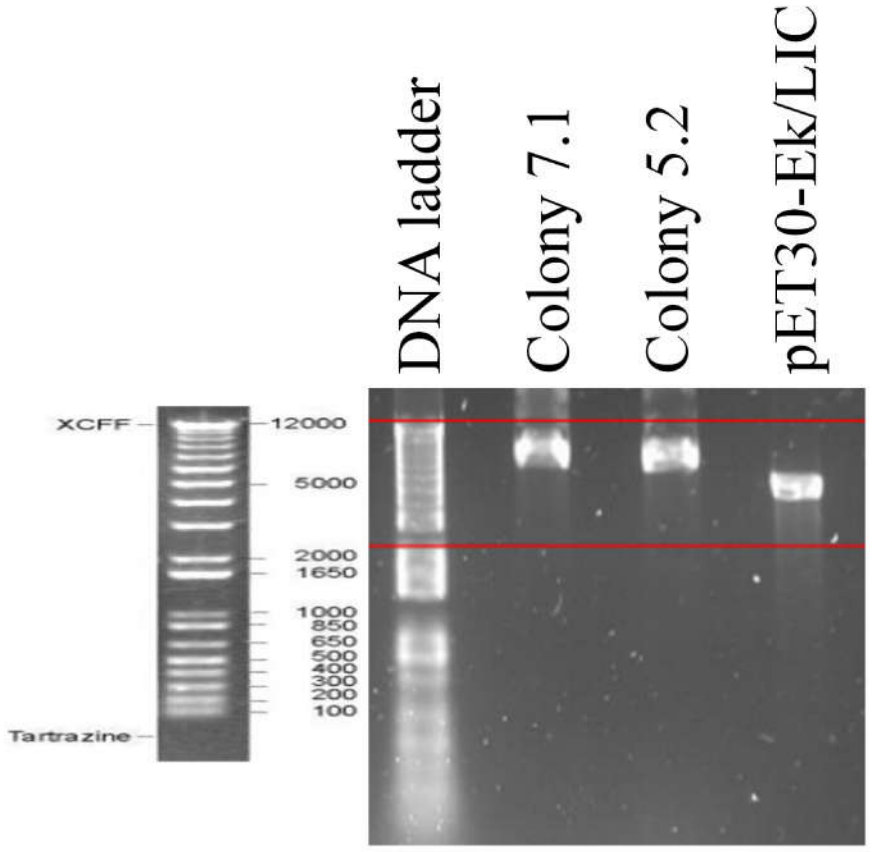

Figure 15. DNA gel electrophoresis of mCGL-ANXA5 E. coli colonies.
The vector is 5439 bp and the addition of the mCGL-ANXA5 gene to the vector increased size to 7647 bp for colonies 7.1 and 5.2, as determined by DNA sequencing. The size determined is the same as the theoretical size with the mCGL-ANXA5 gene insertion.

Fusion protein specificity constant assay

Enzyme activity with L-selenomethionine was assessed according to the methioninase assay previously described [116] with varying concentrations of prodrug.

Cell line and culture conditions

4T1 cells were grown in RPMI-1640 medium enriched with 10% FBS and penicillin/streptomycin antibiotics (100 U ml^{-1} and 100 μg ml^{-1}, respectively). The cells were grown at 37°C with 5% CO_2.

Binding strength

The dissociation constant for mCGL-ANXA5 was determined as previously described [25] using biotin conjugated mCGL-ANXA5 on 70% confluent 4T1 cells. Specific binding was determined by subtracting total binding (medium supplemented with calcium) from nonspecific binding (medium supplemented with EDTA).

In vitro cytotoxicity studies

Alamar Blue cell viability assays were conducted to determine the cytotoxic effects of mCGL-ANXA5 combined with SeMet on 4T1 cells over 3 days in 24-well plates as previously described [25].

Statistical Analysis

Statistical significance of *in vitro* cell survival was assessed using a one-way ANOVA and Tukey-Kramer multiple comparisons test with GraphPad Prism software.

Results

Mutant fusion protein characterization

The new mutant fusion protein, mCGL-ANXA5, was characterized against the original mutant, mCTH-ANXA5. The fusion protein, mCGL-ANXA5, had yields of 40 mg l^{-1} of culture medium with > 95% purity. The specificity constant, which is a measure of how efficiently substrates are converted into a product by an enzyme, for selenomethionine was 1698.03 and 567.96 M^{-1} s^{-1} for mCGL-ANXA5 and mCTH-ANXA5, respectively (data can be found in Figure 28 of Appendix A: Supplemental Data). The dissociation constant (k_d) for mCGL-ANXA5 was 0.53 ± 0.16 mM for 4T1 murine breast cancer cells (data can be found in Figure 29 of Appendix A: Supplemental Data), which is similar to the dissociation constant of mCTH-ANXA5 (0.71 ± 0.48 mM) as previously determined [25].

In vitro cytotoxicity

The cytotoxic efficacy of the new mutant fusion protein, mCGL-ANXA5, was evaluated on 4T1 breast cancer cells as seen in Figure 16. Significant cell death is seen after one day of mCGL-ANXA5 and one day of 100 μM SeMet, with increasing cytotoxicity as concentrations of SeMet or treatment days increased.

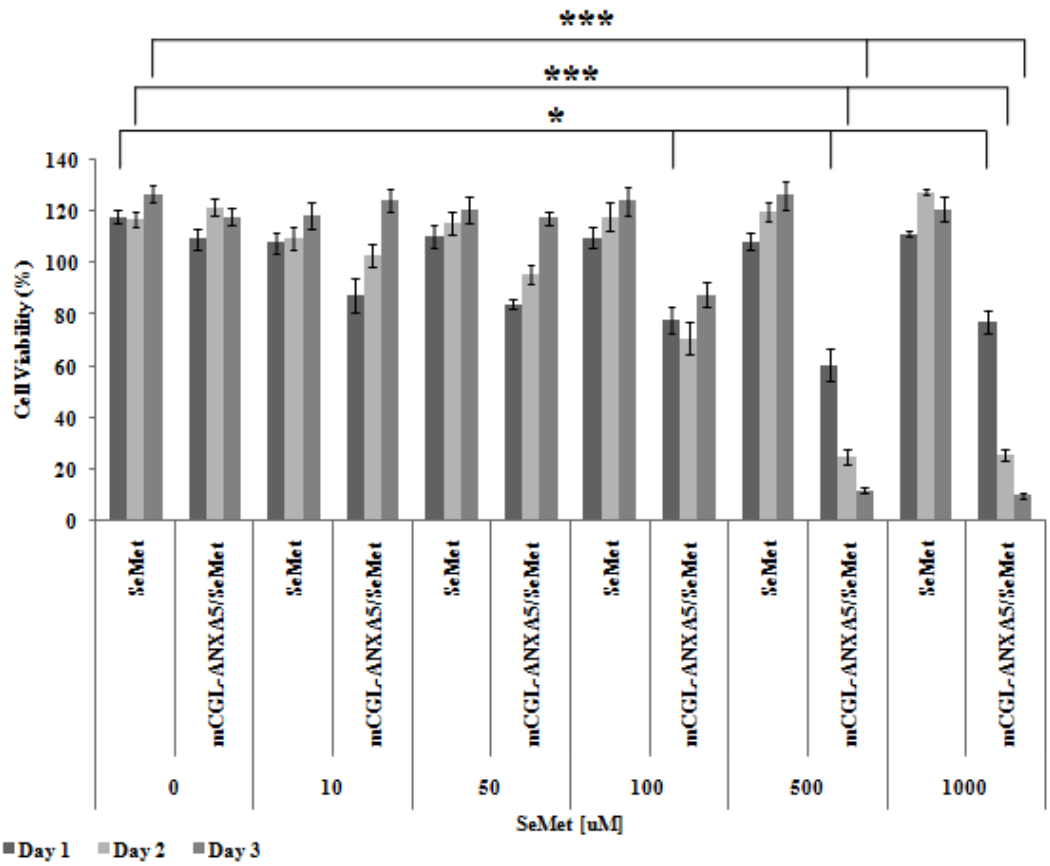

Figure 16. In vitro cytotoxicity of the new enzyme prodrug system.
Cytotoxicity of murine (4T1) breast cancer cells to increasing concentrations of SeMet in the presence of mCGL-ANXA5 was determined. Data is presented as mean ± SE (n = 3). Statistical significance between groups is denoted by * ($p < 0.05$) and *** ($p < 0.001$) with control, untreated cells compared against enzyme prodrug treated cells.

Discussion

The addition of eight point mutations to the mammalian cystathionine gamma-lyase enzyme provides it with improved methionase activity compared to the original mutant, mCTH-ANXA5, used in the previous chapter. There was a 3-fold increase in the specificity constant, which means that the new mutant can bind as well as convert selenomethionine into methylselenol more efficiently. The binding strength of mCGL-ANXA5 was slightly stronger than mCTH-ANXA5, which provides an added advantage of stronger association *in vivo*.

In a previous study, the original mutant, mCTH-ANXA5, was evaluated with 4T1 cells and significant cell death was seen after three days of enzyme prodrug therapy [25]. Comparatively, the new mutant caused significant cell death after only one day of treatment at the same concentration of fusion protein and SeMet. The overall increase in activity renders the new mutant more active *in vitro*, and may provide a boost in the current therapy *in vivo* by either decreasing the frequency of the therapy needed or decreasing the concentration of the enzyme prodrug system needed, making it more clinically applicable.

Conclusions

This study has shown successful synthesis of a novel, mutant fusion protein, mCGL-ANXA5. The new mutant has eight mutations compared to the original cystathionine gamma-lyase enzyme, which makes it three times more active than the previous mutant. The increase in activity is advantageous in causing significant breast cancer cell death with only one day of enzyme prodrug therapy compared to three days with the other mutant. Further evaluation of *in vivo* cytotoxicity and biocompatibility needs to be conducted compared to the previous mutant.

Chapter VI: Enhanced MicroCT Imaging via Phosphatidylserine Targeted Gold Nanoparticles

Abstract

Breast cancer has one of the highest mortality rates usually due to metastatic development before primary tumor detection. Mammograms are the current standard of diagnosis with annual checkups recommended for women 40 – 54 years of age; however due to the low sensitivity and high rate of misdiagnosis patients either are not identified during the early stages or they are overdiagnosed and overtreated, sometimes leading to radiation-induced tumor development. One of key disadvantages of mammograms is their failed ability to differentiate between a dense breast and a tumor usually leading to more mammograms and more expensive diagnostic tools such as surgery, magnetic resonance imaging (MRI), or positron emission tomography (PET). In order to provide a widely available imaging tool for breast cancer, a novel, targeted gold nanoparticle (AuNP) has been developed. AuNPs are high density particles that increase X-ray attenuation during computed tomography (CT) and can be used for *in vivo* identification of breast cancer. Annexin V (ANXA5) conjugated gold nanoparticles (AuNP-ANXA5s) have been developed to specifically bind to phosphatidylserine (PS) expressing tumor cells and tumor vasculature. *In vitro* and *in vivo* studies showed a significant increase in contrast when comparing targeted and untargeted nanoparticles. Tumors as small as 4 mm were detectable as early as 4 h post-injection and remained detectable for 96 h, providing evidence of a promising, sensitive tool for early breast cancer diagnosis.

Introduction

Breast cancer is the most common form of cancer for US women with the second highest rating for death from cancer. It is estimated that 252, 710 new cases of breast cancer will be diagnosed in the US alone in 2017 with 40, 610 deaths [122]. Cancer is often detected either during late, untreatable stages or as clinically insignificant tumors due to the lack of a highly specific and sensitive detection methodology that can be commonly available to the masses for monitoring progression. These rates can be significantly reduced if tumors are caught earlier during the pre-malignant. Currently, survival rates for patients receiving aggressive treatment before tumor metastasis have a 94% survival rate. Survival rates fall precipitously to below 10% in late stage, invasive tumors [14].

The current form of breast cancer detection is annual screening of women 40 – 54 years via mammograms followed by biopsies and in some instances magnetic resonance imaging (MRI). These multiple tests exponentially increase the costs of diagnosis for patients. In addition to the monetary costs associated with excessive testing, there are significant quality of life costs to repeated screenings. A 10-year cumulative study reported overdiagnosis rates as high as 65%. Overdiagnosis results in painful invasive screenings and treatments. Up to 77% of women reported pain during mammograms, and of these women, 11 – 46% declined further screening. Additionally, the high doses of radiation from repeated screenings can increase the risk of developing radiation-induced cancer [123]. Currently mammograms are the gold standard of diagnosis for women at risk for breast cancer; however they fail to test for differences in breast density, which increases costs of diagnosis (follow-up biopsies and MRI), need

for repeated screenings, and increases the risk of overdiagnosis and overtreatment. Due to this void in accurate early detection of breast cancer, a novel and highly specific cancer targeting nanoparticle has been developed for use with computer tomography (CT). Using CT is advantageous since it is available in most clinics and hospitals around the world for easy implementation and significantly more sensitive than mammograms.

Gold nanoparticles (AuNPs) have been clinically employed as biosensors, immunological assessment tools, drug delivery agents, and in use of disease detection and treatment due to their high versatility [124-127]. *In vitro* as well as *in vivo* studies have proven the nontoxic nature of AuNPs, which are currently in clinical trials as drug delivery and photothermal agents [124-129]. We propose the use of targeted AuNPs with CT as contrast agents for early detection of breast cancer as a more accurate and sensitive alternative to mammograms alone.

AuNPs are coated with annexin V (ANXA5), which is a protein that specifically binds phosphatidylserine (PS) exposed only on tumor cells and the tumor vasculature [7]. PS is internalized in healthy tissue, thus making ANXA5 a specific target for multiple cancers including breast cancer [7, 37]. ANXA5 is naturally found in humans and mice, making it nontoxic and safe for use. The AuNPs have also been tested clinically to be nontoxic and are also coated in polyethylene glycol (PEG), which shields the particle from the immune system and prevents toxicity further [130].

CT scans, similar to mammograms, distinguish tissues based on attenuation, the amount of x-rays that pass through a tissue versus the amount that bounces off the tissue and onto the detector. Heavier tissues such as bone attenuate more x-rays onto the

detector for a higher contrast while soft tissues such as breast tissue have low attenuation, making them hard to distinguish. In order to improve the contrast of tumors from the surrounding soft tissue, higher density AuNPs, which attenuate more x-rays, are specifically targeted to the malignant region. Unlike mammograms, AuNPs in conjunction with CT scans provide higher sensitivity and specificity as well as minimize discrepancies in detection due to differences in breast densities.

Due to the high density of gold along with the specific targeting ability of ANXA5, this study hypothesizes that targeted AuNP-ANXA5s in combination with CT can be used as an alternative to identify breast tumors with higher specificity and sensitivity. This study has proven the efficacy of increasing contrast of breast cancer tissue by 2-3-fold with targeted AuNP-ANXA5s versus untargeted AuNPs *in vitro* as well as *in vivo* on orthotopic breast (4T1) tumors. AuNP-ANXA5s have a blood clearance of 8 h and a tumor residence time up to 96 h, providing a novel tool to track tumor progression and therapy efficacy over time without the need for repeated contrast agent delivery.

Materials and Methods

Materials

The plasmid encoding ANXA5, pET-30 Ek/LIC/ANXA5, was previously constructed in this lab [64]. Bovine serum albumin (BSA), Alamar Blue reagent, Triton X-100, EDTA, sulfo-SMCC, and Tris-acetate-EDTA buffer were from Sigma-Aldrich (St Louis, MO). Sodium phosphate is from Mallinckrodt Chemicals (Phillipsburg, NJ). Paraformaldehyde was from Electron Microscopy Sciences (Hatfield, PA). Antifade reagent Fluoro-gel, borate buffer, fluorescein isothiocyanate (FITC), matrigel, and Slide-A-Lyzer dialysis cassettes (3.5 kDa) were from Thermo Fisher Scientific (Waltham, MA). The 2 and 100 kDa dialysis membranes were from Spectrum Laboratories (Rancho Dominguez, CA). Anti-ANXA5 (FL-319) was from Santa Cruz Biotechnology (Santa Cruz, CA). Murine breast cancer cells (4T1) and RPMI-1640 were from ATCC (Manassas, VA). Fetal bovine serum (FBS) was from Atlanta Biologicals (Lawrenceville, GA). Antibiotics, penicillin and streptomycin, were from Invitrogen (Grand Island, NY). Gold nanoparticles (15 nm) were from Nanoprobes (Yaphank, NY). The 1,2-distearoyl-*sn*-glycero-3-phosphoethanolaminepolyethylene glycol-maleimide (NH_2-PEG-SH; PEG molecular weight of 3.4 kDa) linker was from Creative PEGWorks (Winston Salem, NC).

ANXA5 production

Recombinant ANXA5 was produced as previously described [64]. ANXA5 was characterized via SDS-PAGE.

AuNP-ANXA5 Synthesis

AuNP-ANXA5 was produced in the lab using modified protocols as described [28, 131, 132]. Briefly, AuNPs (15 nm) were initially conjugated to NH_2-PEG-SH at a ratio of 1:4 (w/w) overnight at 4°C stirring. AuNPs were washed 3X with PBS and centrifuged at 16,000 g for 20 min. Sulfo-SMCC was added in a 1:2 (w/w) ratio to the AuNP-PEG and incubated for 30 min at room temperature, stirring. The AuNP-PEG-sulfo-SMCC was washed 3X with PBS and centrifuged at 16,000 g for 20 min. ANXA5 was added in a 1:10 (w/w) ratio and incubated overnight at 4°C followed by 3X washes. The AuNP-ANXA5s were quantified via absorbance at 520nm (standard curve can be found in Figure 30 of Appendix A: Supplemental Data) as well as a Bradford assay. A schematic of the AuNP-ANXA5 conjugation is depicted in figure 17 (more details can be found in Appendix C: Laboratory Protocols).

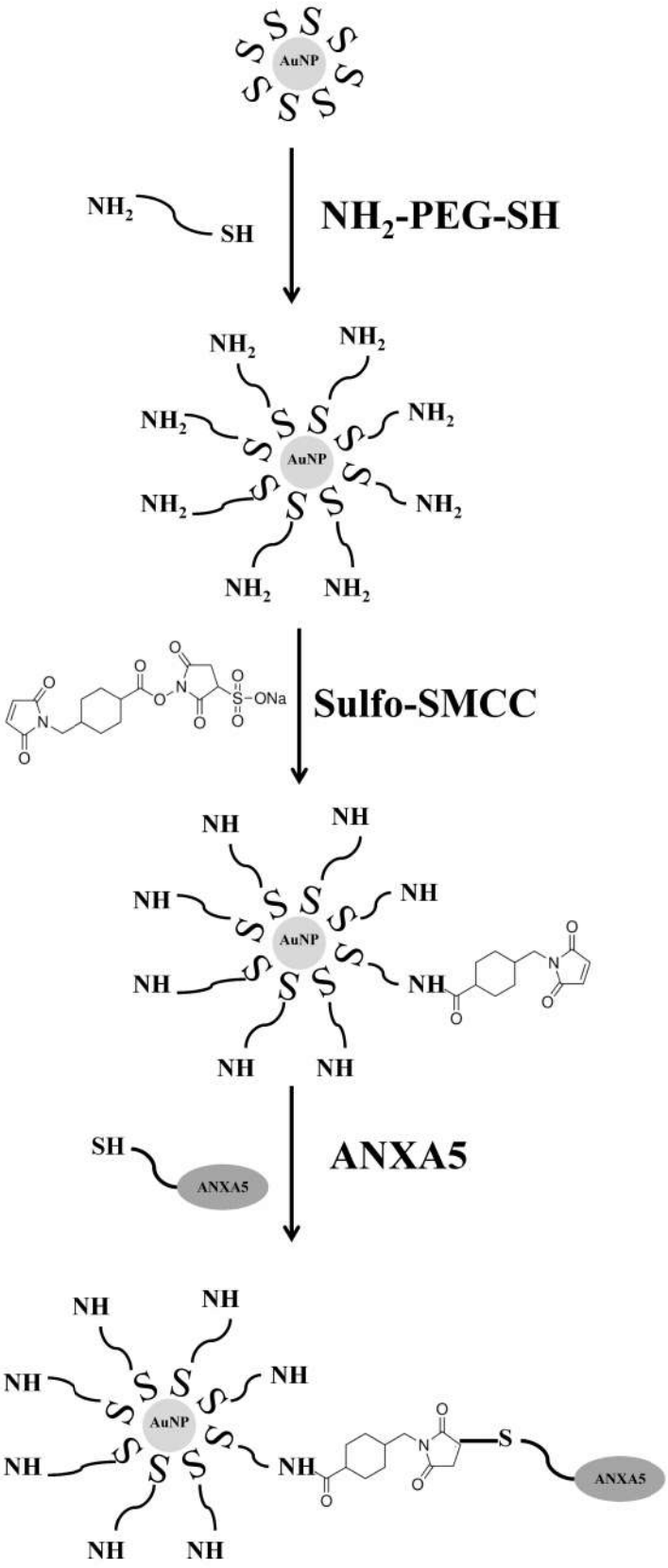
AuNP
NH2
SH
NH2-PEG-SH
NH2
NH2
NH2
NH2
NH2
NH2
NH2
NH2
AuNP
Sulfo-SMCC
NH
NH
NH
NH
NH
NH
NH
NH
NH
AuNP
SH
ANXA5
ANXA5
NH
NH
NH
NH
NH
NH
NH
NH
NH
AuNP
NH
S
ANXA5

Figure 17. Schematic depicting synthesis of tumor targeted gold nanoparticles (AuNP-ANXA5).
Initially 15 nm gold nanoparticles were coated with PEG (HS-PEG-NH_2), a biocompatible polymer. Following PEG coating, a linker (sulfo-SMCC) to conjugate ANXA5 to the nanoparticle was bound to the PEG with ANXA5 attached to the other end. Any unbound PEG, sulfo-SMCC, or ANXA5 was washed off via centrifugation for a final product of AuNP-ANXA5.

Dynamic light scattering and zeta potential

Dynamic light scattering (DLS) and zeta potential for AuNP, AuNP-PEG, and AuNP-ANXA5 nanoparticles was conducted using a Brookhaven ZetaPALS system. Samples were diluted in nanopure water for DLS and 1 M KCl solution for zeta potential.

Agarose gel

A 2% agarose gel in Tris/Borate/EDTA (TBE) buffer was made. Samples were loaded and run at 100 V for 1 h.

Transmission electron microscopy

A drop of either AuNPs or AuNP-ANXA5s was placed on a lacey carbon grid and allowed to dry. Both grids were stained with 1% uranyl acetate for 5 min and washed with nanopure water. Nanoparticles were imaged with a Zeiss 10A transmission electron microscope.

Cell lines and culture conditions

4T1 cells were transfected with tdTomato (Td). 4T1-Td cells were grown in RPMI-1640 medium enriched with 10% FBS and penicillin/streptomycin antibiotics (100 U ml^{-1} and 100 μg ml^{-1}, respectively). The cells were grown at 37°C with 5% CO_2.

In vitro binding strength

The dissociation constant for AuNP-ANXA5 was determined as previously described [64] using biotin conjugated AuNP-ANXA5 on 70% confluent 4T1-Td cells. Specific binding was determined by subtracting total binding (medium supplemented with calcium) from nonspecific binding (medium supplemented with EDTA).

In vitro fluorescence visualization

4T1-Td cells were grown to 70% confluence on cover slips. AuNP-ANXA5s were tagged with FITC following a protocol by [64]. AuNP-ANXA5-FITCs (1.5 mg ml^{-1}) in 2 mM $CaCl_2$ were incubated with 4T1-Td cells for 2 h followed with PBS washing. The cells were fixed in 4% paraformaldehyde. Images were taken on a Nikon fluorescence microscope.

In vitro microCT contrast enhancement

4T1-Td cells were grown to 70% confluence on a T-75 plate. Cells were lifted and incubated with either 1.5 mg ml^{-1} AuNP or AuNP-ANXA5s in microcentrifuge vials at 37°C for 2 h. Cells were washed 3X with media and centrifuged at 1000 g for 5 min

followed by fixation with 4% paraformaldehyde. Images were taken on a PerkinElmer Quantum GX microCT (Waltham, MA) at 50 keV.

Animal handling procedures

All procedures complied with a protocol approved by Institutional Animal Care and Use Committee (IACUC) of the University of Oklahoma Health Sciences Center. Balb/cJ female mice 6 weeks of age, weighing 18 – 20 g were used. Mice were on a standard chow diet.

In vivo tumor model

Mice were injected in mammary fat pad number four with 1 x 10^5 4T1-Td mouse breast cancer cells suspended in 50 µl PBS and 50 µl of matrigel. Mouse body weight and tumor volume were monitored every 3 to 4 days. Tumor volume was calculated with the modified ellipsoid formula volume = (1/2) x (length x width^2) using caliper measurements of the longest dimension and perpendicular width. Mice bearing orthotopic 4T1-Td were randomized into groups (6 to 7 per group) prior to the start of the study when tumors reached 100 mm^3.

In vivo blood clearance

Blood clearance was determined based on a modified protocol from [25]. Briefly, AuNP-ANXA5s were tagged with biotin following the SeraCare company protocol. Blood was collected from mice (n = 3) between 0 – 24 h and analyzed via an ELISA sandwich assay using streptavidin coated high-affinity plates. Plasma dilutions were

incubated on strepatavidin coated plates for 2 h at 37°C. Plates were washed and blocked with 1% fetal bovine serum PBS buffer three times. Following washes, wells were incubated for 1 h with 1:5000 dilution of HRP conjugated goat anti-mouse IgG and IgM. The wells were developed with *o*-phenylenediamine (OPD) for quantification on a BioTek Synergy plate reader (more details can be found in Appendix C: Laboratory Protocols).

In vivo targeted binding affinity

Mice (n = 6-7) were injected with 250 mg kg^{-1} AuNP or AuNP-ANXA5 intravenously when tumors reached 100 mm^3. Mice were imaged with Flex X-O X-PET (Gamma Medica Ideas, Northridge, CA) animal imager at 50 keV with 256 slices before the injection and for 96 h after. Gold concentration was determined by quantifying CT intensity at the tumor against the control image using the Amira software. Intensity was correlated to a gold standard curve previously generated (standard curve can be found in Figure 31 of Appendix A: Supplemental Data).

Statistics

Statistical significance of *in vitro* and *in vivo* contrast enhancement studies was assessed using a one-way ANOVA and Tukey-Kramer multiple comparisons test with GraphPad Prism software.

Results

Characterization of AuNP-ANXA5s

Multiple analysis (UV-vis spectroscopy, agarose gel, DLS, and zeta potential) were conducted on the particles confirming that the addition of ANXA5 as well as the maintenance of the key characteristics of AuNPs that makes it a contrast agent. Analysis via UV-vis spectroscopy was conducted, ensuring that the particle retained its characteristic properties as seen in the similar absorbance spectrums in figure 18a of AuNP against AuNP-ANXA5.

Table 3 further depicts the transition in size and surface modification of the particle as seen in the increasing hydrodynamic diameters (AuNP < AuNP-PEG < AuNP-ANXA5) of the particles. The surface charge of the nanoparticle also changes with the addition of PEG and ANXA5 as seen in the zeta potential in table 3. Since ANXA5 is a negatively charged protein, the surface of the nanoparticle becomes more negative with the addition of ANXA5 as compared to the particle only coated in PEG.

Another key feature to evaluate the conjugation of ANXA5 to the surface of AuNPs was assessed on an agarose gel. An agarose gel allows nanomaterials to move through a gradient based on size. Smaller particles, such as AuNP, travel further down the gel while larger particle, such as AuNP-ANXA5, travel slower. As seen in figure 18b, AuNP moved the furthest, followed by AuNP-PEG and finally AuNP-ANXA5.

A final characterization was conducted to visualize the nanoparticles coated in ANXA5 protein. Transmission electron microscopy (TEM) with staining for protein presence was conducted on AuNP and AuNP-ANXA5. Figure 18c shows individual

gold nanoparticles (dark black circles) with the ANXA5 protein (hazy, dark gray region) directly attached to the surface.

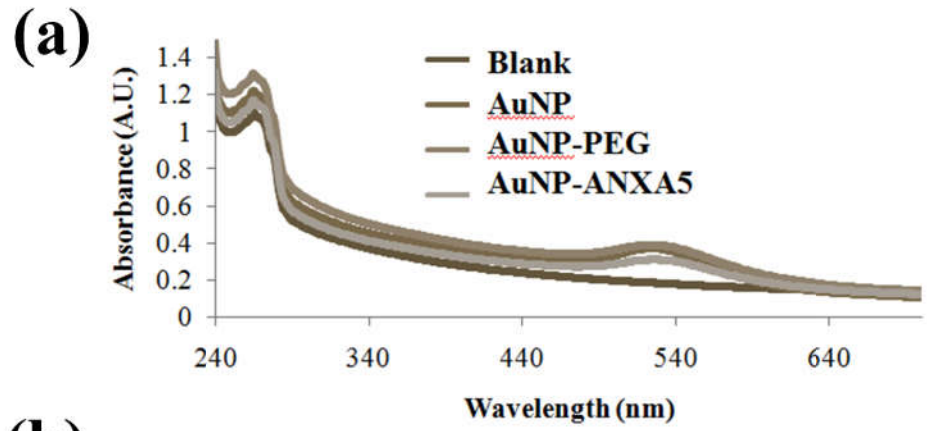

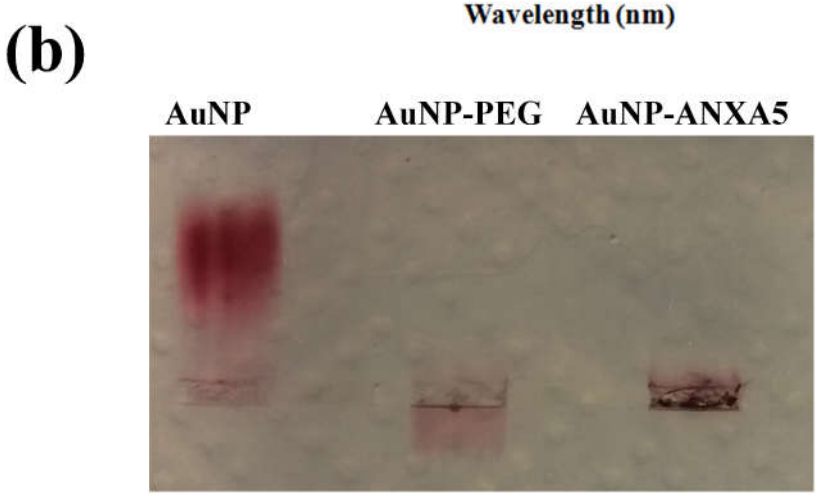

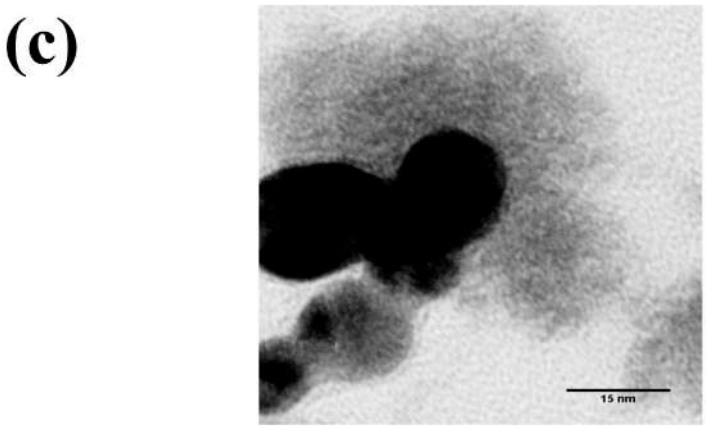

Figure 18. Characterization of AuNP-ANXA5.
(a) Absorbance spectrum of gold nanoparticles showing no change in primary characteristics, which would affect the CT enhancement property of the particle, with the addition of PEG or ANXA5. (b) An agarose gel confirming surface modification of AuNPs. Smaller particles, such as AuNP, move further and fast through the gel, while larger particles, such as AuNP-ANXA5, more slower down the gel. (c) A transmission electron microscopy image of single gold nanoparticles (dark black circle) coated with ANXA5 protein (hazy, dark gray region). Scale bar is 15 nm.

Sample	Hydrodynamic Diameter (nm)	Zeta Potential (mV)
AuNP	58.8 ± 0.6	-5.6
AuNP-PEG	80.6 ± 1.8	-0.6
AuNP-ANXA5	101.6 ± 1.0	-5.44

Table 3. DLS and zeta potential of AuNP-ANXA5.
Confirmation of the surface modification of AuNPs with PEG and ANXA5 as seen in changes of the hydrodynamic diameter of the particle increasing with each addition of PEG and ANXA5. The surface charge of the nanoparticle (zeta potential) is also altered with the addition of PEG which makes the surface more neutral to act as a shield against the immune system *in vivo*. While the addition of ANXA5, which is a negatively charged protein, makes the particle surface slightly more negative, confirming binding of ANXA5 to the surface. Data represented as mean ± SEM (n = 3).

In vitro confirmation

Binding was further tested by incubating 4T1 breast cancer cells with AuNP or AuNP-ANXA5 followed by CT via a PerkinElmer Quantum GX microCT (Waltham, MA) as seen in figure 19a. Breast cancer cells that were incubated with only AuNP had only a ~2-fold increase in contrast compared to cells with no nanoparticles. Cells incubated with AuNP-ANXA5 had a ~4-fold increase in contrast. This study provides significant

evidence of the benefit of using targeted gold nanoparticles to enhance the X-ray detection of cancer cells for early detection. The binding of the AuNP-ANXA5s specifically to 4T1 breast cancer cells was 60.31 ± 68 pM (data can be found in Figure 32 of Appendix A: Supplemental Data). This can be visualized in figure 19b with the localization of FITC labeled AuNP-ANXA5s with tdTomato red fluorescently labeled 4T1 breast cancer cells.

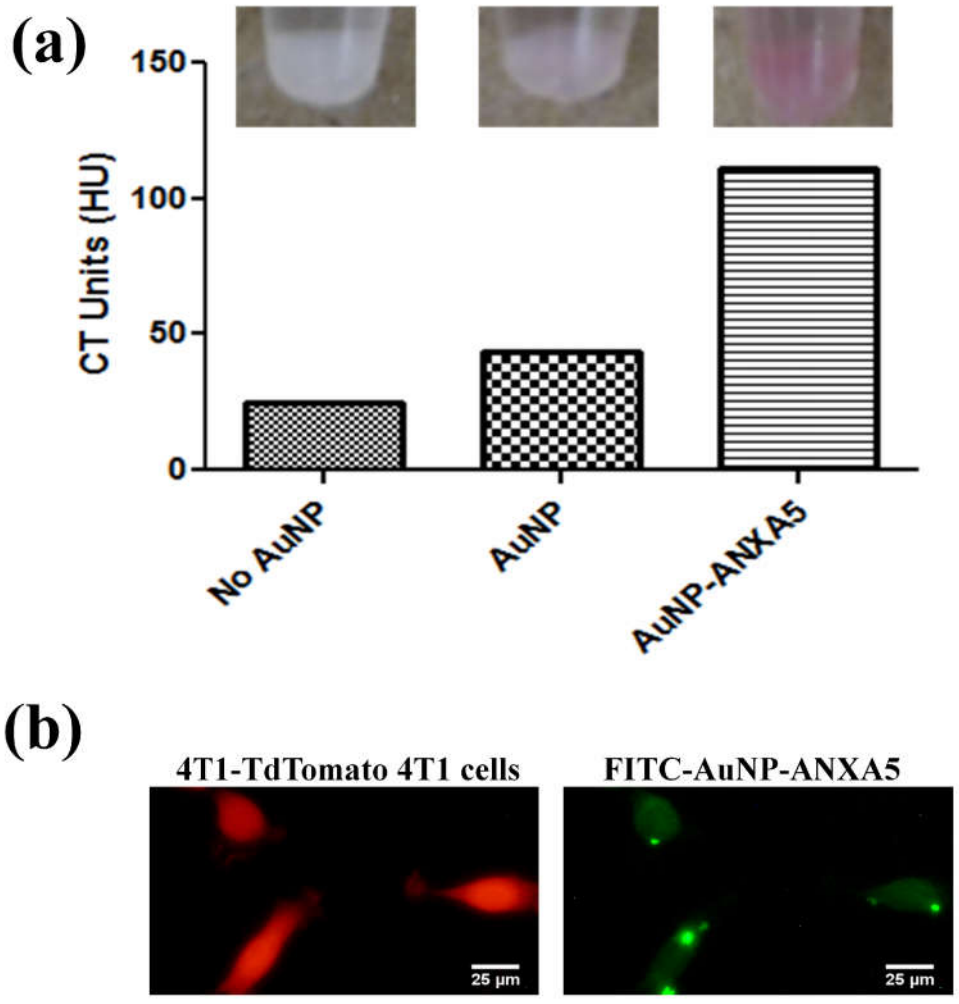

Figure 19. *In vitro* binding specificity of AuNP-ANXA5.

(a) 4T1 breast cancer cells (n = 1) were incubated with either AuNP or AuNP-ANXA5 (1.5 mg ml^{-1}) for 2 h followed by washing of any unbound nanoparticles. Cells were imaged via CT and difference in contrast was evaluated. The addition of untargeted AuNPs causes a slight increase in contrast of cells; however a significant increase in contrast is seen in cells incubated with targeted nanoparticles (AuNP-ANXA5s). The images above the graph are representative of the cells incubated with each nanoparticle. The cells incubated with AuNP-ANXA5s visibly look more pink due to the accumulation of the gold nanoparticles. (b) Fluorescent microscopy showing localization of tdTomato labeled 4T1 cancer cells (left) and FITC-labeled AuNP-ANXA5 (right). Scale bar is 25 μm.

In vivo confirmation

An animal study on mice with orthotopic 4T1 breast tumors in the mammary fat pad was conducted to determine how long the AuNP-ANXA5s remained in the blood. As seen in figure 20, within 8 hours the gold nanoparticles are cleared from the bloodstream.

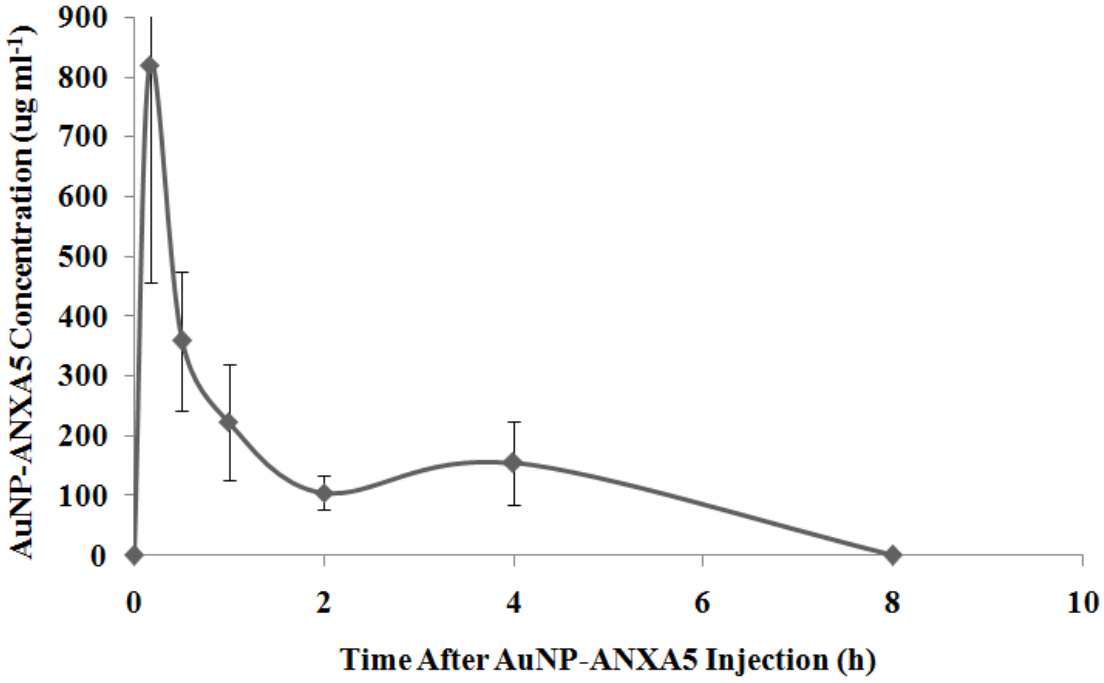

Figure 20. Blood clearance.

Balb/c mice (n = 3) were injected with biotinylated AuNP-ANXA5s, and blood was collected between 10 mins to 24 h post-injection. After 8 h, no AuNP-ANXA5s were detectable in the blood of mice.

A second animal study comparing targeted versus untargeted gold nanoparticles was conducted to evaluate the clinical relevance of using AuNP-ANXA5s for detection of breast cancer. Mice were injected intravenously (i.v.) with 250 mg kg^{-1} (5 mg) of either AuNPs or AuNP-ANXA5s, and CT scans were conducted via a Flex X-O X-PET (Gamma Medica Ideas, Northridge, CA) system over time to compare tumor accumulation of nanoparticles.

Figure 21 shows representative CT images of mice with small 4T1 breast tumors 12 h after delivery of either AuNP (figure 21a) or AuNP-ANXA5 (figure 21b). When comparing the tumors before injection of nanoparticles versus after, the mice injected with AuNP-ANXA5s have a strong, bright border around the rim of the tumor (white arrows) where the gold nanoparticles have accumulated in the tumor as well as on the tumor vasculature. On the other hand, the untargeted AuNPs injected mouse has minimum increase in contrast.

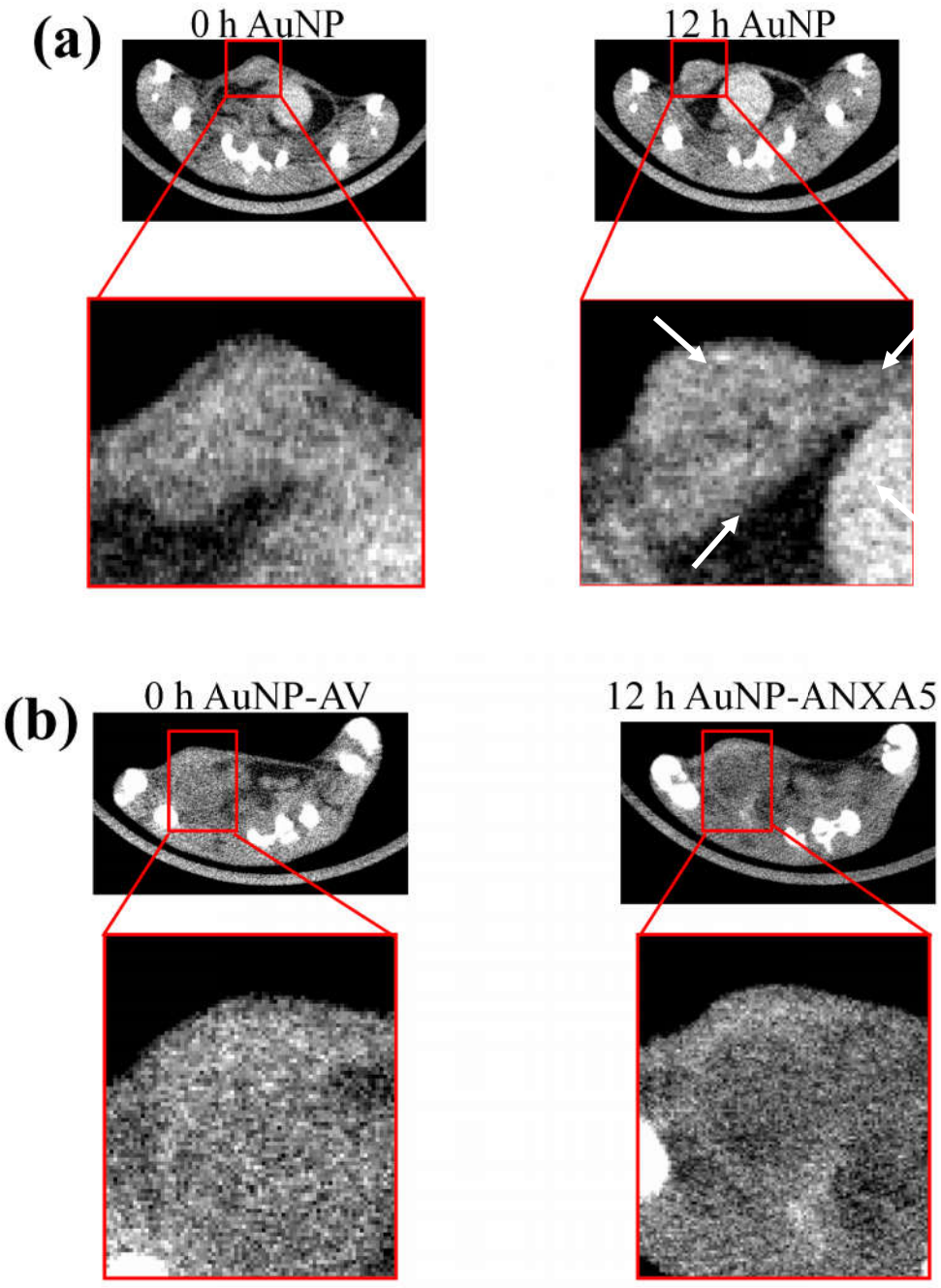

Figure 21. Representative CT images (xz cross section) of Balb/c mice with 4T1 breast cancer tumors.
Mice were imaged before and 12 h after injection of either 250 mg kg^{-1} (a) AuNPs or (b) AuNP-ANXA5s. (a) In the mouse injected with AuNPs it is difficult to identify the tumor compared to the remainder of the animal. (b) In the mouse injected with AuNP-

ANXA5s, a clear border of the tumor is significantly brighter (white arrows) where the gold nanoparticles have accumulated.

The images in figure 21 were taken for multiple mice (n = 6-7) injected with either AuNP or AuNP-ANXA5 and analyzed for accumulation of gold nanoparticles at the tumor as percent injected dose. Percent injected dose was calculated as seen in equation 2.

$$Injected\ Dose\ (\%) = \frac{Concentration\ of\ AuNP\ at\ tumor(mg\ ml^{-1})\ x\ Volume\ of\ tumor\ (ml)}{Amount\ of\ injected\ AuNP\ (mg)}\ x\ 100$$

Equation 2. Injected dose calculation.
Concentration of AuNP or AuNP-ANXA5 at the tumor was calculated with a pre-determined standard curve comparing change in contrast to concentration of gold nanoparticles.

As seen the Figure 22, tumors of mice with AuNP-ANXA5 had significantly higher accumulation of nanoparticles compared to untargeted nanoparticles starting as early as 4 hours and continuing for 96 hours. There is ~2-3-fold increase in concentration of gold nanoparticles when comparing targeted versus untargeted nanoparticles. The contrast remained for up to 96 h which can be further advantageous clinically as a means of monitoring tumor progression during rounds of chemotherapy to evaluate the real-time efficacy of the treatment.

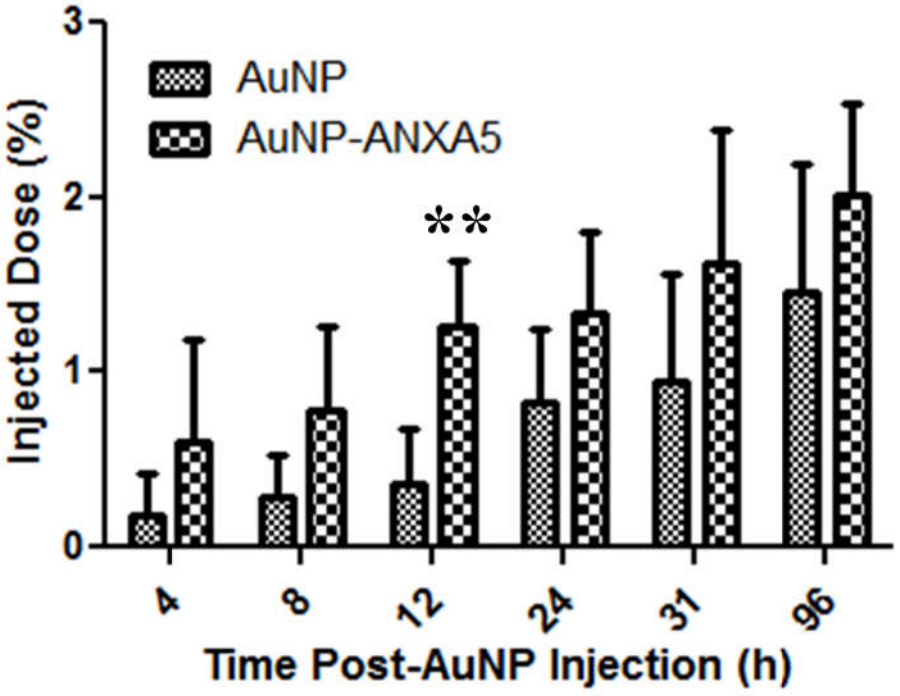

Figure 22. Binding specificity of targeted versus untargeted AuNPs *in vivo*. Mice with orthotopic breast cancer (4T1) tumors were injected with either AuNPs or AuNP-ANXA5s and imaged over a 96 hour period to evaluate accumulation at the site of the tumor. A dose of 250 mg kg^{-1} was given per animal, which is significantly lower than the LD50 (5000 mg kg^{-1}). No signs of mouse stress or toxicity were detected during the course of the study. Mice injected with AuNP-ANXA5s had significant accumulation of nanoparticles as compared to AuNPs injected mice as early as 4 hours after. The sharp difference in accumulation remains throughout the remainder of the study with increasing amounts of the injected dose accumulating at the tumor and remaining there until at least 96 hours post injection. Data represented as mean ± SEM ($n = 6 – 7$). Statistical significance indicated as ** ($p < 0.01$).

Discussion

Breast cancer has a 94% survival rate if diagnosed early on; however when diagnosed during late stage, survival falls to only 10% [14, 122]. Mammograms are the current gold standard for breast cancer diagnosis with up to a 65% misdiagnosis rate, usually due to the failure of differentiating tumors from dense breasts [14, 122]. A novel targeted gold nanoparticle has been developed with computed tomography as an alternative to diagnosis of breast cancer earlier and with more specificity. Gold nanoparticles are conjugated to annexin V, which binds specifically to phosphatidylserine exposed on tumor cells and tumor vasculature. CT, a widely available imaging modality, can be used to detect presence of breast cancer with higher sensitivity and specificity than the current standard of care.

Targeted gold nanoparticles were developed and characterized using DLS, zeta-potential, UV-vis spectroscopy, and TEM. Changes in the hydrodynamic diameter and zeta potential confirmed addition of PEG and ANXA5 to the surface of gold nanoparticles. PEG acts a protective polymer shielding the gold nanoparticles from the immune system by minimizing recognition as seen in the more neutral zeta-potential of the gold nanoparticles. ANXA5 is a negatively charged protein which causes a negative shift in the PEG coated gold nanoparticles as well as an increase in the hydrodynamic diameter.

In vitro studies showed specific binding of AuNP-ANXA5 to 4T1 breast cancer cells via fluorescent microscopy and microCT imaging. The addition of AuNPs caused a 2-fold increase in contrast, while the addition of AuNP-ANXA5 increased contrast by 4-fold compared to breast cancer cells only. *In vivo* studies confirmed plasma clearance

of AuNP-ANXA5s within 8 h post-injection and tumor identification as soon as 4 h after injection. AuNP-ANXA5s had a 2-3-fold increase in contrast compared to control AuNPs, which lasted for 96 h post-injection. Tumors as small as 4 mm were identifiable, making AuNP-ANXA5 a promising modality for early diagnosis of breast cancer compared to the 10 – 20 mm detection limit of mammograms [27]. The AuNPs have an LD50 of 100 mg (5000 mg kg^{-1}) per animal as evaluated by the company (Nanoprobes Inc.). Doses as high as 1100 mg kg^{-1} have been tested in mice with no detectable toxicity [28]. Our dose of 5 mg per animal (250 mg kg^{-1}) is significantly lower than the cytotoxic dose.

Recent studies using targeted gold nanoparticles showed similar increases in contrast *in vitro* and *in vivo* against larynx and oral cancer, glioblastoma, and lymph nodes as compared to untargeted nanoparticles [28, 133-136]. Compared to other targeted nanoparticles, a key advantage of the proposed technology is the broad applicability for detection of multiple cancers, such as bladder, ovarian, melanoma, and lung, which do not have effective diagnosis modalities that are sensitive as well as widely available to the general public. Current diagnosis tools require expensive and scarcely available tools such as MRI or PET systems with the risk of still getting false positives and negatives. Due to a lack of a cost-effective and widely available imaging modality, most patients are diagnosed during late stages of tumor development at which point the effectiveness of surgery and chemotherapy has significantly decreased. The proposed technology can be further expanded as an alternative for the universal detection of multiple cancers using computed tomography (CT), which is already widely present in all clinics and hospitals.

Conclusions

The use of AuNP-ANXA5, a novel, targeted contrast agent for early detection of breast cancer, in conjunction with computed tomography can provide an alternative cost-effective diagnosis tool with more precision and accuracy for multiple malignancies including breast cancer. We have developed and evaluated the efficacy of AuNP-ANXA5s in cell culture as well as in animal models showing significant increases in detection of breast tumors with targeted versus untargeted gold nanoparticles. Gold nanoparticles have minimum toxicity and are currently being tested in phase I clinical trials for therapy based applications [128, 129]. Combined with ANXA5, which is a naturally occurring human protein, the targeted nanoparticle contrast agent has the capability of being a universal diagnosis tool for early cancer detection of multiple malignancies (breast, ovarian, melanoma, bladder, etc).

Chapter VII: Conclusions and Future Directions

A large group of patients with cancer are either diagnosed once metastasis has occurred or have relapsed with chemoresistive tumors. In order to treat as well as diagnose these patients, novel biotechnology agents needs to be developed. This thesis proposes the use of annexin V (ANXA5) conjugated agents for the novel treatment and diagnosis of bladder, ovarian, and breast cancer. ANXA5 is a mammalian protein that specifically interacts with phosphatidylserine (PS), which is expressed by the tumor vasculature and multiple cancer cells [7, 37]. The interaction between ANXA5 and PS can be used to target therapeutic biotechnology agents, such as single-walled carbon nanotubes (SWCNT-AVNXA5) and enzyme prodrug systems (mCTH-ANXA5 and mCGL-ANXA5), for local treatment of tumors while minimizing nonspecific accumulation and toxicity of these agents, which is a key limiting factor for most chemotherapeutic drugs. Although current chemotherapeutics are effective in treating low stage tumors at high doses, the damage to healthy tissue due to nonspecific accumulation often outweighs the therapeutic efficacy thus limiting their use. ANXA5 can also be used to target imaging agents such as gold nanoparticles (AuNP-ANXA5) to tumors for enhanced early detection of breast cancer as well as other PS expressing tumors. This thesis focused on the development and assessment of three PS-targeted biotechnology agents for tumor treatment and/or detection with promising results for clinical translatability.

Single-walled carbon nanotubes

Single-walled carbon nanotubes (SWCNTs) can generate heat by two key mechanisms: 1) absorbing light in the near-infrared (NIR) region, specifically 980 nm, and dissipating their energy as heat and 2) generating dipole moments in a radiofrequency (RF) field and generating vibrational energy that leads to heat dissipation. Chapters II and III focus on the efficacy of PS targeted SWCNT-ANXA5s as photothermal ablation agents for cancer therapy.

SWCNT-ANXA5s at very low doses (0.1 mg SWCNTs kg^{-1}) are delivered intravesically into the bladder of mice with orthotopic murine bladder cancer (MB49) and treated for a short period (30 sec) with a global NIR light (power density of 1.7 W cm^{-2}). After one cycle of therapy, there was a 50% survival rate with no recurrence of bladder cancer for 116 days at which point the study was ended. No nonspecific accumulation of SWCNT-AVs was detected in any clearance organs or the bladders of treated mice, and no short-term or long-term toxicity was identified.

Due to the relative safety of the photothermal approach, future work can be conducted on a multi-cycle therapy to increase the survival rate and decrease recurrence rate of bladder cancer. The photothermal approach can be further enhanced with inhibitors of heat shock proteins (HSP), which are activated as a defense mechanism in healthy and cancer cells to promote survival and resistance [137]. A previous study showed strong synergism between a heat-based therapy and HSP inhibitors with significant increase in overall survival [138]. The photothermal therapy can also be combined with chemotherapy drugs for improved survival since nanotubes can be effective drug delivery vehicles [139-141]. The addition of chemotherapeutic drugs

such as docetaxel and doxorubicin provides a means of a multi-pronged treatment, a higher payload of drug delivery, and a more targeted chemotherapeutic drug delivery system that may reduce nonspecific side effects associated with free, untargeted drugs.

Although SWCNT-ANXA5s in conjunction with NIR is effective at treating non-muscle invasive bladder cancer, this therapy can be further expanded into deeper tumors that are less accessible using radiofrequency (RF). RF can also cause SWCNT-ANXA5 heating, which can be further enhanced if the appropriate resonance frequency is applied. Chapter III of this thesis focuses on preliminary studies to determine the appropriate resonance frequency of SWCNT-ANXA5s since RF can deeply penetrate tissue to treat cancers, such as bone, brain, and liver tumors. Future work to determine the resonance frequency can be determined; however even at 45 MHz the rate of heating of SWCNT-ANXA5s is significantly higher than NIR heating, which already causes tumor cell death as seen in Chapter 2. Evaluation of *in vitro* and *in vivo* cytotoxicity can be conducted for a more clinically, noninvasive therapy for PS expressing tumors.

Enzyme prodrug system

A novel mammalian fusion protein (mCTH-ANXA5) was developed previously with specific binding to PS expressing tumor cells and vasculature via ANXA5, as well as methionase activity for the conversion of a nontoxic prodrug, selenomethionine (SeMet), into a toxic, reactive oxygen species (ROS) generating drug, methylselenol [25]. Most patients with ovarian cancer are diagnosed once metastasis has occurred with a portion quickly developing platinum-resistive tumors. In order to provide an alternative, an enzyme prodrug system (mCTH-ANXA5) was developed for treatment and combined with immunostimulation for a synergistic approach in Chapter IV. The enzyme prodrug system delivered every day for 21 days provided a decrease in overall tumor burden two weeks post-therapy. This decrease was further enhanced with the addition of anti-CD73, which blocks CD73 receptors on cancer cells and prevents production of adenosine, and anti-OX40, which is a T-cell activating co-stimulatory antibody. The addition of both immunostimulants increased median survival from 45 days for saline treated mice to 57 days as well as decreased final tumor burden. The synergism of the enzyme prodrug system and immunostimulation is seen in the increases in cell- and antibody-mediated immune responses. There is an overall increase in the ratio of effector immune cells compared to regulatory immune cells in the mesenteric lymph nodes as well as a significant increase in tumor specific antibodies.

The enzyme prodrug system can be further improved by testing other combination of immunostimulants such as anti-PD-1 or anti-CTLA-4, both of which are currently in clinical trials. The dose and frequency of the immunotimulants alone and in combination with the enzyme prodrug system can also be optimized to reduce the

number of cycles of therapy, making it more clinically relevant. Since ROS induces cell death by causing DNA damage, alkylation agents such as cyclophosphamide or cisplatin can be tested that would prevent the cancer cells from repairing their damaged DNA and increase synergism. Pyridoxal-5'-phosphate (PLP), which is a cofactor of mCTH and has proven to increase the half-life of methionase from 1.5 to 7 h, and can be added to increase the efficacy of the therapy and decrease frequency of cycles needed. PLP dosage and frequency of delivery can also be optimized to prevent unbound and any nonspecifically accumulated mCTH-ANXA5 from causing healthy tissue damage. Currently, mCTH-ANXA5 is delivered intraperitoneally (i.p.), which can easily diffuse molecules under 20 kD [142]. mCTH-ANXA5 is 320 kD, which limits its diffusion across the peritoneum and into blood circulation for efficient targeting of PS expressing tumor vasculature. Future studies can compare delivery of mCTH-ANXA5 and effectiveness of therapy between i.p. and intravenous (i.v.) injections.

Another possibility to improve the overall survival and decrease tumor burden is to deliver a more active form of mCTH-ANXA5. Chapter V focuses on the development of a novel mutant of cystathionine gamma-lyase (mCGL-ANXA5) with eight new point mutations; the result was an increase in methionase activity by three-fold compared to mCTH-ANXA5. The improved fusion protein can be tested *in vivo* against the original mutant for changes in overall tumor burden as well as differences in dosages of the enzyme prodrug system needed to achieve similar efficacies. Due to the increase in mutations, mCGL-ANXA5 may be more immunogenic then mCTH-

ANXA5. Antibody titers and toxicity analysis can be conducted to determine the biocompatibility of the new mutant.

Gold nanoparticles

A key to effective cancer treatment is early cancer detection. The current gold standard for breast cancer diagnosis is a mammogram; however mammograms have a high false positive rate [14]. This rate can be decreased with the use of targeted contrast agents such as PS specific gold nanoparticles (AuNP-ANXA5). AuNP-ANXA5 increases contrast of tumors as small as 4 mm compared to untargeted gold nanoparticles using computed tomography (CT) as seen in Chapter VI.

A dose of 250 mg kg^{-1} AuNP-ANXA5 had a 2-3 fold increase in contrast as early as 4 h post-injection. Although the injected dose is 20 times lower than the LD_{50} of 5000 mg kg^{-1} as reported by the gold nanoparticle manufacturer (Nanoprobes), further optimization of dosage can be conducted to determine the lowest dose needed to achieve tumor contrast with minimal nonspecific accumulation and toxicity. A key problem with mammograms today is the difficulty in differentiating a dense breast or a breast with microcalcifications from a breast tumor. Since AuNP-ANXA5 specifically binds PS exposed on tumor cells and the tumor vasculature, targeted gold nanoparticles can be tested as novel agents with increased specificity and sensitivity to differentiate a tumor from a microcalcification or dense breast.

Work in this thesis with the gold nanoparticles has focused on breast cancer; however as seen in the previous chapters and literature, tumors such as bladder, ovarian, liver, and renal cancer also express PS with no efficient means of mass screening [7, 37]. Future work can focus on developing the versatility of AuNP-ANXA5 as a universal contrast agent for routine screenings using a CT, which is already widely available in most clinics and hospitals. Similar to SWCNTs, gold nanoparticles have

also been used as drug delivery vehicles [143-145]. AuNP-ANXA5 can be further expanded to be a multi-modal nanoparticle for detection as well as therapy by delivering cytotoxic drugs directly to the tumor. However, since the optimal AuNP-ANXA5 dose for imaging is likely to be different from that for cytotoxic drug delivery, it may be necessary to use AuNP-ANXA5 for imaging and a AuNP-ANXA5 drug conjugate for drug delivery.

Phosphatidylserine targeting biotechnology agents

All three PS-targeting biotechnology agents were effective in preventing systemic toxicity due to their specificity to the tumor via ANXA5. Although this thesis has focused each agent on one cancer, PS is expressed in multiple tumors and the tumor vasculature providing a means of a universal targeting molecule for novel therapies and imaging modalities.

References

[1] Hanahan D and Weinberg RA 2011 Hallmarks of cancer: the next generation *cell* **144** 646-74

[2] Burkhart DL and Sage J 2008 Cellular mechanisms of tumour suppression by the retinoblastoma gene *Nature reviews. Cancer* **8** 671

[3] Ghebranious N and Donehower LA 1998 Mouse models in tumor suppression *Oncogene* **17**

[4] Heerboth S, Housman G, Leary M, Longacre M, Byler S, Lapinska K, Willbanks A and Sarkar S 2015 EMT and tumor metastasis *Clinical and translational medicine* **4** 6

[5] Nguyen DX, Bos PD and Massagué J 2009 Metastasis: from dissemination to organ-specific colonization *Nature reviews. Cancer* **9** 274

[6] Philippi C, Loretz B, Schaefer U and Lehr C 2010 Telomerase as an emerging target to fight cancer—Opportunities and challenges for nanomedicine *Journal of controlled release* **146** 228-40

[7] Ran S and Thorpe PE 2002 Phosphatidylserine is a marker of tumor vasculature and a potential target for cancer imaging and therapy *Int. J. Radiat. Oncol. Biol. Phys.* **54** 1479-84

[8] Kamat AM, Colombel M, Sundi D, Lamm D, Boehle A, Brausi M, Buckley R, Persad R, Palou J and Soloway M 2017 BCG-unresponsive non-muscle-invasive bladder cancer: recommendations from the IBCG *Nat. Rev. Urology* **14** 244-55

[9] Di Stasi SM, Valenti M, Verri C, Liberati E, Giurioli A, Leprini G, Masedu F, Ricci AR, Micali F and Vespasiani G 2011 Electromotive instillation of mitomycin immediately before transurethral resection for patients with primary urothelial non-

muscle invasive bladder cancer: a randomised controlled trial *The lancet oncology* **12** 871-9

[10] Witjes JA, Hendricksen K, Gofrit O, Risi O and Nativ O 2009 Intravesical hyperthermia and mitomycin-C for carcinoma in situ of the urinary bladder: experience of the European Synergo® working party *World journal of urology* **27** 319-24

[11] Lokadasan R, James FV, Narayanan G and Prabhakaran PK 2016 Targeted agents in epithelial ovarian cancer: review on emerging therapies and future developments *ecancermedicalscience* **10**

[12] Cannistra SA, Matulonis UA, Penson RT, Hambleton J, Dupont J, Mackey H, Douglas J, Burger RA, Armstrong D and Wenham R 2007 Phase II study of bevacizumab in patients with platinum-resistant ovarian cancer or peritoneal serous cancer *Journal of Clinical Oncology* **25** 5180-6

[13] Du Bois A, Floquet A, Kim J-W, Rau J, Del Campo JM, Friedlander M, Pignata S, Fujiwara K, Vergote I and Colombo N 2014 Incorporation of pazopanib in maintenance therapy of ovarian cancer *Journal of clinical oncology* **32** 3374-82

[14] Heywang-Köbrunner SH, Hacker A and Sedlacek S 2011 Advantages and disadvantages of mammography screening *Breast care* **6** 199-207

[15] Yakobson BI and Avouris P. Mechanical properties of carbon nanotubes. Carbon nanotubes: Springer; 2001. p. 287-327.

[16] Baloch KH, Voskanian N, Bronsgeest M and Cumings J 2012 Remote Joule heating by a carbon nanotube *Nature Nanotechnology* **7** 316-9

[17] Pop E 2010 Energy dissipation and transport in nanoscale devices *Nano Res.* **3** 147-69

[18] Calderwood SK. Hyperthermia, the tumor microenvironment and immunity. Tumor Ablation: Springer; 2013. p. 29-37.

[19] Marconnet AM, Panzer MA and Goodson KE 2013 Thermal conduction phenomena in carbon nanotubes and related nanostructured materials *Reviews of Modern Physics* **85** 1295

[20] Kim SY and Park HS 2009 Multilayer friction and attachment effects on energy dissipation in graphene nanoresonators *Applied Physics Letters* **94** 101918

[21] Lu D, Li Y, Rotkin SV, Ravaioli U and Schulten K 2004 Finite-size effect and wall polarization in a carbon nanotube channel *Nano Letters* **4** 2383-7

[22] Padma VV 2015 An overview of targeted cancer therapy *Bio. Med.* **5** 19-

[23] Xu G and McLeod HL 2001 Strategies for enzyme/prodrug cancer therapy *Clin. Cancer Res.* **7** 3314-24

[24] Zhang J, Kale V and Chen M 2015 Gene-directed enzyme prodrug therapy *AAPS. J.* **17** 102-10

[25] Krais JJ, Virani N, McKernan PH, Nguyen Q, Fung K-M, Sikavitsas VI, Kurkjian CD and Harrison RG 2017 Antitumor Synergism and Enhanced Survival with a Tumor Vasculature-Targeted Enzyme Prodrug System, Rapamycin, and Cyclophosphamide *Mol. Cancer Ther.* MCT-16-0263

[26] Guillen KP, Ruben EA, Virani N and Harrison RG 2017 Annexin-directed β-glucuronidase for the targeted treatment of solid tumors *Protein Eng. Des. Sel.* **30** 85-94

[27] Welch HG, Prorok PC, O'Malley AJ and Kramer BS 2016 Breast-cancer tumor size, overdiagnosis, and mammography screening effectiveness *New England Journal of Medicine* **375** 1438-47

[28] Hainfeld JF, O'Connor MJ, Dilmanian F, Slatkin DN, Adams DJ and Smilowitz HM 2011 Micro-CT enables microlocalisation and quantification of Her2-targeted gold nanoparticles within tumour regions *The British journal of radiology* **84** 526-33

[29] Bertrand N, Wu J, Xu X, Kamaly N and Farokhzad OC 2014 Cancer nanotechnology: the impact of passive and active targeting in the era of modern cancer biology *Adv. Drug Deliv. Rev.* **66** 2-25

[30] Shi J, Kantoff PW, Wooster R and Farokhzad OC 2016 Cancer nanomedicine: progress, challenges and opportunities *Nat. Rev. Cancer*

[31] Hillen F and Griffioen AW 2007 Tumour vascularization: sprouting angiogenesis and beyond *Cancer and Metastasis Reviews* **26** 489-502

[32] Bazak R, Houri M, El Achy S, Hussein W and Refaat T 2014 Passive targeting of nanoparticles to cancer: A comprehensive review of the literature *Molecular and clinical oncology* **2** 904-8

[33] Folkman J, editor Angiogenesis and apoptosis. Seminars in cancer biology; 2003: Elsevier.

[34] Morrissey C and Vessella RL 2007 The role of tumor microenvironment in prostate cancer bone metastasis *Journal of cellular biochemistry* **101** 873-86

[35] Zhang L, Zhou H, Belzile O, Thorpe P and Zhao D 2014 Phosphatidylserine-targeted bimodal liposomal nanoparticles for in vivo imaging of breast cancer in mice *Journal of Controlled Release* **183** 114-23

[36] Zhang X, Huo L, Jin H, Han Y, Wang J, Zhang Y, Lai X, Le Z, Zhang J and Hua Z 2017 Anti-cancer activity of Annexin V in murine melanoma model by suppressing tumor angiogenesis *Oncotarget* **8** 42602-12

[37] Ran S, He J, Huang X, Soares M, Scothorn D and Thorpe PE 2005 Antitumor effects of a monoclonal antibody that binds anionic phospholipids on the surface of tumor blood vessels in mice *Clin. Cancer Res.* **11** 1551-62

[38] Zwaal R, Comfurius P and Bevers E 2005 Surface exposure of phosphatidylserine in pathological cells *Cellular and molecular life sciences* **62** 971-88

[39] Utsugi T, Schroit AJ, Connor J, Bucana CD and Fidler IJ 1991 Elevated expression of phosphatidylserine in the outer membrane leaflet of human tumor cells and recognition by activated human blood monocytes *Cancer Res.* **51** 3062-6

[40] Birge R, Boeltz S, Kumar S, Carlson J, Wanderley J, Calianese D, Barcinski M, Brekken R, Huang X and Hutchins J 2016 Phosphatidylserine is a global immunosuppressive signal in efferocytosis, infectious disease, and cancer *Cell Death Differ.* **23** 962-78

[41] Hochreiter-Hufford A and Ravichandran KS 2013 Clearing the dead: apoptotic cell sensing, recognition, engulfment, and digestion *Cold Spring Harbor perspectives in biology* **5** a008748

[42] Fadok VA, Bratton DL, Frasch SC, Warner ML and Henson PM 1998 The role of phosphatidylserine in recognition of apoptotic cells by phagocytes *Cell Death Differ.* **5**

[43] Borisenko GG, Matsura T, Liu S-X, Tyurin VA, Jianfei J, Serinkan FB and Kagan VE 2003 Macrophage recognition of externalized phosphatidylserine and phagocytosis of apoptotic Jurkat cells—existence of a threshold *Archives of biochemistry and biophysics* **413** 41-52

[44] Segawa K, Suzuki J and Nagata S 2011 Constitutive exposure of phosphatidylserine on viable cells *Proc. Natl. Acad. Sci. U.S.A.* **108** 19246-51

[45] Riedl S, Rinner B, Asslaber M, Schaider H, Walzer S, Novak A, Lohner K and Zweytick D 2011 In search of a novel target—phosphatidylserine exposed by non-apoptotic tumor cells and metastases of malignancies with poor treatment efficacy *Biochimica et Biophysica Acta (BBA)-Biomembranes* **1808** 2638-45

[46] Williamson P and Schlegel RA 1994 Back and forth: the regulation and function of transbilayer phospholipid movement in eukaryotic cells *Molecular membrane biology* **11** 199-216

[47] Sebastian TT, Baldridge RD, Xu P and Graham TR 2012 Phospholipid flippases: building asymmetric membranes and transport vesicles *Biochimica et Biophysica Acta (BBA)-Molecular and Cell Biology of Lipids* **1821** 1068-77

[48] Vallabhapurapu SD, Blanco VM, Sulaiman MK, Vallabhapurapu SL, Chu Z, Franco RS and Qi X 2015 Variation in human cancer cell external phosphatidylserine is regulated by flippase activity and intracellular calcium *Oncotarget* **6** 34375

[49] Connor J, Pak CH, Zwaal R and Schroit A 1992 Bidirectional transbilayer movement of phospholipid analogs in human red blood cells. Evidence for an ATP-dependent and protein-mediated process *Journal of Biological Chemistry* **267** 19412-7

[50] Kagan VE, Gleiss B, Tyurina YY, Tyurin VA, Elenström-Magnusson C, Liu S-X, Serinkan FB, Arroyo A, Chandra J and Orrenius S 2002 A role for oxidative stress in apoptosis: oxidation and externalization of phosphatidylserine is required for macrophage clearance of cells undergoing Fas-mediated apoptosis *The Journal of Immunology* **169** 487-99

[51] Soares MM, King SW and Thorpe PE 2008 Targeting inside-out phosphatidylserine as a therapeutic strategy for viral diseases *Nature medicine* **14** 1357-62

[52] Schutters K and Reutelingsperger C 2010 Phosphatidylserine targeting for diagnosis and treatment of human diseases *Apoptosis* **15** 1072-82

[53] Huber R, Schneider M, Mayr I, Römisch J and Paques E-P 1990 The calcium binding sites in human annexin V by crystal structure analysis at 2.0 A resolution Implications for membrane binding and calcium channel activity *FEBS letters* **275** 15-21

[54] Oling F, Bergsma-Schutter W and Brisson A 2001 Trimers, dimers of trimers, and trimers of trimers are common building blocks of annexin a5 two-dimensional crystals *Journal of structural biology* **133** 55-63

[55] Bryan RT, Collins SI, Daykin MC, Zeegers MP, Cheng K, Wallace DMA and Sole GM 2010 Mechanisms of recurrence of Ta/T1 bladder cancer *Ann. R. Coll. Surg. Engl.* **92** 519-24

[56] Shen Z, Shen T, Wientjes MG, O'Donnell MA and Au JL-S 2008 Intravesical treatments of bladder cancer: review *Pharm. Res.* **25** 1500-10

[57] Cheung G, Sahai A, Billia M, Dasgupta P and Khan MS 2013 Recent advances in the diagnosis and treatment of bladder cancer *BMC Med.* **11** 13

[58] Kobayashi T, Owczarek TB, McKiernan JM and Abate-Shen C 2015 Modelling bladder cancer in mice: opportunities and challenges *Nat. Rev. Cancer* **15** 42-54

[59] Nikfarjam M, Muralidharan V and Christophi C 2005 Mechanisms of focal heat destruction of liver tumors *J. Surg. Res.* **127** 208-23

[60] Burke AR, Singh RN, Carroll DL, Wood JC, D'Agostino RB, Ajayan PM, Torti FM and Torti SV 2012 The resistance of breast cancer stem cells to conventional hyperthermia and their sensitivity to nanoparticle-mediated photothermal therapy *Biomaterials* **33** 2961-70

[61] Singh R and Torti SV 2013 Carbon nanotubes in hyperthermia therapy *Adv. Drug Deliv. Rev.* **65** 2045-60

[62] Chen CH, Wu Y-J and Chen J-J 2015 Photo-thermal therapy of bladder cancer with Anti-EGFR antibody conjugated gold nanoparticles *Front. Biosci. (Landmark Ed.)* **21** 1211-21

[63] Moon HK, Lee SH and Choi HC 2009 In vivo near-infrared mediated tumor destruction by photothermal effect of carbon nanotubes *ACS Nano* **3** 3707-13

[64] Neves LF, Krais JJ, Van Rite BD, Ramesh R, Resasco DE and Harrison RG 2013 Targeting single-walled carbon nanotubes for the treatment of breast cancer using photothermal therapy *Nanotechnology* **24** 375104

[65] Bhirde AA, Sousa AA, Patel V, Azari AA, Gutkind JS, Leapman RD and Rusling JF 2009 Imaging the distribution of individual platinum-based anticancer drug molecules attached to single-wall carbon nanotubes *Nanomed.* **4** 763-72

[66] Robinson JT, Welsher K, Tabakman SM, Sherlock SP, Wang H, Luong R and Dai H 2010 High performance in vivo near-IR (> 1 μm) imaging and photothermal cancer therapy with carbon nanotubes *Nano Res.* **3** 779-93

[67] Tan A, Madani SY, Rajadas J, Pastorin G and Seifalian AM 2012 Synergistic photothermal ablative effects of functionalizing carbon nanotubes with a POSS-PCU nanocomposite polymer *J. Nanobiotechnology* **10** 34

[68] Kam NWS, O'Connell M, Wisdom JA and Dai H 2005 Carbon nanotubes as multifunctional biological transporters and near-infrared agents for selective cancer cell destruction *Proc. Natl. Acad. Sci. U.S.A.* **102** 11600-5

[69] Huang X, Bennett M and Thorpe PE 2005 A monoclonal antibody that binds anionic phospholipids on tumor blood vessels enhances the antitumor effect of docetaxel on human breast tumors in mice *Cancer Res.* **65** 4408-16

[70] Iancu C and Mocan L 2011 Advances in cancer therapy through the use of carbon nanotube-mediated targeted hyperthermia *Int J Nanomedicine* **6** 1675-84

[71] Marentette JO, Hauser PJ, Hurst RE, Klumpp DJ, Rickard A and McHowat J 2013 Tryptase activation of immortalized human urothelial cell mitogen-activated protein kinase *PloS One* **8** e69948

[72] Chan ES, Patel AR, Smith AK, Klein JB, Thomas AA, Heston WD and Larchian WA 2009 Optimizing orthotopic bladder tumor implantation in a syngeneic mouse model *J. Urol.* **182** 2926-31

[73] Tsyboulski DA, Liopo AV, Su R, Ermilov SA, Bachilo SM, Weisman RB and Oraevsky AA 2014 Enabling in vivo measurements of nanoparticle concentrations with three-dimensional optoacoustic tomography *J. Biophotonics* **7** 581-8

[74] Liu Z, Davis C, Cai W, He L, Chen X and Dai H 2008 Circulation and long-term fate of functionalized, biocompatible single-walled carbon nanotubes in mice probed by Raman spectroscopy *Proc. Natl. Acad. Sci. U.S.A.* **105** 1410-5

[75] Krais JJ, De Crescenzo O and Harrison RG 2013 Purine Nucleoside Phosphorylase targeted by Annexin V to breast cancer vasculature for enzyme prodrug therapy *PloS One* **8** e76403

[76] Raoof M, Cisneros BT, Corr SJ, Palalon F, Curley SA and Koshkina NV 2013 Tumor selective hyperthermia induced by short-wave capacitively-coupled RF electric-fields *PloS One* **8** e68506

[77] Li D, Jung YS, Kim HK, Chen J, Geller DA, Shuba MV, Maksimenko SA, Patch S, Forati E and Hanson GW 2012 The effect of sample holder geometry on electromagnetic heating of nanoparticle and NaCl solutions at 13.56 MHz *IEEE Transactions on Biomedical Engineering* **59** 3468-74

[78] Röschmann P 1987 Radiofrequency penetration and absorption in the human body: Limitations to high-field whole-body nuclear magnetic resonance imaging *Medical physics* **14** 922-31

[79] Glazer ES, Zhu C, Massey KL, Thompson CS, Kaluarachchi WD, Hamir AN and Curley SA 2010 Noninvasive radiofrequency field destruction of pancreatic adenocarcinoma xenografts treated with targeted gold nanoparticles *Clin. Cancer Res.* **16** 5712-21

[80] Koshkina NV, Briggs K, Palalon F and Curley SA 2014 Autophagy and enhanced chemosensitivity in experimental pancreatic cancers induced by noninvasive radiofrequency field treatment *Cancer* **120** 480-91

[81] Huttel AK, Steele GA, Witkamp B, Poot M, Kouwenhoven LP and van der Zant HS 2009 Carbon nanotubes as ultrahigh quality factor mechanical resonators *Nano letters* **9** 2547-52

[82] Chien WT, Chen CS and Chen HH 2006 Resonant frequency analysis of fixed-free single-walled carbon nanotube-based mass sensor *Sensors and Actuators A: Physical* **126** 117-21

[83] Garcia-Sanchez D, San Paulo A, Esplandiu M, Perez-Murano F, Forró L, Aguasca A and Bachtold A 2007 Mechanical detection of carbon nanotube resonator vibrations *Physical review letters* **99** 085501

[84] Jensen K, Weldon J, Garcia H and Zettl A 2007 Nanotube radio *Nano letters* **7** 3508-11

[85] Gibson RF, Ayorinde EO and Wen Y-F 2007 Vibrations of carbon nanotubes and their composites: a review *Composites Science and Technology* **67** 1-28

[86] Biercuk MJ, Ilani S, Marcus CM and McEuen PL. Electrical transport in single-wall carbon nanotubes. Carbon Nanotubes: Springer; 2007. p. 455-93.

[87] Balandin AA 2011 Thermal properties of graphene, carbon nanotubes and nanostructured carbon materials *arXiv preprint arXiv:1106.3789*

[88] Musatov A, Izrael'yants K and Blagov E 2014 Field electron emission from carbon nanotubes in the presence of a weak high-frequency electric field *JETP letters* **99** 224-8

[89] Shuba MV, Slepyan GY, Maksimenko SA and Hanson GW 2010 Radiofrequency field absorption by carbon nanotubes embedded in a conductive host *Journal of Applied Physics* **108** 114302

[90] Curley SA, Palalon F, Sanders KE and Koshkina NV 2014 The effects of non-invasive radiofrequency treatment and hyperthermia on malignant and nonmalignant cells *International journal of environmental research and public health* **11** 9142-53

[91] Raoof M and Curley SA 2011 Non-invasive radiofrequency-induced targeted hyperthermia for the treatment of hepatocellular carcinoma *International journal of hepatology* **2011**

[92] Cardinal J, Klune JR, Chory E, Jeyabalan G, Kanzius JS, Nalesnik M and Geller DA 2008 Noninvasive radiofrequency ablation of cancer targeted by gold nanoparticles *Surgery* **144** 125-32

[93] Gannon CJ, Patra CR, Bhattacharya R, Mukherjee P and Curley SA 2008 Intracellular gold nanoparticles enhance non-invasive radiofrequency thermal destruction of human gastrointestinal cancer cells *J. Nanobiotechnology* **6** 2

[94] Rejinold NS, Jayakumar R and Kim Y-C 2015 Radio frequency responsive nano-biomaterials for cancer therapy *Journal of Controlled Release* **204** 85-97

[95] Gannon CJ, Cherukuri P, Yakobson BI, Cognet L, Kanzius JS, Kittrell C, Weisman RB, Pasquali M, Schmidt HK and Smalley RE 2007 Carbon nanotube-enhanced thermal destruction of cancer cells in a noninvasive radiofrequency field *Cancer* **110** 2654-65

[96] Pop E, Mann D, Cao J, Wang Q, Goodson K and Dai H 2005 Negative differential conductance and hot phonons in suspended nanotube molecular wires *Physical Review Letters* **95** 155505

[97] Pop E, Mann D, Wang Q, Goodson K and Dai H 2006 Thermal conductance of an individual single-wall carbon nanotube above room temperature *Nano letters* **6** 96-100

[98] Lengyel E 2010 Ovarian cancer development and metastasis *Am. J. Pathol.* **177** 1053-64

[99] Stone E, Paley O, Hu J, Ekerdt B, Cheung N-K and Georgiou G 2012 De novo engineering of a human cystathionine-γ-lyase for systemic l-Methionine depletion cancer therapy *ACS chemical biology* **7** 1822-9

[100] Sato D and Nozaki T 2009 Methionine gamma-lyase: The unique reaction mechanism, physiological roles, and therapeutic applications against infectious diseases and cancers *IUBMB Life* **61** 1019-28

[101] Liou G-Y and Storz P 2010 Reactive oxygen species in cancer *Free radical research* **44** 479-96

[102] Poisson LM, Munkarah A, Madi H, Datta I, Hensley-Alford S, Tebbe C, Buekers T, Giri S and Rattan R 2015 A metabolomic approach to identifying platinum resistance in ovarian cancer *J. Ovarian Res.* **8** 13

[103] Cavuoto P and Fenech MF 2012 A review of methionine dependency and the role of methionine restriction in cancer growth control and life-span extension *Cancer Treat. Rev.* **38** 726-36

[104] Gaillard SL, Secord AA and Monk B 2016 The role of immune checkpoint inhibition in the treatment of ovarian cancer *Gynecologic oncology research and practice* **3** 11

[105] Homicsko K and Coukos G 2015 Targeting Programmed Cell Death 1 in Ovarian Cancer *Journal of Clinical Oncology* **33** 3987-9

[106] Iwai Y, Hamanishi J, Chamoto K and Honjo T 2017 Cancer immunotherapies targeting the PD-1 signaling pathway *Journal of Biomedical Science* **24** 26

[107] Guo Z, Wang X, Cheng D, Xia Z, Luan M and Zhang S 2014 PD-1 blockade and OX40 triggering synergistically protects against tumor growth in a murine model of ovarian cancer *PloS One* **9** e89350

[108] Allard B, Pommey S, Smyth MJ and Stagg J 2013 Targeting CD73 enhances the antitumor activity of anti-PD-1 and anti-CTLA-4 mAbs *Clin. Cancer Res.* **19** 5626-35

[109] Antonioli L, Yegutkin GG, Pacher P, Blandizzi C and Haskó G 2016 Anti-CD73 in cancer immunotherapy: awakening new opportunities *Trends in cancer* **2** 95-109

[110] Gaudreau P-O, Allard B, Turcotte M and Stagg J 2016 CD73-adenosine reduces immune responses and survival in ovarian cancer patients *Oncoimmunology* **5** e1127496

[111] Turcotte M, Spring K, Pommey S, Chouinard G, Cousineau I, George J, Chen GM, Gendoo DM, Haibe-Kains B and Karn T 2015 CD73 is associated with poor prognosis in high-grade serous ovarian cancer *Cancer Res.* **75** 4494-503

[112] Linch SN, McNamara MJ and Redmond WL 2015 OX40 agonists and combination immunotherapy: putting the pedal to the metal *Frontiers in oncology* **5**

[113] Aspeslagh S, Postel-Vinay S, Rusakiewicz S, Soria J-C, Zitvogel L and Marabelle A 2016 Rationale for anti-OX40 cancer immunotherapy *European Journal of Cancer* **52** 50-66

[114] Yang Z, Wang J, Lu Q, Xu J, Kobayashi Y, Takakura T, Takimoto A, Yoshioka T, Lian C and Chen C 2004 PEGylation confers greatly extended half-life and attenuated immunogenicity to recombinant methioninase in primates *Cancer Res.* **64** 6673-8

[115] Sun X, Yang Z, Li S, Tan Y, Zhang N, Wang X, Yagi S, Yoshioka T, Takimoto A and Mitsushima K 2003 In vivo efficacy of recombinant methioninase is enhanced by the combination of polyethylene glycol conjugation and pyridoxal 5′-phosphate supplementation *Cancer Res.* **63** 8377-83

[116] Van Rite BD, Lazrak YA, Pagnon ML, Palwai NR, Neves LF, McFetridge PS and Harrison RG 2011 Enzyme prodrug therapy designed to target L-methioninase to the tumor vasculature *Cancer letters* **301** 177-84

[117] Hamanishi J 2015 Safety and Antitumor Activity of Anti-PD-1 Antibody, Nivolumab, in Patients With Platinum-Resistant Ovarian Cancer *J Clin Oncol* **33**

[118] Hay CM, Sult E, Huang Q, Mulgrew K, Fuhrmann SR, McGlinchey KA, Hammond SA, Rothstein R, Rios-Doria J and Poon E 2016 Targeting CD73 in the tumor microenvironment with MEDI9447 *Oncoimmunology* **5** e1208875

[119] Yang Z, Sun X, Li S, Tan Y, Wang X, Zhang N, Yagi S, Takakura T, Kobayashi Y and Takimoto A 2004 Circulating half-life of PEGylated recombinant methioninase holoenzyme is highly dose dependent on cofactor pyridoxal-5′-phosphate *Cancer Res.* **64** 5775-8

[120] Georgiou G, Stone E and Lu W-C. Engineered primate L-methioninase for therapeutic purposes. Google Patents; 2016.

[121] Gibson DG, Smith HO, Hutchison III CA, Venter JC and Merryman C 2010 Chemical synthesis of the mouse mitochondrial genome *Nature methods* **7** 901-3

[122] Andrews KS, Brawley OW and Wender RC 2017 Cancer screening in the United States, 2017: A review of current American Cancer Society guidelines and current issues in cancer screening *Ca: a Cancer Journal for Clinicians* **67** 100

[123] Nelson HD, Pappas M, Cantor A, Griffin J, Daeges M and Humphrey L 2016 Harms of breast cancer screening: systematic review to update the 2009 US preventive services task force recommendationharms of breast cancer screening *Annals of internal medicine* **164** 256-67

[124] Connor EE, Mwamuka J, Gole A, Murphy CJ and Wyatt MD 2005 Gold nanoparticles are taken up by human cells but do not cause acute cytotoxicity *Small* **1** 325-7

[125] Kim J-K, Seo S-J, Kim K-H, Kim T-J, Chung M-H, Kim K-R and Yang T-K 2010 Therapeutic application of metallic nanoparticles combined with particle-induced x-ray emission effect *Nanotechnology* **21** 425102

[126] Cho SH, Jones BL and Krishnan S 2009 The dosimetric feasibility of gold nanoparticle-aided radiation therapy (GNRT) via brachytherapy using low-energy gamma-/x-ray sources *Physics in medicine and biology* **54** 4889

[127] Shukla R, Bansal V, Chaudhary M, Basu A, Bhonde RR and Sastry M 2005 Biocompatibility of gold nanoparticles and their endocytotic fate inside the cellular compartment: a microscopic overview *Langmuir* **21** 10644-54

[128] Libutti SK, Paciotti GF, Byrnes AA, Alexander HR, Gannon WE, Walker M, Seidel GD, Yuldasheva N and Tamarkin L 2010 Phase I and pharmacokinetic studies of CYT-6091, a novel PEGylated colloidal gold-rhTNF nanomedicine *Clin. Cancer Res.* clincanres. 0978.2010

[129] Anselmo AC and Mitragotri S 2016 Nanoparticles in the clinic *Bioengineering & Translational Medicine* **1** 10-29

[130] Zolnik BS, Gonzalez-Fernandez A, Sadrieh N and Dobrovolskaia MA 2010 Minireview: nanoparticles and the immune system *Endocrinology* **151** 458-65

[131] Takae S, Akiyama Y, Otsuka H, Nakamura T, Nagasaki Y and Kataoka K 2005 Ligand density effect on biorecognition by PEGylated gold nanoparticles: regulated interaction of RCA120 lectin with lactose installed to the distal end of tethered PEG strands on gold surface *Biomacromolecules* **6** 818-24

[132] Ba H, Rodríguez-Fernández J, Stefani FD and Feldmann J 2010 Immobilization of gold nanoparticles on living cell membranes upon controlled lipid binding *Nano letters* **10** 3006-12

[133] Popovtzer R, Agrawal A, Kotov NA, Popovtzer A, Balter J, Carey TE and Kopelman R 2008 Targeted gold nanoparticles enable molecular CT imaging of cancer *Nano letters* **8** 4593-6

[134] Lai S-F, Ko B-H, Chien C-C, Chang C-J, Yang S-M, Chen H-H, Petibois C, Hueng D-Y, Ka S-M and Chen A 2015 Gold nanoparticles as multimodality imaging agents for brain gliomas *J. Nanobiotechnology* **13** 85

[135] Reuveni T, Motiei M, Romman Z, Popovtzer A and Popovtzer R 2011 Targeted gold nanoparticles enable molecular CT imaging of cancer: an in vivo study *Int. J. Nanomedicine* **6** 2859

[136] Eck W, Nicholson AI, Zentgraf H, Semmler W and Bartling Sn 2010 Anti-CD4-targeted gold nanoparticles induce specific contrast enhancement of peripheral lymph nodes in X-ray computed tomography of live mice *Nano letters* **10** 2318-22

[137] Calderwood SK, Stevenson MA and Murshid A 2012 Heat shock proteins, autoimmunity, and cancer treatment *Autoimmune diseases* **2012**

[138] Ito A, Matsuoka F, Honda H and Kobayashi T 2003 Heat shock protein 70 gene therapy combined with hyperthermia using magnetic nanoparticles *Cancer Gene Therapy* **10** 918

[139] Liu Z, Tabakman S, Welsher K and Dai H 2009 Carbon nanotubes in biology and medicine: in vitro and in vivo detection, imaging and drug delivery *Nano Res.* **2** 85-120

[140] Liu Z, Chen K, Davis C, Sherlock S, Cao Q, Chen X and Dai H 2008 Drug delivery with carbon nanotubes for in vivo cancer treatment *Cancer Res.* **68** 6652-60

[141] Bianco A, Kostarelos K and Prato M 2005 Applications of carbon nanotubes in drug delivery *Current opinion in chemical biology* **9** 674-9

[142] Lu Z, Wang J, Wientjes MG and Au JL 2010 Intraperitoneal therapy for peritoneal cancer *Future oncology* **6** 1625-41

[143] Ghosh P, Han G, De M, Kim CK and Rotello VM 2008 Gold nanoparticles in delivery applications *Adv. Drug Deliv. Rev.* **60** 1307-15

[144] Paciotti GF, Myer L, Weinreich D, Goia D, Pavel N, McLaughlin RE and Tamarkin L 2004 Colloidal gold: a novel nanoparticle vector for tumor directed drug delivery *Drug delivery* **11** 169-83

[145] Brown SD, Nativo P, Smith J-A, Stirling D, Edwards PR, Venugopal B, Flint DJ, Plumb JA, Graham D and Wheate NJ 2010 Gold nanoparticles for the improved anticancer drug delivery of the active component of oxaliplatin *Journal of the American Chemical Society* **132** 4678-84

Appendix A: Supplemental Data

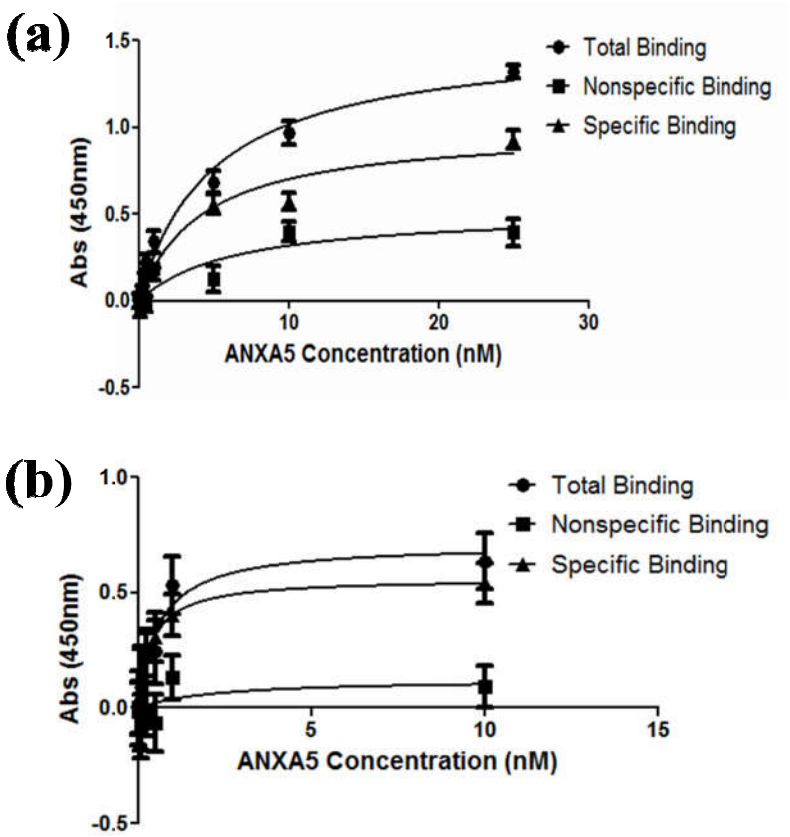

Figure 23. Binding strength data of ANXA5 for bladder cancer cells.
Specific binding was determined by subtracting total binding in Ca^{2+} supplemented media from nonspecific binding in EDTA supplemented medium for (a) MB49 and (b) J82 cells. Binding was quantified with biotinylated ANXA5 and HRP-conjugated streptavidin, developed with OPD. Data are presented as mean ± SEM (n = 3).

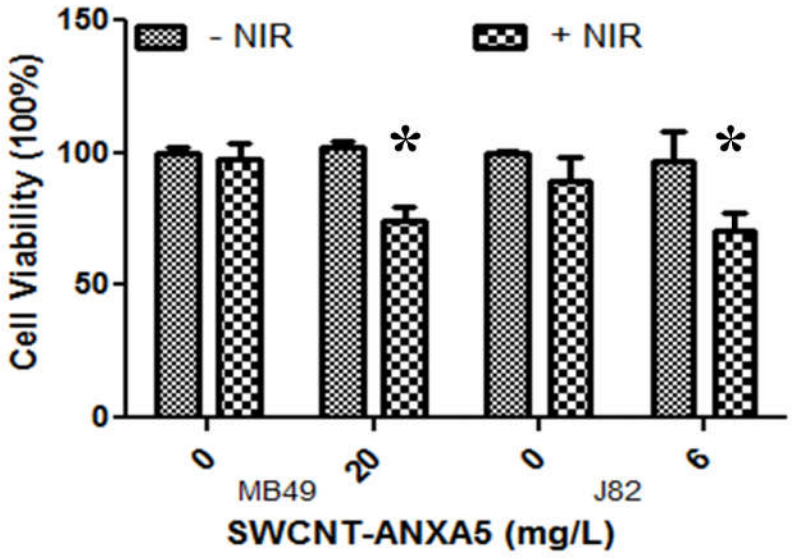

Figure 24. In vitro cytotoxicity of SWCNT-ANXA5s with NIR.
Murine (MB49) or human (J82) bladder cancer cells were incubated with 20 mg l^{-1} of SWCNT-ANXA5 for 2 h at 37°C. Cells were washed three times with media followed by 30 sec of NIR treatment at 50 J cm^{-2} or 100 J cm^{-2} for MB49 or J82 cells, respectively. Data presented at mean ± SEM (n = 3). Statistical significance indicated as * ($p < 0.05$).

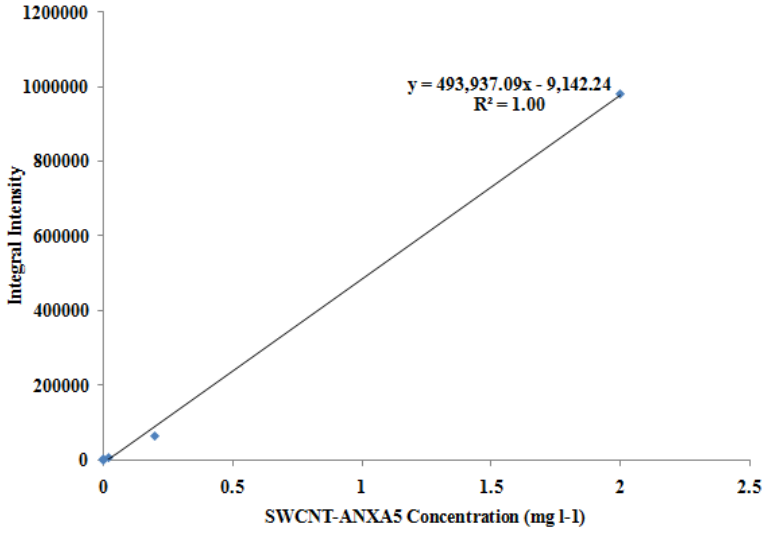

Figure 25. Standard curve for SWCNT-ANXA5 versus NIR fluorescence.
The NIR fluorescence intensities for various concentrations of SWCNT-ANXA5 were determined by integrating the area under the curve from 800 to 1400 nm.

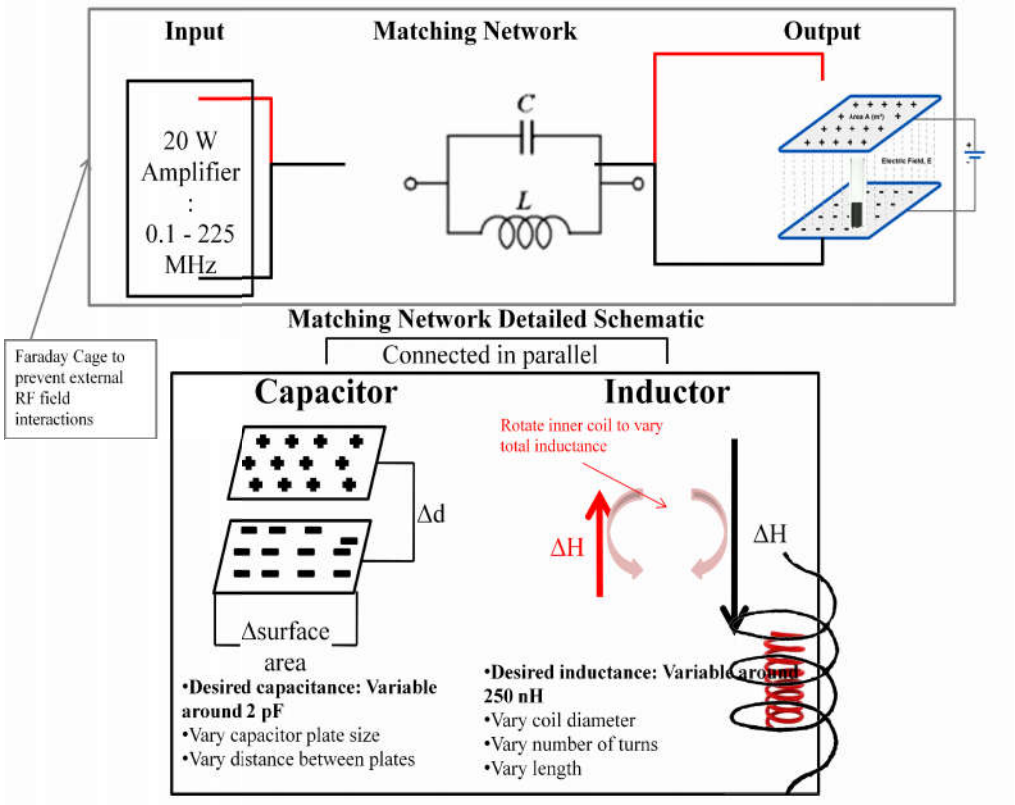

Figure 26. Schematic of RF system and matching network.
In order to determine the resonance of nanotubes within the RF range as well as run *in vitro* cytotoxicity studies, a RF and matching networks needs to be built. A schematic of the proposed system is presented here.

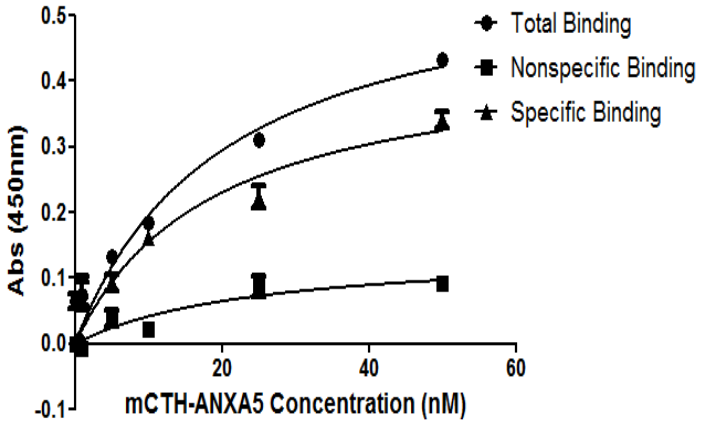

Figure 27. Binding strength data of mCTH-ANXA5 for ovarian cancer cells.
Specific binding was determined by subtracting total binding in Ca^{2+} supplemented media from nonspecific binding in EDTA supplemented medium for ID8 $p53^{-/-}$ cells.

Binding was quantified with biotinylated mCTH-ANXA5 and HRP-conjugated streptavidin, developed with OPD. Data are presented as mean ± SEM (n = 3).

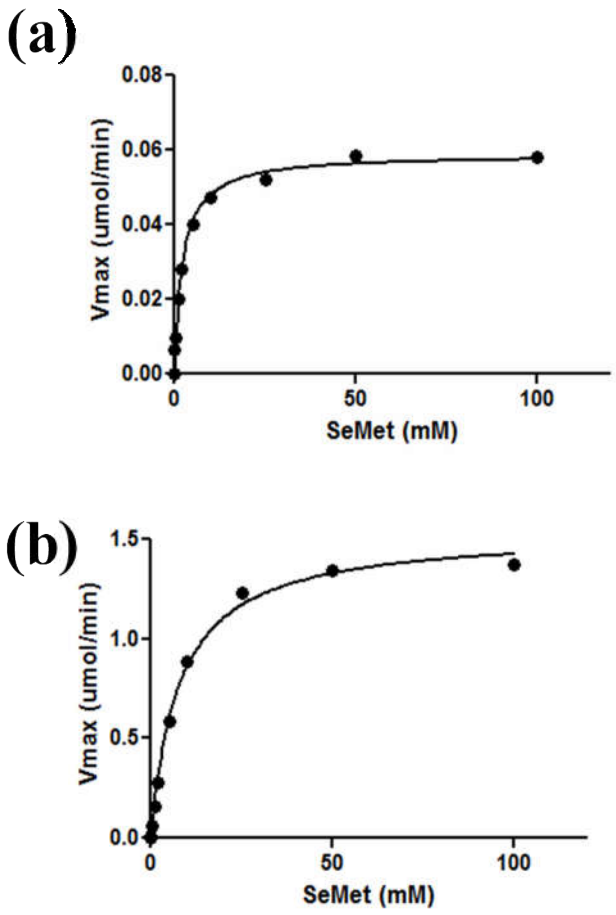

Figure 28. Michaelis-Menten kinetics.
The Michaelis-Menten kinetics of (a) mCGL-ANXA5 and (b) mCTH-ANXA5 with selenomethionine as the substrate. The Michaelis constant, K_M, was determined as half the maximum rate (V_{max}).

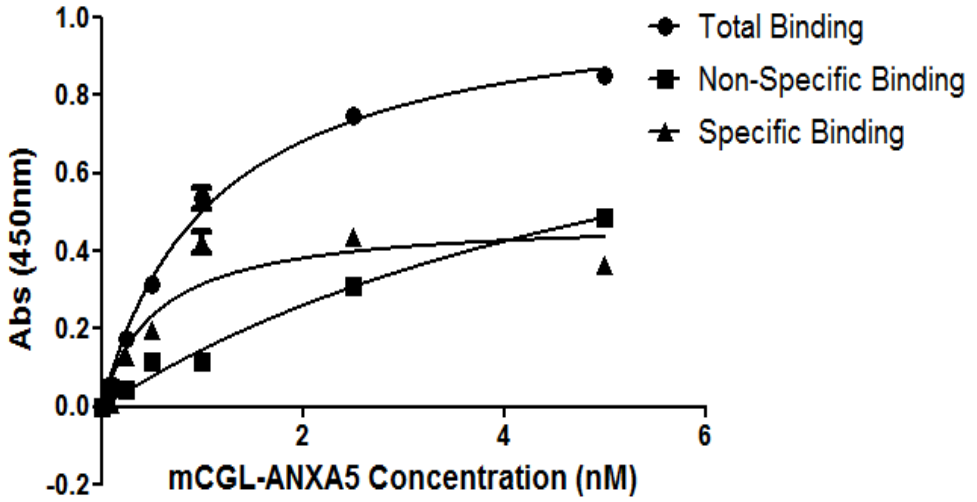

Figure 29. Binding strength data of mCGL-ANXA5 for breast cancer cells.
Specific binding was determined by subtracting total binding in Ca^{2+} supplemented media from nonspecific binding in EDTA supplemented medium for 4T1 cells. Binding was quantified with biotinylated mCGL-ANXA5 and HRP-conjugated streptavidin, developed with OPD. Data are presented as mean ± SEM (n = 3).

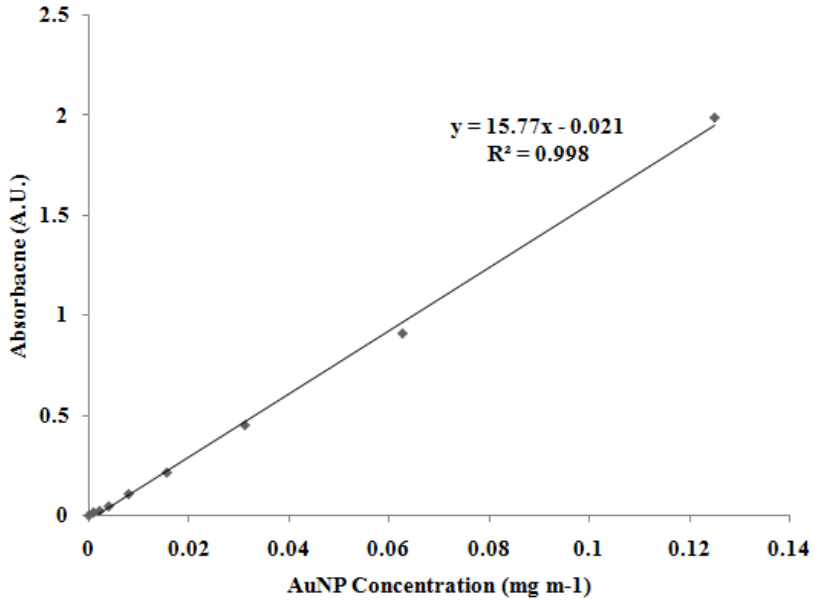

Figure 30. Standard curve for AuNP concentration.
Absorbance of AuNP was measured at 520 nm at various concentrations to determine the standard curve for AuNPA-ANXA5 concentration determination.

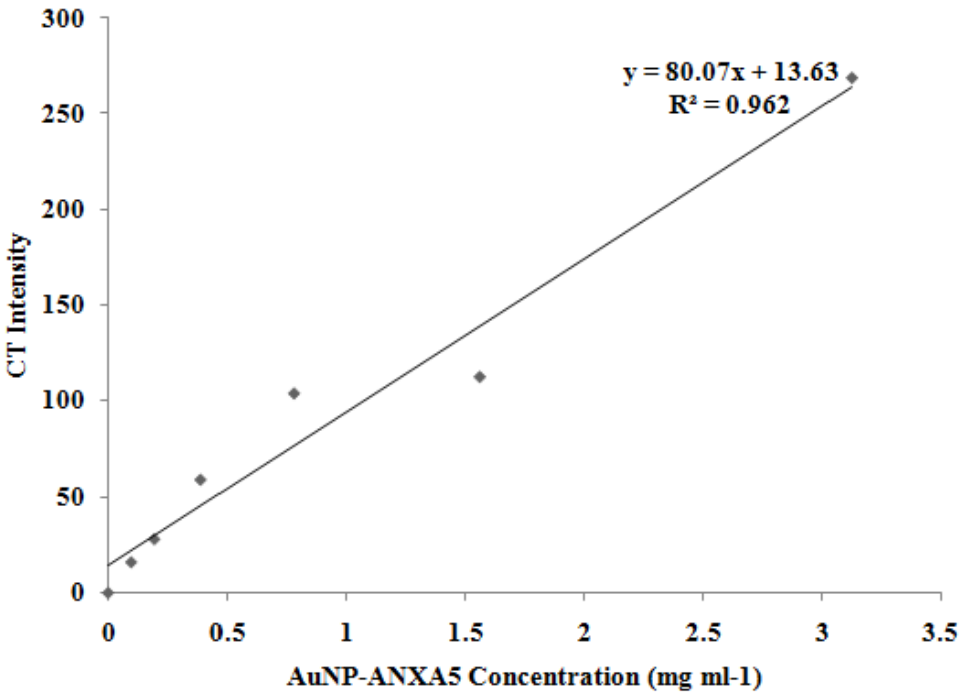

Figure 31. Standard curve for AuNP-ANXA5 concentration compared to CT intensity.
The CT intensities for various concentrations of AuNP-ANXA5 were determined at 50 keV.

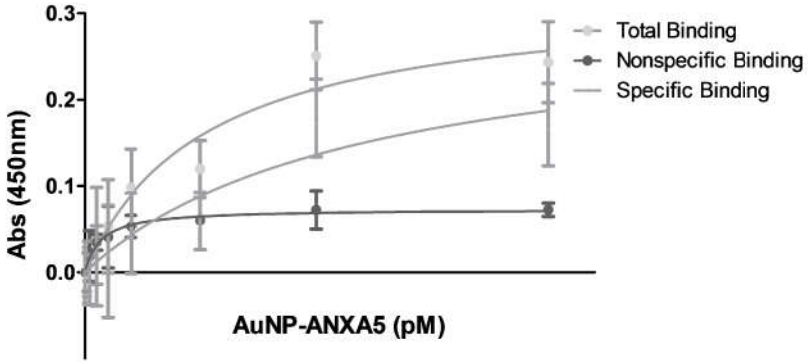

Figure 32. Binding strength data of AuNP-ANXA5 for breast cancer cells.
Specific binding was determined by subtracting total binding in Ca^{2+} supplemented media from nonspecific binding in EDTA supplemented medium for 4T1 cells. Binding was quantified with biotinylated AuNP-ANXA5 and HRP-conjugated streptavidin, developed with OPD. Data are presented as mean ± SEM (n = 3).

Appendix B: mCGL-ANXA5 Gene Construction

Legend: **mCGL**, *ANXA5*, His-tag, **His-tag cleavage site**, **Mutations**, ***Sequencing Primers***

mCGL-ANXA5 Pre-cleavage

MHHHHHHSSGLVPRGSGMKETAAAKFERQHMDSPDLGTDDDDKM**LEVLFQ|GP**
MQKDASLSGFLPSFQHFATQAIHVGQEPEQWNSRAVVLPISLATTFKQD
FPGQSSGFIYSRLGNPTRNCLEKAVAALDGAKHSLAFASGMAATITITHLLK
AGDEIICMDEVYGGTNAYFRRVASEFGLKISFVDCSKTKLLEAAITPQTKLV
WIETPTNPTLKLADIGACAQIVHKRGDIILVVDNTFMSAYFQRPLALGADIC
MCSATKYMNGHSDVVMGLVSVNSDDLNSRLRFLQNSLGAVPSPFDCYLCC
RGLKTLQVRMERHFKNGMAVARFLETNPRVEKVVYPGLPSHPQHELAKR
QCSGCGGMVSFYIKGALQHAKAFLKNLKLFTLAVSLGGYESLAELPASMT
HASVPEKDRATLGINDTLIRLSVGLEDEQDLLEDLDRALKAAHP*SGGGGSG*
GGG*MATRGTVTDFPGFDGRADAEVLRKAMKGLGTDEDSILNLLTSRSNAQRQEIAQ*
EFKTLFGRDLVDDLKSELTGKFEKLIVAMMKPSRLYDAYELKHALKGAGTDEKVLT
EIIASRTPEELSAIKQVYEEEYGSNLEDDVVGDTSGYYQRMLVVLLQANRDPDTAIDD
AQVELDAQALFQAGELKWGTDEEKFITIFGTRSVSHLRRVFDKYMTISGFQIEETIDR
ETSGNLEQLLLAVVKSIRSIPAYLAETLYYAMKGAGTDDHTLIRVVVSRSEIDLFNIRKE
FRKNFATSLYSMIKGDTSGDYKKALLLLCGGEDD

mCGL-ANXA5 Post-cleavage

GP**MQKDASLSGFLPSFQHFATQAIHVGQEPEQWNSRAVVLPISLATTFKQ**
DFPGQSSGFIYSRLGNPTRNCLEKAVAALDGAKHSLAFASGMAATITITHLL
KAGDEIICMDEVYGGTNAYFRRVASEFGLKISFVDCSKTKLLEAAITPQTKL
VWIETPTNPTLKLADIGACAQIVHKRGDIILVVDNTFMSAYFQRPLALGADI
CMCSATKYMNGHSDVVMGLVSVNSDDLNSRLRFLQNSLGAVPSPFDCYLC
CRGLKTLQVRMERHFKNGMAVARFLETNPRVEKVVYPGLPSHPQHELAK
RQCSGCGGMVSFYIKGALQHAKAFLKNLKLFTLAVSLGGYESLAELPASM
THASVPEKDRATLGINDTLIRLSVGLEDEQDLLEDLDRALKAAHP*SGGGGS*
GGGG*MATRGTVTDFPGFDGRADAEVLRKAMKGLGTDEDSILNLLTSRSNAQRQEIA*
QEFKTLFGRDLVDDLKSELTGKFEKLIVAMMKPSRLYDAYELKHALKGAGTDEKVL
TEIIASRTPEELSAIKQVYEEEYGSNLEDDVVGDTSGYYQRMLVVLLQANRDPDTAID
DAQVELDAQALFQAGELKWGTDEEKFITIFGTRSVSHLRRVFDKYMTISGFQIEETID
RETSGNLEQLLLAVVKSIRSIPAYLAETLYYAMKGAGTDDHTLIRVVVSRSEIDLFNIRK
EFRKNFATSLYSMIKGDTSGDYKKALLLLCGGEDD

mCGL-ANXA5 Complete Sequence

ATGCACCATCATCATCATCATTCTTCTGGTCTGGTGCCACGCGGTTCTGGTA
TGAAAGAAACCGCTGCTGCTAAATTCGAACGCCAGCACATGGACAGCCCAG
ATCTGGGTACCGATGACGACGACAAGATG**CTGGAAGTTCTGTTCCAGGGT**
CCGATGCAGAAAGACGCGAGCCTGTCTGGCTTCCTGCCGTCTTTTCAGCACT
TCGCAACTCAGGCGATCCACGTTGGTCAGGAGCCTGAACAATGGAACTCTC
GTGCGGTTGTTCTGCCGATCAGCCTCGCCACGACCTTCAAACAGGATTTCCC
GGGTCAGTCTTCTGGTTTCATCTACTCCCGTCTGGG***CAATCCGACCCGTAACT***
GCCTGGAAAAAGCGGTAGCCGCGCTGGACGGTGCGAAACACTCTCTGGCGT
TCGCCTCTGGTATGGCGGCGACCATCACGATCACCCATCTGCTCAAGGCCGG
TGACGAAATCATCTGTATGGACGAAGTTTACGGTGGCACCAACGCGTATTTT
CGTCGTGTTGCGTCTGAATTCGGTCTGAAAATCTCTTTCGTTGACTGCTCTAA
AACCAAACTCCTGGAGGCAGCAATTACTCCGCAGACGAAACTCGTTTGGAT
CGAAACCCCGACCAACCCGACCCTGAAGCTCGCCGACATCGGTGCGTGCGC
TCAAATCGTTCACAAACGTGGTGACATCATCCTGGTTGTTGATAATACCTTC
ATGTCTGCGTACTTTCAGCGTCCGCTGGCGCTGGGCGCTGACATCTGCATGT
GCTCCGCGACCAAATACATGAACGGTCACTCTGACGTAGTTATGGGTCTGGT
TAGCGTTAA***CAGCGACGATCTCAATTCCC***GCCTGCGTTTCCTGCAGAACTCC
CTCGGCGCAGTACCGTCCCCGTTCGACTGCTATCTCTGCTGCCGTGGTCTCA
AAACGCTGCAGGTTCGTATGGAACGTCATTTCAAGAACGGTATGGCGGTGG
CGCGCTTCCTCGAAACGAACCCGCGTGTTGAAAAAGTTGTTTACCCTGGCCT
CCCGTCCCACCCGCAGCACGAACTGGCGAAACGTCAGTGCTCTGGTTGCGG
TGGCATGGTTTCCTTCTACATCAAAGGTGCCCTCCAGCACGCGAAAGCCTTC
CTGAAAAACCTGAAACTGTTCACCCTCGCGGTTTCTCTGGGTGGTTACGAAT
CTCTCGCTGAACTGCCGGCGTCCATGACCCACGCTTCTGTACCTGAAAAAGA
CCGTGCGACCCTCGGTATCAACGATACCCTGATCCGTCTGTCTGTTGGTCTG
GAGGACGAACAGGACCTGCTGGAAGAC***CTGGATCGTGCTCTCAAAGC***GGCG
CACCCGAGCGGTGGTGGTGGTAGTGGTGGCGGTGGTATGGCGACCCGTGGT
ACCGTTACTGATTTCCCGGGTTTCGACGGTCGTGCGGACGCGGAAGTTCTGC
GTAAAGCGATGAAAGGCCTGGGTACGGATGAAGATTCTATCCTGAACCTGC
TGACGTCTCGTTCTAACGCGCAACGCCAGGAAATCGCGCAGGAGTTCAAAA
CGCTGTTTGGCCGCGACCTGGTGGACGACCTCAAGTCCGAGCTGACCGGTA
AATTCGAAAAACTGATTGTTGCCATGATGAAGCCGTCCCGTCTGTATGACGC
GTACGAGCTCAAGCATGCGCTGAAAGGTGCTGGCACCGACGAAAA***GGTTCT***
GACCGAGATCATCGCCTCTCGTACCCCGGAAGAACTGTCTGCGATTAAACAG
GTTTACGAGGAAGAATACGGTTCTAATCTGGAGGACGACGTGGTCGGCGAT
ACTTCTGGTTACTATCAGCGTATGCTCGTTGTCCTGCTCCAGGCCAATCGTG
ATCCGGACACTGCGATCGACGATGCGCAAGTTGAGCTGGACGCACAGGCGC
TCTTCCAGGCTGGTGAACTGAAATGGGGCACGGACGAGGAGAAGTTCATCA
CCATCTTCGGCACGCGTTCTGTTAGCCACCTGCGTCGTGTTTTCGACAAATA
CATGACCATCTCTGGCTTTCAGATCGAAGAAACCATTGACCGTGAGACCTCT
GGTAACCTGGAACAGCTGCTGCTGGCGGTTGTTAAATCTATCCGTTCTATTC
CGGCGTACCTGGCGGAAACCCTGTACTACGCCATGAAGGGTGCGGGCACTG
ACGATCACACCCTGATTCGTGTTGTTGTTTCTCGCTCCGAGATTGATCTCTTC
AATATCCGTAAGGAATTTCGTAAAAACTTTGCGACTTCCCTCTACTCTATGA

TCAAAGGCGACACTAGCGGCGACTACAAAAAAGCGCTGCTCCTGCTGTGCG
GTGGTGAAGACGACTGACCGGGCTTCTCCTCAACCATGGCGATATCGGATC
CGAATT

Gibson Assembly Fragments

Fragment 1

CATGGACAGCCCAGATCTGGGTACCGATGACGACGACAAGATG**CTGGAAG**
TTCTGTTCCAGGGTCCGATGCAGAAAGACGCGAGCCTGTCTGGCTTCCTG
CCGTCTTTTCAGCACTTCGCAACTCAGGCGATCCACGTTGGTCAGGAGCCTG
AACAATGGAACTCTCGTGCGGTTGTTCTGCCGATCAGCCTCGCCACGACCTT
CAAACAGGATTTCCCGGGTCAGTCTTCTGGTTTCATCTACTCCCGTCTGGGC
AATCCGACCCGTAACTGCCTGGAAAAAGCGGTAGCCGCGCTGGACGGTGCG
AAACACTCTCTGGCGTTCGCCTCTGGTATGGCGGCGACCATCACGATCACCC
ATCTGCTCAAGGCCGGTGACGAAATCATCTGTATGGACGAAGTTTACGGTG
GCACCAACGCGTATTTTCGTCGTGTTGCGTCTGAATTCGGTCTGAAAATCTC
TTTCGTTGACTGCTCTAAAACCAAACTCCTGGAGGCAGCAATTACTCCGCAG
ACGAAACTCGTTTGGATCGAAACCCCGACCAACCCGACCCTGAAGCTCGCC
GACATCGGTGCGTGCGCTCAAATCGTTCACAAACGTGGTGACATCATCCTG
GTTGTTGATAATACCTTCATGTCTGCGTACTTTCAGCGTCCGCTGGCGCTGG
GCGCTGACATCTGCATGTGCTCCGCGACCAAATACATGAACGGTCACTCTG
ACGTAGTTATGGGTCTGGTTAGCGTTAACAGCGACGATCTCAATTCCCGCCT
GCGTTTCCTGCAGAACTCCCTCGGCGCAGTACCGTCCCCGTTCGACTGCTAT
CTCTGCTGCCGTGGTCTCAAAACGCTGCAGGTTCGTATGGAACGTCATTTCA
AGAACGGTATGGCGGTGGCGCGCTTCCTCGAAACGAACCCGCGTGTTGAAA
AAGTTGTTTACCCTGGCCTCCCGTCCCACCCGCAGCACGAACTGGCGAAAC
GTCAGTGCTCTGGTTGCGGTGGC

Fragment 2

GCACGAACTGGCGAAACGTCAGTGCTCTGGTTGCGGTGGCATGGTTTCCTTC
TACATCAAAGGTGCCCTCCAGCACGCGAAAGCCTTCCTGAAAAACCTGAAA
CTGTTCACCCTCGCGGTTTCTCTGGGTGGTTACGAATCTCTCGCTGAACTGC
CGGCGTCCATGACCCACGCTTCTGTACCTGAAAAAGACCGTGCGACCCTCG
GTATCAACGATACCCTGATCCGTCTGTCTGTTGGTCTGGAGGACGAACAGG
ACCTGCTGGAAGACCTGGATCGTGCTCTCAAAGCGGCGCACCCGAGCGGTG
GTGGTGGTAGTGGTGGCGGTGGTATGGCGACCCGTGGTACCGTTACTGATTT
CCCGGGTTTCGACGGTCGTGCGGACGCGGAAGTTCTGCGTAAAGCGATGAA
AGGCCTGGGTACGGATGAAGATTCTATCCTGAACCTGCTGACGTCTCGTTCT
AACGCGCAACGCCAGGAAATCGCGCAGGAGTTCAAAACGCTGTTTGGCCGC
GACCTGGTGGACGACCTCAAGTCCGAGCTGACCGGTAAATTCGAAAAACTG
ATTGTTGCCATGATGAAGCCGTCCCGTCTGTATGACGCGTACGAGCTCAAGC
ATGCGCTGAAAGGTGCTGGCACCGACGAAAAGGTTCTGACCGAGATCATCG
CCTCTCGTACCCCGGAAGAACTGTCTGCGATTAAACAGGTTTACGAGGAAG
AATACGGTTCTAATCTGGAGGACGACGTGGTCGGCGATACTTCTGGTTACTA
TCAGCGTATGCTCGTTGTCCTGCTCCAGGCCAATCGTGATCCGGACACTGCG
ATCGACGATGCGCAAGTTGAGCTGGACGCACAGGCGCTCTTCCAGGCTGGT
GAACTGAAATGGGGCACGGACGAGGAGAAGTTCATCACCATCTTCGGCACG
CGTTCTGTTAGCCACCTGCGTCGTGTTTTCGACAAATACATGACCATCTCTG
GCTTTCAGATCGAAGAAACCATT

Fragment 3

ATACATGACCATCTCTGGCTTTCAGATCGAAGAAACCATTGACCGTGAGAC
CTCTGGTAACCTGGAACAGCTGCTGCTGGCGGTTGTTAAATCTATCCGTTCT
ATTCCGGCGTACCTGGCGGAAACCCTGTACTACGCCATGAAGGGTGCGGGC
ACTGACGATCACACCCTGATTCGTGTTGTTGTTTCTCGCTCCGAGATTGATCT
CTTCAATATCCGTAAGGAATTTCGTAAAAACTTTGCGACTTCCCTCTACTCT
ATGATCAAAGGCGACACTAGCGGCGACTACAAAAAAGCGCTGCTCCTGCTG
TGCGGTGGTGAAGACGACTGACCGGGCTTCTCCTCAACCATGGCGATATCG
GATCCGAATT

Appendix C: Laboratory Protocols

FIJI macro for bladder tumor quantification

```
//This macro quantifies the TdTomato fluorescence on a mouse bladder with respect to bladder area
//The macro assumes the files are ".tif" images of a bladder from a dissection scope imaged for Tdtomato

//Close all current images
close("*");

//Clear results table
run("Clear Results");

//Choose the input directory for Tdtomato Fluorescent images
TRDirectory = getDirectory("Choose Fluoresence input directory");

//Get all filenames in directory and store in an array
TRfileList = getFileList(TRDirectory);

//Choose the output directory for the processed images and final analysis excel file
outputDirectory = getDirectory("Choose output directory");

//Set which measurements to collect: area, integrated density, and mean gray value
run("Set Measurements...", "area mean integrated redirect=None decimal=3");

//Overall image processing to all images one at a time
for (a=0; a<TRfileList.length; a++) {
	//Open fluorescent image and get title
	open(TRDirectory + TRfileList[a]);
	TRfile = getTitle();

	//Remove measurement units since there is no scale associated with these images
	//Program sets a default scale in inches which is incorrect for these images
	run("Properties...", "channels=1 slices=1 frames=1 unit=pixel pixel_width=1 pixel_height=1 voxel_depth=1 global");
	//Convert to an 8-bit from an RGB image to run further analysis
	run("8-bit");
	//Save converted image
	TRfile_Scaled = replace(TRfile, ".tif", "_Scaled.tif");
	saveAs("tiff", outputDirectory + TRfile_Scaled);

	//Remove dark current noise in image from camera and save image
	run("FeatureJ Derivatives", "x-order=0 y-order=0 z-order=0 smoothing=4");
```

```
	TRfile_Scaled_NoNoise = replace(TRfile, ".tif", "_Scaled_NoNoise.tif");
	saveAs("tiff", outputDirectory + TRfile_Scaled_NoNoise);

	//Threshold image using Huang algorithm to get mask of bladder and save
thresholded image
	run("Threshold...");
	setAutoThreshold("Huang dark");
	//Some images do not auto thershold properly so this allows user to adjust
thershold
	waitForUser("Adjust threshold value. \nClick OK when complete.");
	//By not selecting "BlackBackground", the object is assumed to be black and
background white
	setOption("BlackBackground", false);
	//Generates a binary mask of the thresholded image
	run("Convert to Mask");
	TRfile_Scaled_NoNoise_Threshold = replace(TRfile, ".tif",
"_Scaled_NoNoise_Threshold.tif");
	saveAs("tiff", outputDirectory + TRfile_Scaled_NoNoise_Threshold);

	//Closed 8-bit image
	close("*_Scaled.tif");

	//Get mask of only bladder and save mask
	//Only the bladder area will be measured since it is the only object that fits in the
	//size range selected (largest object)
	run("Analyze Particles...", "size=100000.00-Infinity show=Masks");
	TRfile_Scaled_NoNoise_Threshold_Mask = replace(TRfile, ".tif",
"_Scaled_NoNoise_Threshold_Mask.tif");
	saveAs("tiff", outputDirectory + TRfile_Scaled_NoNoise_Threshold_Mask);

	//Close Threshold image
	close("*_Scaled_NoNoise_Threshold.tif");

	//Create selection of mask and paste on original fluorescent image
	run("Create Selection");
	//Reopen original fluorescent image
	open(TRDirectory + TRfileList[a]);
	//Paste mask on original fluorescent image for quantification
	run("Restore Selection");

	//Measure area, mean, and integrated intensity
	run("Measure");

	//Add name to row to keep track of what results go with what image
	setResult("Sample", a, TRfile);
	updateResults();
```

```
	//Close all the current images
	close("*");
}

//Save measurements in results window to excel file in output directory
selectWindow("Results");
saveAs("Results", outputDirectory + "FinalAnalysis.xls");
selectWindow("Results");
run("Close");
selectWindow("Threshold");
run("Close");
```

Flow Cytometry Staining

Tissue Collection:

1. Euthanize animal with CO_2 inhalation.
2. Collect blood and place in heparin tube. Spin tube to separate plasma from blood and store at -20°C.
3. Collect lymph node and spleen and place in 5 ml of cold RPMI-1640 medium. Place samples on ice and transport to Norman.
4. Collect remaining tissue (liver, kidney, heart, lungs, intestine, and tumor) place in 10% NBF.

Flow Cytomery Buffer Preparation:

1. Flow Cytometry Staining Buffer (SB): 1X PBS + 0.5% BSA + 0.05% Sodium Azide.
2. Foxp3 Fixation/Permeabilization working solution: Dilute the Fixation/Permeabilization Concentrate (1 part) with Fixation/Permeabilization Diluent (3 parts). You will need 1 mL of the Fixation/Permeabilization working solution for each sample, if staining in tubes.
3. Permeabilization Buffer: Dilute the 10X concentrate with distilled water prior to use.

All following procedures with cells should be conducted on ice.

Flow Cytometry Sample Preparation:

1. Tease apart tissue (lymph node and spleen) into a single-cell suspension by pressing with the plunger of a 3-mL syringe with 1 ml of SB into a petri dish. Wash plunger 2X with 1 ml SB each time.

2. Place a cell strainer on top of a 50-ml conical tube. Pass cells from the petri culture dish through the cell strainer to eliminate clumps and debris. Wash petri dish and stainer 2X with 1 ml SB each time.
3. Centrifuge cell suspension at 300-400*g* for 4-5 min at 2-8°C. Discard the supernatant.
4. Resuspend the cell pellet in a 1 ml volume of SB and perform a cell count and viability analysis.
    a. Add 10 µl of typan blue + 10 µl of diluted cell suspension (1:100 dilution) and count live and total cells.
5. Centrifuge cells as in Step 3 and resuspend in appropriate volume of SB so that the final cell concentration is 1 x 10^7 cells ml^{-1}.

Flow Cytometry Staining

1. Add 100 µL of cell stock to a 2 mL microvial.
2. Spin primary antibody tubes to pull solution to bottom of vial.
3. Stock antibody cocktail
4. Add stock antibody cocktail (Table 1) and bring final volume to 50 µl with SB.
5. Incubate for at least 60 minutes at 2-8°C or on ice. Protect from light.
6. Wash the cells by adding Flow Cytometry Staining Buffer. Use 2 ml $tube^{-1}$. Centrifuge at 400-600*g* for 5 min at room temperature. Discard supernatant.
7. Repeat previous wash step.
8. Add 1 ml of Fixation/Permeabilization working solution to each tube and pulse vortex.

9. Incubate for 60 min at room temperature. Protect samples from light.
10. Wash the cells by adding 1X Permeabilization Buffer to each tube. Use 1 ml tube^{-1}. Centrifuge at 400-600*g* for 5 min at room temperature. Discard supernatant.
11. Repeat previous wash step.
12. Resuspend pellet in 100 µl of 1X Permeabilization Buffer. This is typically the residual volume after decanting.
13. Block with 2% BSA by adding 2 µl directly to the cells.
14. Incubate for 15 min at room temperature.
15. Without washing, add either 2.5 µL of PE-Foxp3 antibody or SB (Table 1) to cells.
16. Incubate for at least 30 minutes at room temperature. Protect samples from light.
17. Wash the cells by adding 1X Permeabilization Buffer to each tube. Use 1 ml tube^{-1}. Centrifuge at 400-600*g* for 5 min at room temperature. Discard supernatant.
18. Repeat previous wash step.
19. Resuspend cells in an appropriate volume of Flow Cytometry Staining Buffer.
20. Analyze samples by flow cytometry.

Antibody Titers

1) Mice were euthanized 3 days after immunostimulation and blood was collected in heparin tubes.
    a. Allow 20 min for clots to form before centrifugation
    b. Centrifuge at 3500*g* for 90 s.
    c. Remove serum with pipet and freeze (cryovial) at -80°C.
2) Plate ID8 $p53^{-/-}$ cells at 70% confluence on 96-well plates.
3) Buffers:
    a. Diluting Buffer (1 L)
        i. 0.5 g Tween 20 (0.005%)
        ii. 2.5 g BSA (0.25%)
        iii. 1 l PBS
    b. Wash Buffer
        i. 5 g Tween 20 (0.05%)
        ii. 1 l PBS
4) Add 50 µ of each serum sample to wells. Make appropriate dilutions.
5) Cover the plate with adhesive cover and incubate for 2 h at 37°C
6) Shake out the plates into a sink. Wash the plates with wash buffer 4 times by adding 200 µ and shaking out the wash buffer into a sink. Pat plates dry by inverting on paper towel.
7) Add 50 µl of anti-rabbit IgG-HRP conjugate (secondary antibody) diluted to 1:5000 (initially at about 1 mg/mL) using diluting buffer to each well.
8) Cover the plate with adhesive cover and incubate for 60 min at 37°C.

9) Shake out the plates into a sink. Wash the plates with wash buffer 4 times by adding 200 µl and shaking out the Wash buffer into a sink. Pat plates dry by inverting on paper towel.
10) Prepare a curve in blood/serum of different dilutions of anti-rabbit IgG-HRP conjugate.
11) Add 50 µl of OPD solution to each well.
    a. Add one capsule of phosphate-citrate buffer to 100 ml DI in beaker and stir (no more than 30 min prior to use of OPD).
    b. Weigh 0.4 mg ml^{-1} OPD and place in foil coated tube (6.4 mg for 16 ml buffer).
    c. Add 40 µl of 30% H_2O_2 (glass fridge) to buffer.
    d. Mix for 30 sec.
    e. Add required amount of buffer to OPD (16 ml) (use within 5 min).
    f. Mix by inversion
12) Cover the plate with adhesive cover and incubate for 30 min at room temperature in the dark.
13) Read absorbance at 450 nm.

mCGL-ANXA5 Transformation

1. Combine reagents for Gibson assembly.
    a. Use 50 ng of plasmid and 0.2 pmol of each fragment (equimolar). Run control.
        i. 1 ul pET-30 Ek/LIC (at 50 ng/µl)
        ii. 3.3 µl F1
        iii. 3.3 µl F2
        iv. 1.7 µl F3
    b. 10 µl Gibson Master Mix (2X)
    c. Nuclease free DI (adjust to final volume of 20 µl)
2. Incubate at 50°C for 1 h, then keep on ice (or -20°C) until transformation.
3. Transform NEB 5-alpha competent cells (included in Gibson Assembly kit) with Gibson Assembly reaction product.
    a. Thaw NEB 5-alpha competent cells on ice for 2-5 min.
    b. Resuspend cells and then add 2 ul of Gibson Assembly reaction to 50 µL cells in transformation tube on ice.
    c. Incubate the tube on ice for 30 minutes.
    d. Heat the tube for 30 sec in 42°C water bath.
    e. Incubate tube for 2 min on ice.
    f. Add 950 µl room temperature SOC medium to tube on ice.
    g. Incubate for 60 minutes at 37°C while shaking at 250 rpm.
    h. Concurrently, heat LB agar + 35 ug l^{-1} kanamycin or 25 ug l^{-1} ampicillin plates to 37°C for ~20 min prior to plating.

i. Spread 100 µL cell solution on plates using flame/EtOH sterilized glass pipette at several dilutions (1:1 to 1:100) in SOC medium. Use kanamycin plates to select for plasmid and ampicillin plates as a control.

j. Allow plates to sit on benchtop for several minutes, invert, and incubate overnight at 37°C.

4. Using a flame sterilized, blunt glass pipet, select several colonies and culture each colony in 15 mL of LB medium with antibiotic at 37°C and 250 rpm for 16 h.
5. Collect cells through centrifugation at 1000 x g and discard supernatant.
6. Perform a miniprep using the QIAprep spin columns.
    a. Resuspend pelleted bacterial cells in 250 ul Buffer P1 and transfer to microcentrifuge tube (make sure RNase A has been added to Buffer P1).
    b. Add 250 ul Buffer P2 and mix thoroughly by inverting the tube 4-6 times.
    c. Add 350 ul Buffer N3 and mix immediately and thoroughly by inverting the tube 4-6 times.
    d. Centrifuge for 10 min at 13,000 rpm in microcentrifuge.
    e. Apply the supernatants from step 4 to the QIAprep spin column by decanting or pipetting.
    f. Centrifuge for 30-60 sec. Discard flow through.
    g. Wash QIAprep spin column by adding 0.5 mL Buffer PB and centrifuge for 30- 60 sec. Discard flow through.

h. Wash QIAprep spin column by adding 0.75 ml Buffer PE and centrifuging for 30-60 sec.

i. Discard the flow through and centrifuge for an additional 1 minute to remove residual wash buffer.

j. Place QIAprep column in a clean 1.5 ml microcentrifuge tube. To elute DNA, add 50ul Buffer EB to the center of each QIAprep spin column, let stand for 1 min, then centrifuge for 1 min.

7. Run DNA electrophoresis to select appropriate DNA plasmid to sequence.
8. Submit for sequencing.
    a. T7 promoter, T7 terminator, and mutant mCGL-AV sequencing primers were used.
    b. Plasmid DNA should be submitted at approximately 100 ng/µL and primers at 3-5 µM.
9. After confirming correct sequence, transform plasmid miniprep for mutant mCGL-AV into T7 Express lysY competent cells and culture for expression.
    a. Thaw a tube of T7 Express *lysY* Competent *E. coli* cells on ice until the last ice crystals disappear (~10 min).
    b. Mix gently and carefully pipette 50 µl of cells into a transformation tube on ice.
    c. Add 1 µl of plasmid DNA to the cell mixture. Carefully flick the tube 4-5 times to mix cells and DNA. **Do not vortex.**
    d. Place the mixture on ice for 30 min. Do not mix.
    e. Heat shock at exactly 42°C for exactly 10 sec. Do not mix.

f. Place on ice for 5 minutes. Do not mix.

g. Pipette 950 µl of room temperature SOC into the mixture.

h. Place at 37°C for 60 min. Shake vigorously at 250 rpm.

i. Warm selection plates to 37°C for ~20 min prior to plating.

j. Mix the cells thoroughly by flicking the tube and inverting, then perform multiple 10-fold serial dilutions in SOC.

k. Spread 100 µl of each dilution onto 35 ug l^{-1} kanamycin plates.

l. Allow plates to sit on benchtop for several minutes, invert, and incubate overnight at 37°C.

m. Using flame sterilized, blunt glass pipet, select several colonies, and culture each colony in 10 mL of TB medium with 35 mg l^{-1} kanamycin at 30°C with shaking at 220 rpm for 16 h.

n. Collect colonies and 50% glycerol stocks. Store at -80°C.

Synthesis of AuNP-ANXA5

Procedure:

1. AuroVistTM-15 nm initially at 200 mg ml^{-1} PBS:
    a. Dilute AuNPs to (20 mg ml-1, 0.1 M) in PBS
        i. Final volume 0.5 ml
        ii. 50 ul of 200 mg ml^{-1} solution in 0.45 ml of PBS
2. PEGylating AuNPs:
    a. Dilute 61.2 mg (0.36 M) HS-PEG-NH_2 spacer in 0.5 ml of PBS (4:1 weight ratio spacer:AuNPs).
    b. Sonicate spacer solution for 15 min in water bath sonicator.
    c. Add HS-PEG-NH_2 solution dropwise to AuNPs solution and place on rotator.
    d. Let solution stir overnight on rotator (speed 1.5) at 4°C.
3. Purifying AuNP-PEG-NH_2 solution:
    a. Wash excess linker away
        i. Pipette solution into ultracentrifuge tube. Wash tube with PBS and place wash buffer with nanoparticles. Fill remaining ultracentrifuge tube space with PBS.
        ii. Centrifuge tubes at 16,000g for 20 min.
        iii. Remove supernatant and redisperse in sulfo-SMCC PBS buffer with water bath/probe sonicator.
            1. Add 1 mg Sulfo-SMCC in 0.5 ml PBS
4. Adding Maleimide groups to NH_2 functionalized AuNPs

a. Add Sulfo-SMCC solution to AuNP-PEG-NH_2.

b. Let reaction stir for 30 min under on rotator at room temperature.

5. Purifying AuNP-SMCC solution:

    a. Wash excess crosslinker away:

        i. Pipette solution into ultracentrifuge tube. Wash tube with PBS and place wash buffer with nanoparticles. Fill remaining ultracentrifuge tube space with PBS.

        ii. Centrifuge tubes at 16,000g for 20 min.

        iii. Remove supernatant and redisperse in 0.5 ml PBS buffer with water bath/probe sonicator.

6. Adding ANXA5 to maleimide functionalized AuNPs:

    a. Add 2:1 weight concentration ratio of ANXA5 to Sulfo-SMCC

        i. Annexin is 36,000 mg $mmol^{-1}$

    b. Let reaction shake 18 h under moderate speed at 4°C.

        i. Vial should be stabilized in a Styrofoam box and parallel to ensure proper circulation.

7. Blocking leftover Maleimide groups on AuNP-ANXA5:

    a. Dissolve 1.5mg L-Cysteine in 1mL PBS.

        i. Vortex for a minute to dissolve

    b. Add 10ul L-Cysteine solution to AuNP-ANXA5

    c. Let shake 1 h under moderate speed at 4°C.

8. Purifying AuNP-ANXA5 solution:

    a. Wash excess Annexin away:

i. Pipette solution into ultracentrifuge tube. Wash tube with PBS and place wash buffer with nanoparticles. Fill remaining ultracentrifuge tube space with PBS.
ii. Centrifuge tubes at 12,000g for 15 min.
iii. Remove supernatant and redisperse in in desired volume of PBS buffer with water bath/probe sonicator.

9. Measure concentration of AuNP and ANXA5 in final product.

AuNP-ANXA5 Blood Pharmacokinetics

14) Perform retro orbital draws between 0 and 24 h in heparin tubes.
    a. Allow 20 min for clots to form before centrifugation
    b. Centrifuge at 3500*g* for 90 s.
    c. Remove serum with pipet and freeze (cryovial) at -80°C.
15) Prepare biotinylated AuNP-ANXA5 nanoparticle calibration curve in blood/serum (typically between 0 $\mu g\ ml^{-1}$ and 10 $\mu g\ ml^{-1}$) and assay solutions.
    a. Diluting Buffer (1 L)
        i. 0.5 g Tween 20 (0.005%)
        ii. 2.5 g BSA (0.25%)
        iii. 1 l PBS
    b. Wash Buffer
        i. 5 g Tween 20 (0.05%)
        ii. 1 l PBS
16) Add 50 µ of each serum sample to wells. Make appropriate dilutions. Use streptavidin-coated 96 well plates.
17) Cover the plate with adhesive cover and incubate for 60 min at 37°C
18) Shake out the plates into a sink. Wash the plates with wash buffer 4 times by adding 200 µ and shaking out the wash buffer into a sink. Pat plates dry by inverting on paper towel.
19) Add 50 µl of Annexin V polyclonal antibody (rabbit) diluted to 1.25 $\mu g\ ml^{-1}$ in diluting buffer to each well.
20) Cover the plate with adhesive cover and incubate for 60 min at 37°C.

21) Shake out the plates into a sink. Wash the plates with wash buffer 4 times by adding 200 µl and shaking out the wash buffer into a sink. Pat plates dry by inverting on paper towel.

22) Add 50 µl of anti-rabbit IgG-HRP conjugate (secondary antibody) diluted to 1:1,000 (initially at about 1 mg/mL) using diluting buffer to each well.

23) Cover the plate with adhesive cover and incubate for 60 min at 37°C.

24) Shake out the plates into a sink. Wash the plates with wash buffer 4 times by adding 200 µl and shaking out the Wash buffer into a sink. Pat plates dry by inverting on paper towel.

25) Add 50 µl of OPD solution to each well.

    a. Add one capsule of phosphate-citrate buffer to 100 ml DI in beaker and stir (no more than 30 min prior to use of OPD).
    b. Weigh 0.4 mg ml^{-1} OPD and place in foil coated tube (6.4 mg for 16 ml buffer).
    c. Add 40 µl of 30% H_2O_2 (glass fridge) to buffer.
    d. Mix for 30 sec.
    e. Add required amount of buffer to OPD (16 ml) (use within 5 min).
    f. Mix by inversion

26) Cover the plate with adhesive cover and incubate for 30 min at room temperature in the dark.

27) Read absorbance at 450 nm.